COATED FUEL PARTICLE INTEGRITY ANALYSIS

KAPLANMIŞ YAKIT PARÇACIKLARININ BÜTÜNLÜK ANALİZİ

OYA ÖZDERE GÜLOL

A dissertation submitted in partial satisfaction of the
requirements for the degree of
Doctor of Philosophy

in

Nuclear Engineering

According to the Regulations of
The Institute For Graduate Studies in
Pure and Applied Sciences
Hacettepe University

Spring 2007

To The Institute for Graduate Studies in Pure and Applied Sciences,

This study has been approved by the Graduate Committee as partial fulfillment of the requirements for the degree of **Doctor of Philosophy** in the field of **Nuclear Engineering**.

Graduate Committee

Head _____
Assoc. Prof. Dr. Mehmet Tombakoğlu

Member _____
Prof. Dr. Üner Çolak

Member _____
Assoc. Prof. Dr. Bora Yıldırım

Member _____
Assoc. Prof. Dr. C. Niyazi Sökmen

Member _____
Assist. Prof. Dr. Serkan Dağ

APPROVED
This dissertation has been approved on / /2007 by the Graduate Committee established by the Board of the Institute.

/ /2007

Prof. Dr. Erdem Yazgan
HEAD OF THE INSITUTE FOR GRADUATE
STUDIES IN PURE AND APPLIED SCIENCES

COATED FUEL PARTICLE INTEGRITY ANALYSIS

OYA ÖZDERE GÜLOL

ABSTRACT

High Temperature Reactors (HTRs) are among the candidates of the possible next generation nuclear plants. HTRs are expected to offer attractive features such as inherent safety, low cost of electricity generation, and short construction period. The safety performance of high temperature gas cooled reactors mainly relies on the quality and integrity of the coated fuel particles.

In this study, mechanisms that may lead to pressure vessel failure of a coated fuel particle are analyzed. In addition to internal pressure rise due to increasing concentration of fission product gases with burnup, mechanisms that stand out are migration of the kernel of the fuel particle and failure due to reactivity insertion accident.

The analysis is composed of mechanical and thermal parts. Mechanical analysis is performed to obtain stress distribution inside the load bearing layers. Particle failure fraction can be obtained from those stresses. Thermal analysis predicts the temperature distribution inside the coated fuel particle, from which internal pressure load on the structural layers is calculated.

This study consists of three major parts, which are the IAEA (International Atomic Energy Agency) Benchmark Study CRP-6 (Coordinated Research Project 6), kernel migration analysis and analysis of fuel failure due to reactivity insertion accident. CRP-6 study of the IAEA is used to benchmark the coated fuel particle model and its analysis methodology. The results obtained for the CRP-6 study are consistent with those of the other participants.

Kernel migration is one of the failure mechanisms of a coated fuel particle. The amount of migration of the kernel is calculated and the response of the load bearing layers are analyzed for different operating temperatures. Results of the analysis showed that the effect of kernel migration itself is not so critical on fuel failure as of pressure vessel failure.

Reactivity insertion accident is one of the design basis accidents of HTRs.

The scenario analyzed in this study assumes withdrawal of one of the control rods and consequent reactivity insertion. The power level reaches a significant value and then decreases slightly during the accident. The analysis shows that reactor can stabilize its power level at a constant value in the absence of reactivity control systems due to temperature feedbacks. Another result of the analysis is the significant increase in temperature as a result of positive reactivity insertion. Temperature increase as high as 200 °C may cause tensile stress on the SiC layer, which increases the failure probability of the coated fuel particle.

Keywords: nuclear reactor, nuclear fuel, high temperature reactor, coated fuel particle, TRISO, kernel migration

Advisor: Prof. Dr. Üner Çolak, Department of Nuclear Engineering, Hacettepe University.

KAPLANMIŞ YAKIT PARÇACIKLARININ BÜTÜNLÜK ANALİZİ

OYA ÖZDERE GÜLOL

ÖZ

Yüksek sıcaklıklı reaktörler gelecek vaad eden yeni nesil reaktörler arasında yer almaktadır. Kendinden güvenli olma, düşük maliyetli elektrik üretimi ve kısa inşa süreci bu reaktörlerin çekici özellikleri arasındadır. Yüksek sıcaklıklı reaktörlerin güvenlik performansı kaplanmış yakıt parçacıklarının bütünlüğüne ve kalitesine dayanmaktadır.

Bu çalışmada kaplanmış yakıt parçacıklarının hasar görmesine yol açabilecek bazı mekanizmalar analiz edilmiştir. Fisyon gazı miktarının yanmayla birlikte artması sonucu iç basıncın yükselmesi yanında öne çıkan mekanizmalar, yakıt çekirdeği göçü ve reaktivite ithali kazası nedeniyle yakıtın hasar görmesidir. Analiz mekanik ve ısıl bölümlerden oluşmaktadır. Mekanik analizde yük taşıyan yakıt katmanları içerisindeki gerilim dağılımları hesaplanmıştır. Parçacığın hasar görme olasılığı bu gerilim değerlerinden bulunabilmektedir. Isıl analizde ise parçacığın içerisindeki sıcaklık dağılımı hesaplanarak yük taşıyan katmanlar üzerindeki basınç yükü elde edilmiştir.

Bu çalışma üç ana bölümden oluşmaktadır. Bunlar, Uluslararası Atom Enerjisi Ajansı'nın (UAEA) yürütücülüğündeki Eşgüdümlü Araştırma Projesi 6 (CRP-6), yakıt çekirdeği göçü ve reaktivite ithali kazasında yakıtın hasar görmesi analizleridir. CRP-6 çalışması modelin doğrulanması ve kaplanmış yakıt parçacığı analiz metodolojisinin sınanması amacıyla gerçekleştirilmiştir. CRP-6 çalışmasının sonuçlarının, diğer katılımcı ülkelerin analiz sonuçları ile uyumlu olduğu görülmüştür.

Yakıt çekirdeği göçü kaplanmış yakıt parçacığının hasar görmesine sebep olabilecek bir olaydır. Yakıt çekirdeğinin ne kadar göç etmiş olduğu ve yük taşıyan katmanların buna tepkisi, değişik işletme sıcaklıkları için hesaplanmıştır. Analizler sonucunda, yakıtın zarar görmesinde yakıt çekirdeği göçünün kendisinden çok basınç kabı hasarının etken olduğu görülmüştür.

Reaktivite ithali kazası yüksek sıcaklıklı reaktörlerde tasarıma esas kazalardan biridir. Bu çalışmada, kontrol çubuklarından birinin çekilmesi sonucu meydana

gelen reaktivite ithali kazası ele alınmaktadır. Kazada reaktör gücü belli bir seviyeye ulaştıktan sonra azalmış ve sonunda dengeye gelmiştir. Analiz sonucunda gücün, reaktivite kontrol sistemleri devreye girmese de kendiliğinden dengeye gelebileceği görülmüştür. Bu durum yakıt ve yavaşlatıcının sıcaklık geribeslemesi özelliğinden kaynaklanmaktadır. Analizin bir sonucu da kazanın seyri sırasında yakıt sıcaklığının yaklaşık 200 °C kadar artmasıdır. Bu artış silikon karbür kaplama üzerinde çekme gerilmelerine yol açmakta ve parçacığın hasar görmesine sebep olabilmektedir.

Anahtar Sözcükler: nükleer reaktör, nükleer yakıt, yüksek sıcaklıklı reaktör, gaz soğutmalı reaktör yakıtı

Danışman: Prof. Dr. Üner Çolak, Nükleer Enerji Mühendisliği Bölümü, Hacettepe Üniversitesi.

ACKNOWLEDGMENTS

I would like to thank my thesis advisor Dr. Üner Çolak and co-advisor Dr. Bora Yıldırım for their helpful cooperation and guidance. I would like to thank Dr. Ediz Tanker for his valuable comments and guidance. I thank members of my graduate committee for their recommendations and the Department of Safety of Turkish Atomic Energy Authority for their support. I would also like to thank Dr. Mehmet Turanlı for his helpfullness. I would like to thank my family for encouraging and supporting me all my life.

Contents

List of Figures

List of Tables

Chapter 1

Introduction

High Temperature Reactors (HTRs) are among the candidates for the possible next generation nuclear plants. HTRs are expected to offer inherent safety characteristics, low cost of electricity generation, and a short construction period. Also they operate at high temperature ranges in which excess heat can be employed in industrial applications. Especially, the synergy of HTRs with hydrogen generation is a significant advantage.

There are two mainstream designs for HTRs: prismatic and pebble bed. Different fuel options such as uranium dioxide, uranium carboxide (UCO), and the (U, Pu) mixed oxide are considered. Such reactors can be used to eliminate weapon plutonium stockpiles and for nuclear waste transmutation. Thorium can be used in these reactors as fuel. Other prominent characteristics of HTRs include presence of only ceramic materials in the core, large graphite inventory as a heat sink and inherent safety characteristics.

The basic building blocks of HTR fuel elements are TRISO coated particles. A TRISO particle is made of a fuel kernel surrounded by a low density porous pyrolitic carbon (the buffer), a high density pyrolitic carbon, a SiC, and a high density pyrolitic carbon layer. The SiC layer acts as the primary pressure boundary. SiC can withstand temperatures up to 1800 °C. Beyond that temperature, thermal decomposition may be observed over extended time periods. The buffer layer is used to accommodate volume expansion due to swelling and fission products. The high density pyrolitic carbon layers protect the SiC layer, keep the SiC under compression, and act as a barrier against gaseous fission products.

In this study, main features provided by TRISO particles, their common failure modes, and basic elements for their performance analysis are discussed. The failure mechanisms for a coated fuel particle are analyzed in three parts. First, the finite element model developed for the analyses is presented. The model is benchmarked against the results of the IAEA Coordinated Research Project-6 (CRP-6) results. The

CRP-6 study, presented in Appendix A, is composed of simple and elaborate models of coated fuel particles under irradiation conditions. The study involves 14 cases. The particle integrity analysis of the participating countries involve finite element models as well as simplified models.

In the second part of the study the kernel migration phenomenon in HTTR fuel is analyzed. The reason for kernel migration is the high temperature gradient in the core causing carbon mass transport. Kernel migration analysis is composed of thermal and mechanical parts. Thermal analysis involves prediction of temperature distributions in the direction of kernel migration as well as the transverse direction. Mechanical analysis involves calculation of gas pressure inside the inner pyrolytic carbon and determination of stress distribution inside the layers. Results of kernel migration analyses are presented for two different particle surface temperatures and limiting burnup values, to illustrate its effect on particle failure.

The result of kernel migration analysis showed that the effect of kernel migration itself is not so critical on fuel failure. This is justified when temperature and stress values are compared for the same case with and without kernel migration. Pressure vessel failure is the primary mode of failure in high temperature and high burnup conditions. Coated fuel particle failure is more pronounced when pressure vessel failure is probable. However, the presence of kernel migration or thinning of the inner pyrolytic layer may facilitate the silicon carbide failure, which leads to particle failure.

The third part of the study involves reactivity insertion accident analysis. The finite element model is extended with numerical solution of point kinetics equations and analytical solution of temperature distribution inside the fuel. The point kinetics equations are used to determine the change of particle power in case of reactivity insertion. The time-dependent analytical solution of pebble temperature distribution is used to determine particle surface temperature and moderator temperature. Thermal analysis of the particle and the pebble produce temperature changes, which are employed in the point kinetics equations for calculating the feedbacks.

The reactivity insertion accident study shows that the HTR reactor is capable of stabilizing its power with feedbacks even when the shutdown or reactivity control

systems are unavailable, demonstrating the inherently safe characteristic of these reactors.

Modelling and analyses presented in this study are based on specific assumptions, and the results obtained are observed to be affected strongly by these assumptions.

In Chapter 2 of this thesis HTR fuel is introduced and its basic properties as well as its failure modes are described. A review of previous studies on HTR coated fuel particle is presented in Chapter 3. The present study is based on a finite element model of the coated fuel particle; therefore, an introduction to finite element analysis is included in Chapter 4. The finite element model developed for the coated fuel particle in this study is described in Chapter 5. Chapters 6 and 7 present applications of the model to kernel migration and reactivity insertion accident analyses, respectively. Conclusions and recommendations for future work can be found in Chapter 8. Supporting information are included in the appendices.

Chapter 2

High Temperature Reactor Fuel

2.1 High Temperature Reactors - History

The HTR utilizes an all-ceramic core, a graphite core structure, ceramic-coated particle fuels and completely ceramic fuel elements. The use of refractory core materials combined with a single phase inert helium coolant allows high coolant temperatures and results in a number of significant advantages, including high thermal efficiency, inherent safety advantages resulting from the low-power density and large thermal capacity of the core, absence of coolant phase changes and a prompt negative temperature coefficient.

Development of the HTR has proceeded in two directions: (a) the pebble bed concept in the Federal Republic of Germany and Russia (also in China and South Africa); and (b) the prismatic core in the United States, the United Kingdom, Japan and, recently with the GTMHR, also Russia. The fuel elements for the pebble bed system consist of 60 mm diameter spheres made up of a fuel-free carbon outer zone and an inner fueled region with coated particles uniformly dispersed in a graphitic matrix. Figure 2.1 presents the fuel element and the coated fuel particle.

The prismatic fuel element consists of a machined hexagonal graphite block 750 mm long and 350 mm across flats. Alternate fuel and coolant holes are drilled in a hexagonal array. Fuel rods, consisting of coated particles bonded in a close-packed array by a carbonaceous matrix, are stacked in the fuel holes. Figure 2.2 presents the structure of a prismatic fuel assembly.

Although fuel elements in the two HTR designs differ substantially, the basic fuel-containing unit, the coated particle, is essentially the same. HTR coated fuel particle has been developed internationally, irrespective of differences in reactor designs of different countries.

The following three experimental reactors have been developed and successfully operated:

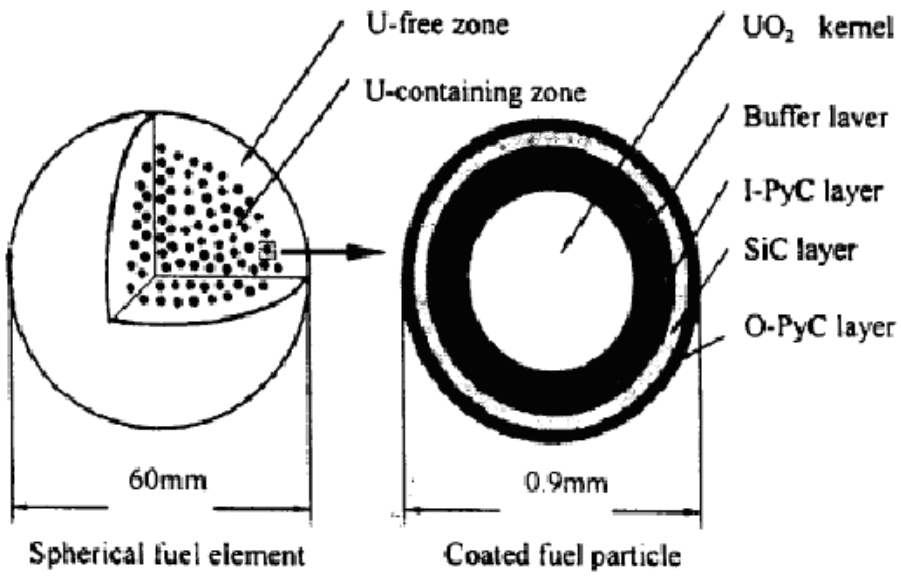

Figure 2.1: Pebble bed reactor coated fuel particle and fuel element [1]

- AVR (Arbeitsgemeinschaft Versuchsreaktor): 1967-1988, Pebble bed core, various (Th, U)C_2, (Th, U)O_2 BISO and (Th, U)O_2 TRISO with high enriched uranium as well as low enriched UO_2 TRISO coated particles; 46 MW_{th}/15 MW_e
- Peach Bottom 1 reactor in the US: 1967-1974, Core with tube elements, ThC_2, BISO; 115 MW_{th}/40 MW_e
- Dragon reactor in the UK: 1968-1975, Core with tube elements, various (UO_2 driver fuel), TRISO; 20 MW_{th}

Two commercial HTR plants were also constructed and operated: The 330 MW_e Fort St. Vrain (FSV) reactor, built by General Atomics Company for the Public Service Company of Colorado in the USA and the 300 MW_e Thorium High Temperature Reactor (THTR) at Schmehausen in Germany, built by Konsortium THTR (BBC-HRB-NUKEM) for Hochtemperatur-Kernkraftwerk GmbH (HKG). The first of these uses a prismatic core, while the second one has a pebble bed core.

- FSV: 1976-1989, 842 MW_{th}/330 MW_e; prismatic core; (Th, U)C_2/ThC_2, TRISO

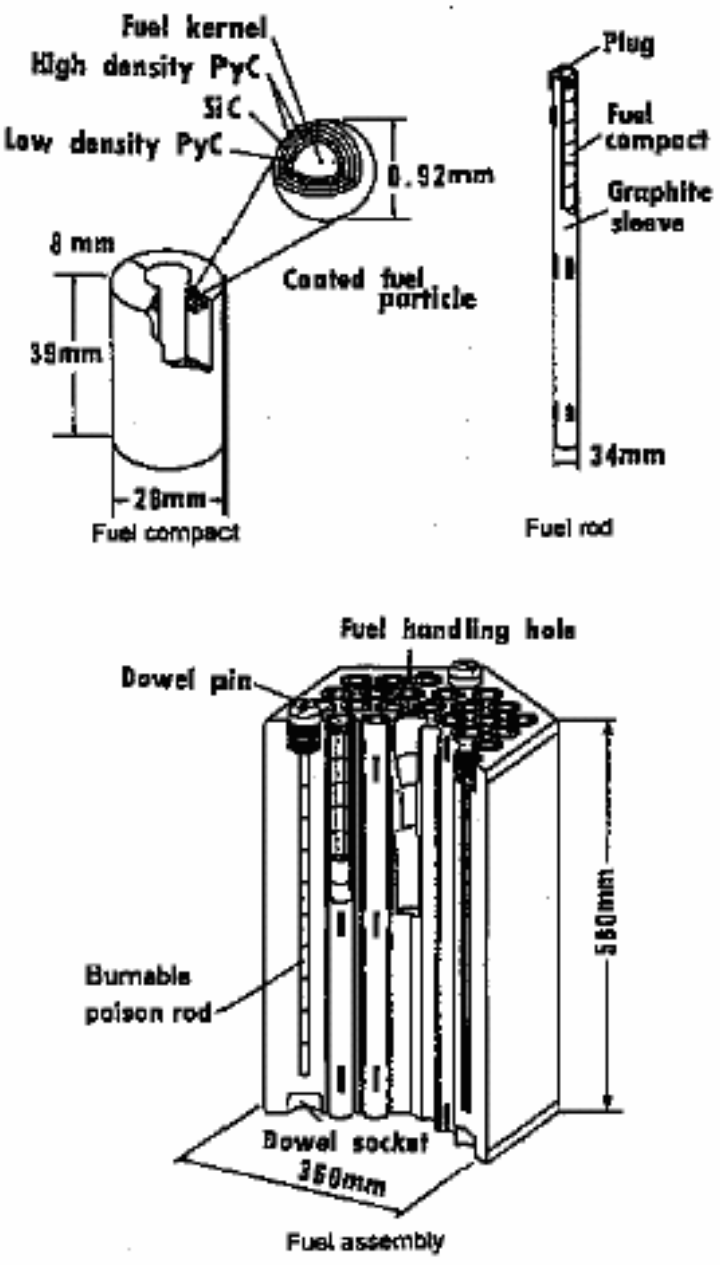

Figure 2.2: Structure of a prismatic fuel assembly [2]

- THTR: 1986-1989, 750 MW_{th}/300 MW_e; pebble bed core; (Th, U)O_2, BISO

This generation of HTRs has been operated on conventional steam cycle. However, advanced designs with direct-cycle helium turbines and reformers for industrial process heat was under active development in Germany over two decades. Comparable HTR research activities have been done in the United States and Russia as well as for a process heat HTR in Japan. In addition to the steam cycle HTR plants with prestressed concrete pressure vessels, such as the 300 MW_e THTR and 500 MW_e HTR-500 in Germany and the 330 MW_e FSV in the USA, small HTRs with steel pressure vessels are designed in both countries to achieve a so-called catastrophe-free design, irrespective of probability for all practical purposes. Examples of these so-called Modular HTRs are pebble bed core designs such as the 200 MW_{th} plant from Siemens/Interatom or the HTR-100 (250 MW_{th}) from BBC/HRB, and a General Atomics 250 MW_e (600 MW_{th}) design having a prismatic core. HTRs are designed such that the maximum fuel temperature in accidents remain below 1600 °C without active control mechanisms. These designs are intended to replace water-cooled reactors for electricity generation and to provide process heat for applications such as heavy oil recovery, coal gasification and liquefaction, etc.

The HTR development is still on the way in different countries: Japan has developed the experimental reactor HTTR with a thermal power of 30 MW, which became critical in November 1998 and is on its way to full power. Major specifications of the HTTR are: prismatic block core; low enriched UO_2; TRISO; He pressure: 4 MPa; He inlet/outlet temperature: 395/850 and 950 °C; steel containment. Figure 2.3 presents the vertical view of the HTTR core.

China has built the test reactor HTR-10. The HTR-10 with a thermal power of 10 MW presents the features of modular HTR design, which became critical at the end of the year 2000. The HTR-10 main design parameters are: modular HTR with a pebble bed core; low enriched fuel with 17% U-235 UO_2; TRISO; He pressure: 3 MPa; He inlet/outlet temperature: 250/300 and 700/900 °C. Reactor core and steam generator are housed in two steel pressure vessels, which are located side-by-side with a connecting vessel in between. Figure 2.4 presents the vertical view of HTR-10 reac-

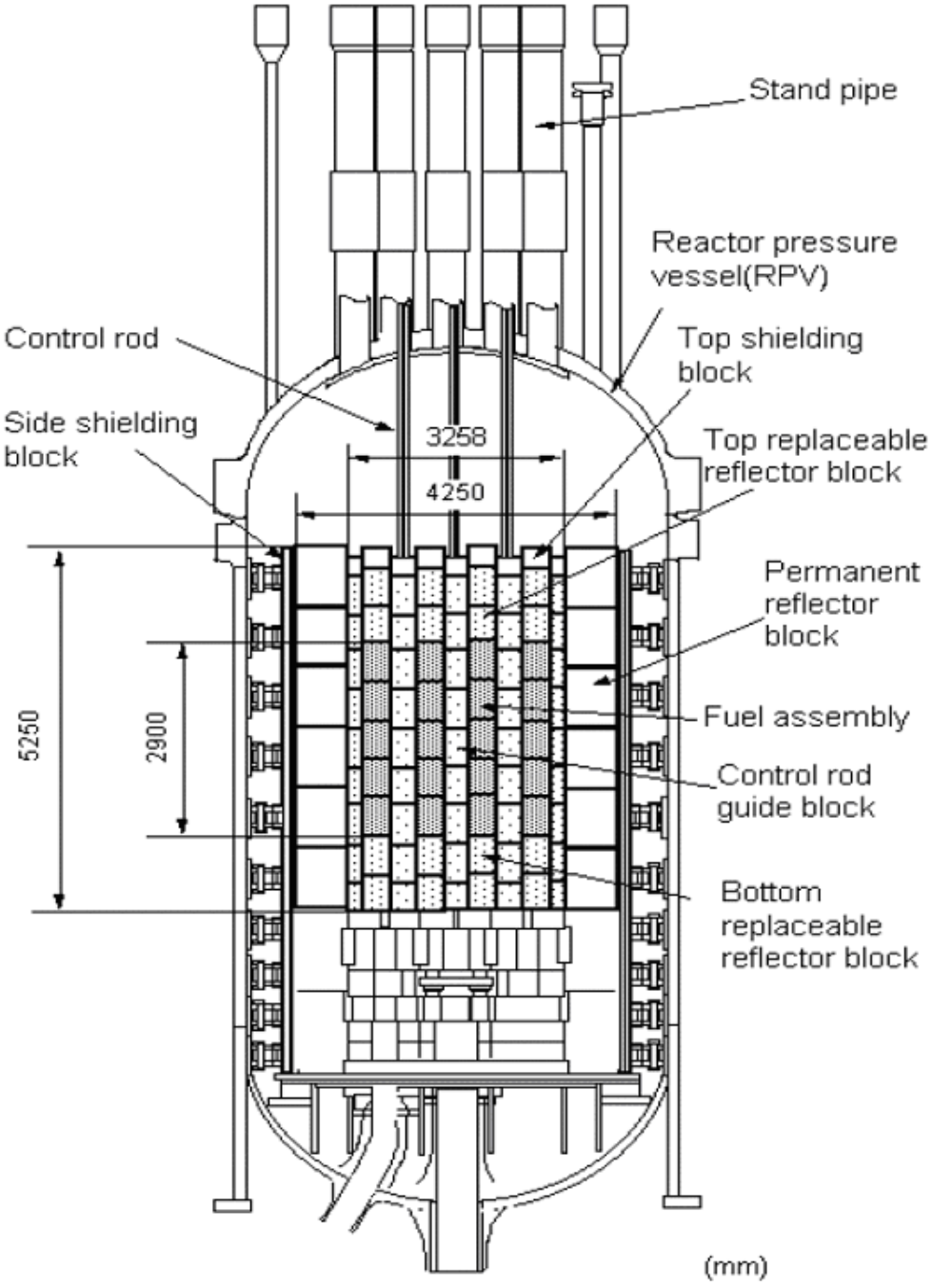

Figure 2.3: Vertical view of the HTTR core [2]

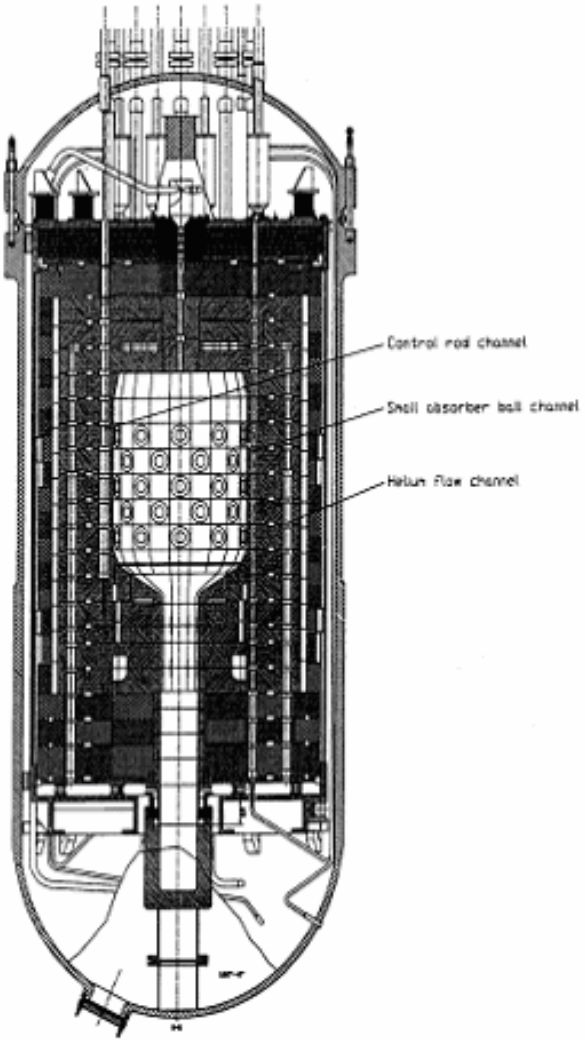

Figure 2.4: Vertical view of the HTR-10 core [2]

tor core.

In South Africa, ESKOM as the national utility sees a nuclear future in the HTR pebble bed system. ESKOM successfully operates the two-unit Koeberg PWR station, but it does not see light water reactors (LWRs) as the solution. Rather, it is putting its technical and financial resources behind a HTR project, which is seen as the best approach to take. The conceptual design is of a 120 MW_e Pebble Bed Modular Reactor (PBMR) with a direct cycle gas turbine [3]. Figure 2.5 presents the PBMR cross section.

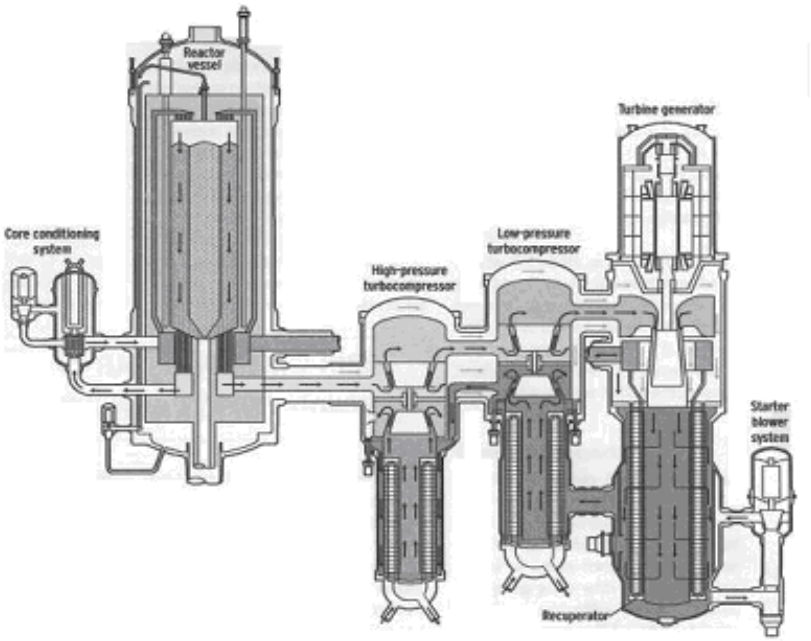

Figure 2.5: PBMR cross section [5]

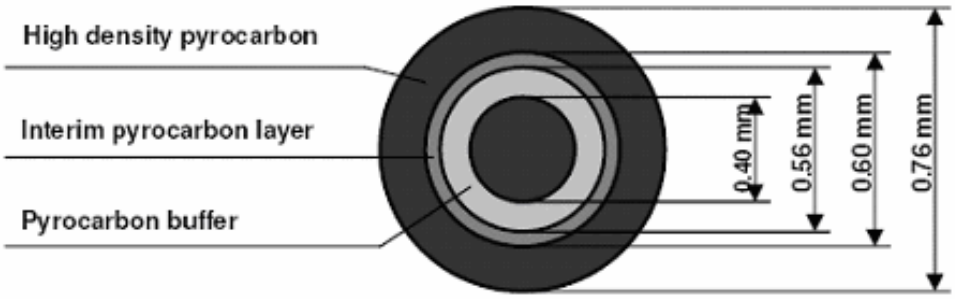

Figure 2.6: Diagrammatic view of BISO particle [6]

2.2 Coated Fuel Particle

Coated fuel particles (CFPs) are in themselves miniature fuel elements on the order of a millimeter in diameter. A commercial reactor core contains about 100 million individual coated fuel particles. The coatings provide the primary barrier to fission product release. The very small size of coated particles is an advantage in testing, because a statistically significant number of 'fuel elements' can be tested. The two coated particle types most commonly used are:

- the two-layer BISO coating with porous buffer and dense pyrolytic carbon (PyC, the so-called pyrocarbon)
- the four-layer TRISO coating with its interlayer of SiC between two layers of high-density isotropic PyC.

Figure 2.6 and 2.7 presents diagrammatic views of BISO and TRISO particles, respectively.

Both BISO and TRISO particles are capable of complete retention of gaseous fission products and iodine with properly designed and specified coatings. Intact TRISO particles also provide essentially complete retention of metallic fission products at current peak HTR design temperatures. Because diffusional release of certain metallic fission products, particularly cesium, strontium and silver does occur at elevated temperatures from BISO coatings, fuel elements with TRISO coated particles

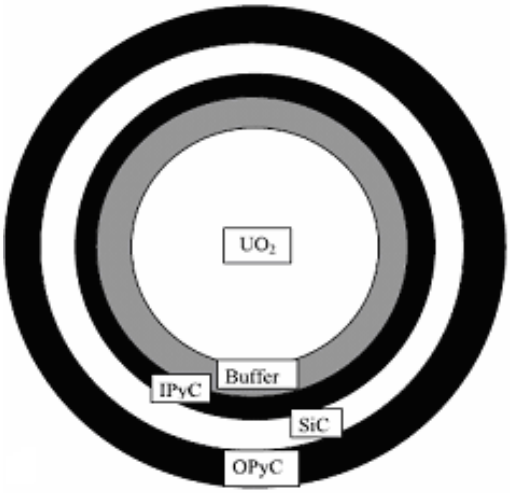

Figure 2.7: Diagrammatic view of TRISO particle [7]

are used (Fig. 2.7) in all modern HTR designs.

One of the attractive features of the HTR is its flexibility to use different fuel cycles. The thorium cycle with both separable and mixed fuel, the low-enriched uranium cycle and even cycles based on plutonium fissile particles are feasible. Fuel particles specific to each of these cycles have been successfully tested in prototype HTRs as well as in materials test reactors [3].

The TRISO coated fuel particle is described in the following subsections.

2.2.1 Kernel

The kernel contains the nuclear fuel. It may be composed of UO_2, PuO_2, ThO_2, UC_2, or their mixtures. The main function of the kernel is to produce the desired power for the reactor. Its composition determines the basic chemistry of the inner particle environment. Another function of the kernel for oxide-containing fuels is to bind the rare earth fission products as oxides to limit their migration to the coatings [4].

The fission gases and volatile fission products are largely contained by the coatings. However, fission gas retention by the kernel is important at low to moderate burnup levels, which is less than about 20% FIMA (Fissions per Initial Metal Atoms).

Up to this burnup and at normal operating temperatures, the kernel provides significant holdup of the fission gases krypton and xenon as well as the volatile species such as iodine and cesium. This retention aids in controlling particle pressure and is important for exposed kernels, as it greatly reduces the amount of fission products that are released to reactor internal components. Significant retention of some isotopes can occur even at accident temperatures.

As the kernel burnup increases, its ability to retain fission gases and volatile fission products can decrease, especially at higher temperatures. Designers often assume high release levels (up to 100%) of fission gases (very high burnup, 70% FIMA) at the end of life or for accident conditions.

An important design consideration for the kernel is the oxygen potential. Fission products from a fissioned uranium atom have an oxygen combining ability less than that of the original U, thus oxygen is available in the system to combine with other elements. The oxygen potential is determined by the amount of oxygen in the system and the affinity of particular elements for it. The oxygen potential determines which elements are successful in competing for the oxygen and which are not. The fission products, carbon, and uranium all compete for oxygen in this closed system and the system oxygen potential determines which elements are oxidized and which are not for a limited amount of oxygen.

In pure UO_2 fuel, the oxygen potential increases as a function of burnup and results in CO production. In CO production, the oxygen comes from the fissioning U in UO_2 and the carbon comes from the buffer. This CO increases the pressure in the particle. Details of pressure calculation and CO production are presented in Appendix B and Chapter 6, respectively. The total gas pressure is the sum of CO gas pressure and that of fission gases, which are mainly xenon and krypton. The krypton and xenon pressure depend on burnup, kernel gas retention and free volume in the buffer. Kernel gas retention diminishes with burnup and is often assumed to be nil for some accidents.

2.2.2 Buffer Layer

The buffer layer is composed of low density pyrolytic carbon. It surrounds the kernel and performs three main functions [4]:

- Fission product recoil attenuation: When uranium fissions, the resulting fission products are ejected at high velocity and are slowed down and stopped by the nearby material. Dense materials such as UO_2 and LWR fuel cladding limit the range of these recoils to roughly 10 microns. However, in low-density materials like carbon, the range of these recoils can be longer and they can cause significant local damage to the area they impact. The thickness of the dense outer layers in coated particle fuel is comparable to the recoil range. The buffer layer captures fission-produced recoils originating on the surface of the kernel and shields the IPyC from recoil damage.

- Void volume: The porous buffer layer provides free volume for accumulation of gases released from the kernel to control the particle pressure.

- Sacrificial layer: The buffer layer can distort to accommodate kernel swelling.

The thickness of the buffer layer affects the particle internal pressure. Too thin a buffer or a missing buffer layer will cause increased internal pressure, which can cause the particle to fail before the design burnup is reached. Thermal conductivity of the buffer is not as high as the other coatings, and too thick a buffer can raise kernel temperatures and thereby limit the power density. Thus, the buffer thickness is limited by pressure and heat transfer considerations. The buffer layer is not required for particle strength, but it must be able to hold the kernel away from the inner pyrolytic carbon layer. Fast flux and recoils can cause shrinkage and cracking of the buffer layer. While not desirable, a certain amount of shrinkage and cracking is acceptable.

2.2.3 Inner Pyrolytic Carbon Layer

The inner pyrocarbon layer (IPyC) is a higher density pyrolytic carbon layer deposited on the buffer layer. It serves several functions [4]:

- It protects the kernel from chlorine (in the form of HCl) liberated during SiC deposition. Without the IPyC layer, chlorine would easily migrate through the buffer layer to the kernel and react with the uranium to produce volatile chlorides. These chlorides would then transport the uranium out of the kernel and contaminate the coatings. During operation, fissioning of this uranium contamination would then damage the layers. Fissioning outside the kernel would also lead to increased fission product transport and release from the particle.

- It provides a smooth surface for SiC deposition since the buffer layer is too porous.

- It delays transport of fission products to the SiC layer. The IPyC layer retains gases well and effectively isolates the SiC from CO, which can attack the SiC at higher temperatures. The IPyC layer does not retain metals effectively.

- It can help maintain the SiC layer in compression. Depending on the IPyC/SiC layer bonding, the IPyC can place compressive forces on the SiC due to irradiation-induced shrinkage of the IPyC.

Good irradiation behavior requires that a pyrocarbon layer exhibit similar dimensional changes in the longitudinal and latitudinal directions for the fast fluence of interest. That is, it is desired that the carbon layer material and physical properties be isotropic. This can be achieved by ensuring that the deposited carbon has a random rather than a preferred macroscopic crystal orientation. A measurement of anisotropy in graphite is known as the Bacon Anisotropy Factor (BAF). BAF is an index to measure the anisotropy of the layer. A BAF of 1 is completely isotropic, greater than 1 implies increasing crystal orientation. The IPyC and OPyC layers are preferred to be isotropic and dense to minimize the neutron irradiation effects and to retain fission products. The forces acting on the IPyC layer during operation are gas pressure, irradiation-induced swelling/shrinkage, creep and thermal expansion. Due to anisotropy in the pyrocarbon shrinkage behavior, the shrinkage histories differ in the radial and tangential directions. The shrinkage in the radial direction reverses to

swelling at moderate fluence levels whereas shrinkage in the tangential direction continues to high fluence levels [8].

2.2.4 Silicon Carbide Layer

The silicon carbide (SiC) layer has two major functions [4]:

- It provides structural support to accommodate internal gas pressure.
- It is the primary fission product barrier. It retains gases and metals (except silver), but is subject to attack from palladium and rare earth elements.

The interaction of strains between the pyrocarbon layers and the SiC layer are important to SiC layer failure. Stress in the PyC layers is driven by gas pressure and irradiation-induced shrinkage and it is relieved by irradiation-induced creep. Both shrinkage and creep are temperature dependent. Stress in the SiC layer is driven by particle pressure and the relative stress distributions between the layers, which depend on material properties and layer bonding strengths. Two points could be emphasized:

- The particle should be designed so that the pyrocarbons keep the SiC in compression for as long as possible.
- Failure of a pyrocarbon layer will change the stress distributions and will change the SiC stress from compression to tension at a lower burnup. Failure probability is of primary concern for SiC layers under tension.

For design purposes, an intact SiC is assumed to retain all fission products at normal operating temperatures except for silver, which has a high release rate above 1100 °C. As the operating temperatures increase (>1250 °C) fission product attack on the SiC becomes more likely. The major concerns are the lanthanides (even at lower temperatures) and palladium. Design of the kernel can retain the lanthanides as oxides, but palladium (a noble metal) cannot be tied up and migrates (diffuses) to the SiC at higher temperatures where it attacks the layer. This behavior effectively limits the normal operating temperatures (below 1300 °C). At accident temperatures,

above 1600-1800 °C, fission product release quickly increases. Above about 2000 °C, thermal decomposition of SiC is a dominant failure mechanism.

2.2.5 Outer Pyrolytic Carbon Layer

The outer pyrocarbon layer (OPyC) is the final layer on the coated fuel particle and is the layer that binds the particle to the fuel form. Many of the performance factors associated with the OPyC are similar to those of the IPyC, especially irradiation stability, but there are differences. The OPyC [4]:

- Protects the SiC during fuel particle handling prior to fuel element fabrication.
- Provides a bonding surface for the matrix material.
- Compresses the SiC during irradiation.
- Acts as a final barrier to gaseous fission product release.
- Provides some isolation of the SiC from external chemical reactions.

The irradiation shrinkage and creep of the OPyC play similar roles as were outlined for the IPyC. The properties of interest of the OPyC are similar to those of the IPyC with the exception of permeation, which is important to matrix bonding rather than chlorine transport to the kernel.

2.3 Coated Fuel Particle Failure Modes

A review of the irradiation and safety testing of coated particle fuel reveals a number of potential failure mechanisms. These failure mechanisms are functions of temperature, burnup, fluence and the macroscopic temperature gradient across the particle. Mechanisms that may result in particle failure, which ultimately leads to fission product release, are [4]:

- Pressure vessel failure caused by internal gas pressure

- Pyrocarbon layer cracking and/or debonding due to irradiation-induced shrinkage that ultimately leads to the failure of the SiC layer
- Fuel kernel migration (amoeba effect), which leads to interactions with the coating layers
- Fission product/coating layer chemical interactions
- Matrix/OPyC interaction
- As-manufactured defects produced during fabrication of fuel particles or during pressing of fuel compacts/spheres
- Thermal decomposition of the SiC layer at very high temperatures
- Enhanced SiC permeability and/or SiC degradation under high burnup conditions
- Chemical attack in water and air ingress accidents
- Reactivity insertion accidents, which may cause fuel failure

2.3.1 Pressure Vessel Failure

Under irradiation, coated particle fuel is subjected to a number of forces that put stress on the TRISO coating. One of the mechanisms recognized the earliest is overpressure due to gas generation under irradiation. During irradiation, fission gases are released from the kernel to the porous buffer layer. The pressure that is generated exerts tensile forces on the layers of the particle. In addition to fission gases, in coated particle fuel with UO_2 kernels, there is excess oxygen released during fission. This excess oxygen will react with the buffer to form CO gas. Both the fission gases and CO production are primarily functions of burnup and temperature. Particles are generally manufactured with a large enough buffer to ensure that nominal particles do not fail by overpressure. Particle failure is postulated to occur in the event that, during the coating process particles are coated with an insufficient or no buffer layer.

2.3.2 Irradiation-induced IPyC Cracking and Debonding

Under irradiation, PyC shrinks in both radial and tangential directions. At modest fluences depending on the density, temperature and anisotropy of the material, PyC begins to swell in the radial direction and continues to shrink in the tangential direction. This behavior puts the PyC layers into tension in the tangential direction. At longer irradiation times, irradiation-induced creep relieves the tensile stress in the PyC layers. If the IPyC is strongly bonded to the SiC layer, the IPyC shrinkage provides a strong compressive stress in the SiC layer that offsets the tensile stresses generated by gas pressure. In fact, the particles are designed such that in intact particles the SiC layer remains in compression throughout the irradiation. If the shrinkage is much larger than anticipated, the tangential stresses in the PyC can be high enough to cause cracking in the layer. These cracks can lead to stress concentrations in the SiC layer high enough to cause failure of that layer. This failure mechanism has been attributed to high anisotropy in the PyC layer. In addition to irradiation-induced shrinkage, debonding at the IPyC/SiC interface has been observed in some experiments. This debonding is believed to be related to the nature of the IPyC/SiC interface. Weakly bonded coating layers can partially detach because of the tensile stresses generated by the PyC shrinkage under irradiation. A particle for which partial debonding of the IPyC from the SiC has occurred can develop relatively large tensile stresses in the SiC, which may lead to failure.

2.3.3 Kernel Migration

Kernel migration is defined simply as movement of the kernel in the coated fuel particle towards the TRISO coating. If the migration is excessive, the kernel will penetrate the TRISO coating leading to failure of the particle. Kernel migration is associated with carbon transport in the particle in the presence of a temperature gradient. In the fuel kernel equilibrium is established among C, UO_2 and CO. When there is a thermal gradient across the particle, the equilibrium is different on each side of the particle. The different equilibrium conditions lead to mass transport of carbon down

the temperature gradient. This movement of carbon appears in photomicrographs of fuel as a movement of the kernel up the temperature gradient, hence the name kernel migration. This phenomenon is strongly dependent on the temperature and the macroscopic temperature gradient in the fuel, with secondary dependence on burnup. It can also occur as solid-state carbon transport through carbide kernels. In prismatic cores with UO_2 fuel, where power densities in the particles are greater, the potential for kernel migration is greater. In pebble bed cores, the power densities and hence the thermal gradients are much smaller.

2.3.4 Fission Product/Coating Layer Chemical Interactions

Past irradiation experiments indicate that fission products can be transported from the kernel to the inner surface of the SiC where they interact and can damage and potentially fail the SiC layer. Migration of the fission products is thought to be a function of temperature and burnup as well as the temperature gradient. Although a complete understanding of the phenomenon is not available, the degree of fission product attack is generally correlated with the temperature and temperature gradient in the fuel. Thus, these fission product attack mechanisms are expected to play a more important role in prismatic reactors where power densities in the particle are larger than corresponding particles in a pebble bed reactor.

2.3.5 Matrix/OPyC Interaction

In early irradiations, high levels of OPyC failure due to cracking or debonding from the SiC layer were observed. These failures were attributed to intrusion of the low viscosity carbonaceous matrix material in the OPyC during compact fabrication followed by shrinkage under irradiation.

2.3.6 As-Manufactured Defects

In the absence of any of the above failure mechanisms, fission gas and metal release during irradiation is attributed to heavy metal contamination outside the SiC

layer and to initially defective particles. Initially defective particles can be the result of undetected defective particles that have not been removed during fabrication, particles that have been attacked during fabrication or irradiation by impurity metals (e.g. Fe), or particles that have failed as a result of damage during fuel element fabrication.

2.3.7 SiC Thermal Decomposition

At very high temperatures (above 1600-1800 °C), thermodynamics and data from high temperature heating tests show that the SiC layer undergoes thermal decomposition at a significant rate. This phenomenon is primarily a function of temperature and time, and has not played a major role in fuel failure at lower accident temperatures ($\sim$1600 °C) where safety testing has been routinely performed. Releases from fuel generally increase at temperatures above 1600 °C, with releases at 1800 °C being much greater, although the SiC behavior in the 1600-1800 °C range may be a combination of corrosion and decomposition.

2.3.8 Enhanced SiC Permeability and/or SiC Degradation

Although not formally a failure mechanism, there is some limited evidence that fast neutron fluence and/or burnup plays a role in the permeability or degradation of the SiC layer with respect to fission products during high temperature heating. Pebbles exposed to higher fluence ($4.6 \times 10^{25}\ n/m^2$) and higher burnup (14% FIMA) have exhibited a greater release of fission products (e.g. cesium) in heating tests than similar pebbles exposed to less severe conditions. This phenomenon could become more important as coated particle fuel is pushed to high burnup.

2.3.9 Chemical Attack (Ingress Accidents)

Under accident conditions, fuel may be exposed to air and/or water. Both will react with the carbon materials and the fuel kernels. Water ingress primarily affects exposed kernels, causing them to release a large fraction of their stored inventory. Reactions with the carbon materials are relatively modest at the temperatures of interest

and the resulting fuel damage is not extensive. Air is much more aggressive than water and reacts not only with the exposed kernels, but also with the carbon materials at a greater rate than water. Establishment of an air flow may result in significant fuel damage if allowed to continue unabated. In both cases, reactions with the carbon materials will release sorbed fission products.

2.3.10 Reactivity Insertion Accident

Sudden generation of high energies within the coated particle fuel can cause it to overheat, overpressure and break, thus releasing its fission products. This accident is not well defined, but results to date indicate that coated particle fuel will fail with energy depositions in the range of 1000-2000 kJ/kg. Much higher energies may cause the fuel element to be damaged.

Chapter 3

Literature Review

Early studies on coated fuel particle integrity analysis include simplified mathematical models of Prados and Scott [10] and Kaae [11, 12] for calculating stress distributions inside layers. Kaae's mathematical models calculate stress distributions for three and four layered, SiC coated fuel particle. Stresses are considered to result from pressure buildup inside the coatings due to fission, anisotropic dimensional changes inside the pyrocarbon layers due to fast neutron irradiation, thermal expansion and creep. The stress distribution inside the layers is calculated by analytical formulas. Kaae's model neglects the change in free volume inside the particle. Kaae indicated the importance of the buffer layer to accommodate empty volume for gaseous fission products. Also, variation in thicknesses of the layers do not change the stress distribution inside the pyrocarbon layers but do change the stress inside the SiC layer.

Martin's model [9, 7] is utilized in the STRESS3 code, which performs pressure vessel failure analysis and, when used with the statistical code STAPLE, takes changes in particle parameters and their effects on the failure probability into account. Martin's model also includes analytical formulations for stress distributions. Martin has pointed out the importance of isotropy in coated fuel particles, the effect of anisotropy manifesting itself in swelling and shrinkage of the pyrocarbon layers. Another point considered important is the lack of experimental data in predicting the change of anisotropy in material properties. Martin has also studied pyrocarbon material properties and contributed to the IAEA TECDOC 1154 [16], which presents material properties and deposition techniques used for pyrocarbons employed in research reactors.

Nabielek et al.'s PANAMA code calculates the stress distribution for the SiC layer with the thin shell approximation, and the CONVOL code uses an analytical solution based on a Weibull probability distribution for the SiC strength and the normal distribution for kernel and buffer layer thicknesses [17]. PANAMA is based on a pressure vessel failure model, where the SiC layer represents a simplified pressure vessel

assumed to fail as soon as internal gas pressure exceeds the tensile strength of the layer. The code assumes two modes of failure: pressure vessel and SiC corrosion [18, 19]. The FRESCO code describes diffusive fission product release from a single spherical fuel element under both normal and heating conditions. The model includes the effects of recoil release from the kernel and inventory buildup during neutron irradiation [20].

Early fuel performance models have, in some cases, shown good agreement with high-quality German fuel irradiation data, in which the failure rate was very low. However, irradiation tests on New Production Reactor (NPR) fuel conducted at Idaho National Engineering & Environmental Laboratory (INEEL) and the Oak Ridge National Laboratory in 1991 and 1992 revealed unexpectedly high fuel particle failure rates with fuel made in the US but which was nominally similar to German fuel [21]. The higher failure rates were not predicted by either the German or the US fuel performance models at the time. The experience demonstrated, at least in part, that coated particle fuel behavior was not sufficiently well understood and that the existing fuel performance models were not able to adequately capture some of the most relevant physical phenomena that occur in the particles during irradiation. Based on this less than satisfactory performance, it is clear that an improved fuel performance model is needed, which attempts to better represent the physics of fuel performance and the realistic irradiation environment. Finite element modeling is one such mechanism for representing the actual particle behavior.

Another CFP thermal and mechanical analysis code, ATLAS, has been developed by CEA in partnership with FRAMATOME. The ATLAS code is capable of performing thermal, mechanical and statistical calculations with the finite element technique [22, 23]. The models are one-dimensional for intact particles or particles with fully debonded layers and two dimensional for cracked, partially debonded or reshaped particles. Temperatures, displacements, stresses, strains and fission product concentrations can be calculated. ATLAS can also perform statistical processing of the results, taking into account the SiC failure mode and the uncertainities from fabrication, material properties and core data.

Korean Atomic Energy Research Institute's CFP analysis code, COPA, can

perform thermal and mechanical analyses as well as calculate failure probabilities. COPA also includes modules for calculating temperature distributions inside the pebble and graphite block. The COPA code considers fuel failure mechanisms such as pressure vessel failure, crack induced failure, SiC degradation and kernel migration [24].

Miller et al. at the Idaho National Laboratory developed an integrated mechanistic fuel performance model, the PARFUME, which performs multi-dimensional mechanical analyses by finite element techniques, thermal analysis and statistical calculations [26]. This code is capable of analyzing different phenomena such as shrinkage cracking, partial debonding, asphericity, kernel migration and SiC thinning [8, 27, 30]. Among current capabilities of the code are: various options for calculating CO production and fission product gas release, a thermal model that calculates a time-dependent temperature profile through a pebble sphere or a prismatic fuel block as well as through the layers of each analyzed particle, simulation of multi-dimensional particle behavior associated with cracking in the IPyC layer, partial debonding of the IPyC from the SiC, particle asphericity, kernel migration, thinning of the SiC caused by interaction of fission products with the SiC, two independent methods for determining particle failure probabilities, a model for calculating release-to-birth (R/B) ratios of gaseous fission products that accounts for particle failures and uranium contamination in the fuel matrix, and the evaluation of an accident condition [28, 29].

Another fuel performance model, the TIMCOAT code, has been developed at Massachusetts Institute of Technology, USA. TIMCOAT can model coated fuel particle behavior for pebble bed and prismatic designs. Fission gas release, pyrocarbon dimensional change and creep, temperature profile in the fuel particle and chemistry calculations are combined in TIMCOAT to perform mechanical analyses for obtaining the mechanical and chemical state of the fuel particle. TIMCOAT also has an interface with the VSOP code for obtaining flux and power levels. Chemistry calculations in TIMCOAT is still under development. The calculations include SiC degradation, SiC thermal decomposition, kernel/coating interaction and Ag diffusion [31].

Wang has developed an integrated fuel performance model for studying the

coated fuel particle mechanical behavior. He has employed TIMCOAT in his master's thesis and benchmarked his model with finite element calculations of INEEL, HTTR first loading fuel and NPR experiments [32].

Diecker has studied the developments of the chemistry model of the TIMCOAT code in her M.Sc. thesis [33] and added palladium attack on the SiC layer to fracture mechanics failure model of the TIMCOAT.

Gas pressure is the main contributor to the stress on the load bearing layers. Studies of Gelbard [34] presents analytical modelling of fission gas releases for multilayer coated fuel particles. Bernard et al. [35] and Lösönen [36] present models for calculation of gas release that can be applied for coated particle fuel.

There also exist studies on improving the performance of HTRs. These studies include material analysis for ZrC use instead of SiC and new fuel designs for higher temperature and burnup conditions.

Advanced Gas Reactor (AGR) fuel design considers previous studies and experimental results on German fuel particle. The fuel of AGR is UCO and coating techniques of TRISO has been studied in detail to adopt in AGR fuel design [29].

Recent studies involve analysis of new designs such as the VHTR which will operate at a higher temperature range than the HTR and which employ the coated fuel particle. An assessment has been performed using the PARFUME code to quantitatively evaluate the challenges associated with high temperature and high burnup conditions applied to the TRISO coated particle fuel. Maki et al. [38] studied a number of known fuel failure and fission product release mechanisms that are temperature and burnup dependent. These mechanisms include: thermomechanical response of PyC, fission gas release and CO production, amoeba effect, metallic fission product diffusion and Pd attack on the SiC. The study involves comparison of the PARFUME code results with the behavior of German coated fuel particle in the upper operating limit. The study points out the differences between the two models and the necessity of further analysis for VHTR operating ranges.

Another study by Snead et al. [39] collects the SiC material properties for irradiated and unirradiated cases. The study also points out the necessity of data for

higher temperature ranges such as VHTR operating temperatures and for collecting material properties of SiC and ZrC in a handbook.

In advanced fuel designs, the SiC layer has sometimes been replaced by ZrC. ZrC coating layer is a candidate to replace the SiC layer for improving particle stability at higher temperatures. In addition, ZrC has higher resistance to chemical attack compared to SiC. Irradiation tests on ZrC for obtaining the material behavior are the subject of current studies [37].

Chapter 4

The Finite Element Method

Many problems in engineering and applied science are governed by differential or integral equations. The finite element method is a numerical procedure for obtaining approximate solutions to many of the problems encountered in engineering analysis.

In the finite element method (FEM), a complex region defining a continuum is discretized into simple geometric shapes called elements. The properties and the governing relationships are assumed over these elements and expressed mathematically in terms of unknown values at specific points in the elements called nodes. An assembly process is used to link the individual elements to the given system. When the effects of loads and boundary conditions are considered, a set of linear or nonlinear algebraic equations is usually obtained. Solution of these equations gives the approximate behavior of the continuum or system. The continuum has an infinite number of degrees of freedom (DOF), while the discretized model has a finite number of DOF. This is the origin of the name, finite element method. The number of equations is usually rather large for most real-world applications of the FEM, and requires the computational power of the digital computer. Finally, plots and numerical results are output to provide engineers with insights to the behavior of the model [48]. Finite element method can handle complex geometries.

The finite element model of the present study involves ceramic brittle materials, and the calculations are performed in the elastic region. Fracture of the coated fuel particle layers is expressed in terms of probabilistic fracture mechanics. Weibull distribution is employed in probability analysis. Details on Weibull distribution is presented in Appendix C.

Basic equations regarding the finite element solution are presented in this chapter [49].

4.1 Basic Equations

A state of stress exists in a body acted upon by external forces. If these external forces act over the surface of the body, they are called surface forces; if they are distributed throughout the volume, they are called body forces. Pressure is the surface force in our case.

The components of normal stress are denoted as $\sigma_x, \sigma_y, \sigma_z$ and the components of shear stress $\sigma_{xy}, \sigma_{yz}, \sigma_{zx}$. Normal stress carries a single subscript to indicate that the stress acts on a plane normal to the axis in subscript direction. The first letter of the double subscript on shear stress indicates that the plane on which the stress act is normal to the axis in the subscript direction; the second letter designates the coordinate direction in which the stress acts. Six quantities $\sigma_x, \sigma_y, \sigma_z, \sigma_{xy}, \sigma_{yz}, \sigma_{zx}$ describe the stress at a point.

When an elastic body is subjected to a state of stress, it is assumed that particles will move in a small amount and the body in its deformed state remains perfectly elastic, so that its deformation disappears when the stress is removed. If the displacement in the deformed body is represented by three components u, v and w parallel to the coordinates x, y and z, respectively, the strain at a point in the body may be expressed as:

$$\epsilon_x = \frac{\partial u}{\partial x} \qquad \epsilon_y = \frac{\partial v}{\partial y} \qquad \epsilon_z = \frac{\partial w}{\partial z} \tag{4.1}$$

$$\epsilon_{xy} = \frac{\partial u}{\partial y} + \frac{\partial v}{\partial x} \qquad \epsilon_{xz} = \frac{\partial u}{\partial z} + \frac{\partial w}{\partial x} \qquad \epsilon_{yz} = \frac{\partial v}{\partial z} + \frac{\partial w}{\partial y} \tag{4.2}$$

The strain ϵ_x is defined as the unit elongation of the body and the shearing strain ϵ_{xy} is defined as the distortion of the angle between $x - z$ and $y - z$ planes.

The six components of stress are related to the six components of strain through a proportionality matrix [C] containing 36 terms for a general anisotropic material, called Hooke's law:

$$\begin{Bmatrix} \sigma_x \\ \sigma_y \\ \sigma_z \\ \sigma_{xy} \\ \sigma_{yz} \\ \sigma_{zx} \end{Bmatrix} = \begin{bmatrix} C_{11} & \dots & \dots & \dots & \dots & C_{16} \\ \vdots & \ddots & & & & \vdots \\ \vdots & & \ddots & & & \vdots \\ \vdots & & & \ddots & & \vdots \\ \vdots & & & & \ddots & \vdots \\ C_{61} & \dots & \dots & \dots & \dots & C_{66} \end{bmatrix} \begin{Bmatrix} \epsilon_x \\ \epsilon_y \\ \epsilon_z \\ \epsilon_{xy} \\ \epsilon_{yz} \\ \epsilon_{zx} \end{Bmatrix} \tag{4.3}$$

Because the matrix [C] is symmetric, only 21 coefficients can be identified. Using matrix notation, Equation 4.3 can be written as:

$$\{\sigma\} = [C] \ \left\{\epsilon^{el}\right\} \tag{4.4}$$

where ϵ^{el} represents the elastic strain. By inversion, the strains may be expressed as:

$$\left\{\epsilon^{el}\right\} = [C]^{-1} \{\sigma\} = [D] \{\sigma\} \tag{4.5}$$

Taking thermal strain and creep vectors into account gives the following relationship [46]:

$$\left\{\epsilon^{el}\right\} = \{\epsilon\} - \left\{\epsilon^{th}\right\} - \{\epsilon^{cr}\} \tag{4.6}$$

where $\left\{\epsilon^{el}\right\}$ is the elastic strain vector, which causes stress as defined in previous equations. $\left\{\epsilon^{th}\right\}$ is the thermal strain and $\{\epsilon^{cr}\}$ is the creep strain vector [47]. $\{\epsilon\}$ is the total strain vector, which is the strain measured by a strain gauge. Thermal strain is defined as:

$$\left\{\epsilon^{th}\right\} = \Delta T \begin{Bmatrix} \alpha_x \\ \alpha_y \\ \alpha_z \\ 0 \\ 0 \\ 0 \end{Bmatrix} \tag{4.7}$$

where

α_i = coefficient of thermal expansion in direction i

$\Delta T = T - T_{ref}$

T = temperature at the point in question

T_{ref} = reference temperature.

Creep is also considered in the coated fuel particle model. The creep equation for finite element analysis of coated fuel particle is of the form:

$$\dot{\epsilon_{cr}} = K\ \sigma \tag{4.8}$$

where K is the creep constant presented in references [25, 16] and $\dot{\epsilon_{cr}}$ is the change in equivalent creep strain with time. The creep strain rate is integrated over time to calculate the creep strain. There exist different types of equations representing creep and creep rate in ANSYS. Norton's creep rate model is the consistent representation of the real creep rate of pyrolytic carbons. It is of the form:

$$\dot{\epsilon_{cr}} = C_1\ \sigma^{C_2}\ e^{-C_3/T}, \qquad C_1 > 0 \tag{4.9}$$

where

$\dot{\epsilon_{cr}}$ = change in equivalent creep strain with time

σ = equivalent stress

T = absolute temperature.

To use Norton's creep rate model, $C_1 = K,\ C_2 = 1$ and $C_3 = 0$ are assumed.

The matrix [C] of equation 4.3 is termed the material stiffness matrix, while its inverse [D] is the material flexibility matrix. These relations between stress and strain take on less complex forms if the elastic body is homogenous and isotropic. Homogenous means the material has the same physical properties at any part. Isotropy is defined as the independency of material property from directions.

In our case all the modelled layers are homogenous. Also, load bearing layers subjected to mechanical analysis have isotropic material properties.

For homogenous isotropic materials, only two physical constants are required to express all coefficients in Hooke's law; these are Young's modulus E and

Poisson's ratio ν. In terms of these constants the matrices in Hooke's law are as follows:

$$[C] = \frac{E}{(1+\nu)(1-2\nu)} \begin{bmatrix} 1-\nu & \nu & \nu & 0 & 0 & 0 \\ \nu & 1-\nu & \nu & 0 & 0 & 0 \\ \nu & \nu & 1-\nu & 0 & 0 & 0 \\ 0 & 0 & 0 & \frac{1-2\nu}{2} & 0 & 0 \\ 0 & 0 & 0 & 0 & \frac{1-2\nu}{2} & 0 \\ 0 & 0 & 0 & 0 & 0 & \frac{1-2\nu}{2} \end{bmatrix} \tag{4.10}$$

$$[D] = [C]^{-1} \frac{1}{E} \begin{bmatrix} 1 & -\nu & -\nu & 0 & 0 & 0 \\ -\nu & 1 & -\nu & 0 & 0 & 0 \\ -\nu & -\nu & 1 & 0 & 0 & 0 \\ 0 & 0 & 0 & 2(1+\nu) & 0 & 0 \\ 0 & 0 & 0 & 0 & 2(1+\nu) & 0 \\ 0 & 0 & 0 & 0 & 0 & 2(1+\nu) \end{bmatrix} \tag{4.11}$$

The equilibrium of an elastic body in a state of stress is governed by three partial differential equations for the stress components. These equations may be derived by writing force balances for an elemental volume of the material acted upon by body forces F_x, F_y and F_z per unit volume. Forces acting on the element are calculated by assuming that the sides of the element have infinitesimal area and by multiplying the stresses at the centroid of the element by the area of the sides. Summing forces per unit volume in the three coordinate directions gives:

$$\begin{aligned} \frac{\partial \sigma_x}{\partial x} + \frac{\partial \sigma_{xy}}{\partial y} + \frac{\partial \sigma_{xz}}{\partial z} + F_x = 0 \\ \frac{\partial \sigma_{xy}}{\partial x} + \frac{\partial \sigma_y}{\partial y} + \frac{\partial \sigma_{yz}}{\partial z} + F_y = 0 \\ \frac{\partial \sigma_{xz}}{\partial x} + \frac{\partial \sigma_{yz}}{\partial y} + \frac{\partial \sigma_z}{\partial z} + F_z = 0 \end{aligned} \tag{4.12}$$

A balance of moments about three coordinate directions shows that $\sigma_{xy} = \sigma_{yx}$ and so on. Boundary conditions for the equilibrium equations 4.12 may be found by considering the external surface forces acting on the body. If the components of

these unit forces are denoted by $\overline{\sigma}_x$, $\overline{\sigma}_y$ and $\overline{\sigma}_z$, at any point on the surface of the body:

$$\begin{aligned} \overline{\sigma}_x &= \sigma_x\, l + \sigma_{xy}\, m + \sigma_{xz}\, n \\ \overline{\sigma}_y &= \sigma_{xy}\, l + \sigma_y\, m + \sigma_{yz}\, n \\ \overline{\sigma}_z &= \sigma_{xz}\, l + \sigma_{yz}\, m + \sigma_z\, n \end{aligned} \tag{4.13}$$

where l, m and n are the direction cosines of the outward normal to the surface at point of interest.

The definition of strain in terms of derivatives of displacement given in equations 4.1 lead to other relations between strain and displacement that must be satisfied. These relations are called compatibility conditions and can be derived from differentiation of equations 4.1.

Hooke's law is used to express stress components in terms of strain components, then equations 4.1 are employed to express strain in terms of displacements that produce differential equations to be solved. These differential equations can be converted to algebraic equations by assuming that displacements are known functions, e.g. polynomials, of coordinates, with unknown coefficients to satisfy continuity and other conditions. For example, if the finite elements are triangles (in 2D) then the displacements at the corners of each triangle, called nodes, can be the unknowns and the displacements anywhere inside a triangle can be expressed in terms of the displacements at the corners. If the functions are chosen as bilinear polynomials then the displacements are continuous everywhere inside the domain (not just the triangular element). If higher degree polynomials or other functions are employed the displacements will be continuous only at the nodes. In this case, the equations to be solved to determine the coefficients are derived using variational techniques.

In the analyses the spherical coated fuel particle is assumed to be subjected to axisymmetric loads. Therefore, the geometry of the model is essentially two dimensional. In finite element analysis, plane strain elements are used to represent a slice (of unit thickness) of a structure in which only the strain components ϵ_x, ϵ_y and ϵ_{xy} are non-zero in the $x - y$ plane. Since the geometry is symmetric around a central axis in our case, the effect of the third dimension is taken into account using axisymmetric

elements. The stress and strain components, Hooke's law, equilibrium conditions and differential equations for displacement are presented below in case of plane strain.

Stress components:

$$\{\sigma\} = \{\sigma_x \ \sigma_y \ \sigma_{xy}\}^T \tag{4.14}$$
$$\sigma_z = \nu \ (\sigma_x + \sigma_y)$$

Strain components:

$$\{\epsilon\} = \{\epsilon_x \ \epsilon_y \ \epsilon_{xy}\}^T \tag{4.15}$$

Hooke's law:

$$\{\sigma\} = [C] \ \{\epsilon\} \tag{4.16}$$

$$[C] = \frac{E}{(1+\nu)(1-2\nu)} \begin{bmatrix} 1-\nu & \nu & 0 \\ \nu & 1-\nu & 0 \\ 0 & 0 & \frac{1-2\nu}{2} \end{bmatrix} \tag{4.17}$$

Static equilibrium:

$$\begin{aligned} \frac{\partial \sigma_x}{\partial x} + \frac{\partial \sigma_{xy}}{\partial y} + \ F_x = 0 \\ \frac{\partial \sigma_{xy}}{\partial x} + \frac{\partial \sigma_y}{\partial y} + \ F_y = 0 \\ \frac{\partial \sigma_z}{\partial z} + \ F_z = 0 \end{aligned} \tag{4.18}$$

Differential equations for displacements:

$$\begin{aligned} \nabla^2 u + \frac{1}{1-2\nu} \ \frac{\partial}{\partial x} \left(\frac{\partial u}{\partial x} + \frac{\partial v}{\partial y} \right) + \frac{F_x}{\mu} = 0 \\ \nabla^2 v + \frac{1}{1-2\nu} \ \frac{\partial}{\partial y} \left(\frac{\partial u}{\partial x} + \frac{\partial v}{\partial y} \right) + \frac{F_y}{\mu} = 0 \end{aligned} \tag{4.19}$$

with boundary conditions:

$$\begin{aligned} T_x^* = \lambda \psi l + \mu \left[2 \frac{\partial u}{\partial x} \ l + \left(\frac{\partial u}{\partial y} + \frac{\partial v}{\partial x} \right) m \right] \\ T_y^* = \lambda \psi m + \mu \left[2 \frac{\partial v}{\partial y} \ m + \left(\frac{\partial v}{\partial x} + \frac{\partial u}{\partial y} \right) l \right] \end{aligned} \tag{4.20}$$

where T^*s are external surface traction forces and ψ is the strain invariant given by:

$$\psi = \epsilon_x + \epsilon_y \tag{4.21}$$

Coated fuel particle is modelled as an axisymmetric solid. This is similar to plane strain in the $x - y$ (here $r - z$, where z is the symmetry axis) plane except that the strain perpendicular to the $r - z$ plane, ϵ_ϕ, is not zero, along with ϵ_r, ϵ_z and ϵ_{rz}. The stress and strain components, and Hooke's law are presented below in the axisymmetric case.

Stress components:

$$\{\sigma\} = \{\sigma_r \ \sigma_z \ \sigma_\phi \ \sigma_{rz}\}^T \tag{4.22}$$

Strain components:

$$\{\epsilon\} = \{\epsilon_r \ \epsilon_z \ \epsilon_\phi \ \epsilon_{rz}\}^T \tag{4.23}$$

Hooke's law:

$$\{\sigma\} = [C] \ \{\epsilon\} \tag{4.24}$$

$$[C] = \frac{E}{(1+\nu)(1-2\nu)} \begin{bmatrix} 1-\nu & \nu & \nu & 0 \\ \nu & 1-\nu & \nu & 0 \\ \nu & \nu & 1-\nu & 0 \\ 0 & 0 & 0 & \frac{1-2\nu}{2} \end{bmatrix} \tag{4.25}$$

The displacements are two dimensional, as in the plane strain case. However, solution of the related equations also yield the circumferential stress perpendicular to the plane of solution, σ_ϕ.

4.2 Finite Element Formulations

Displacements in a finite element can be expressed in terms of those of its nodes. In the following, an example is given for a triangular element, in which the

displacements are assumed to be expressed as bilinear polinomial functions of the coordinates. Since the coated fuel particle is modelled as axisymmetric, equations are in cylindrical coordinates. Using the triangular shape of an element with the nodes i, j, m as presented in Figure 4.1, the nodal displacements are defined by two components as [50]:

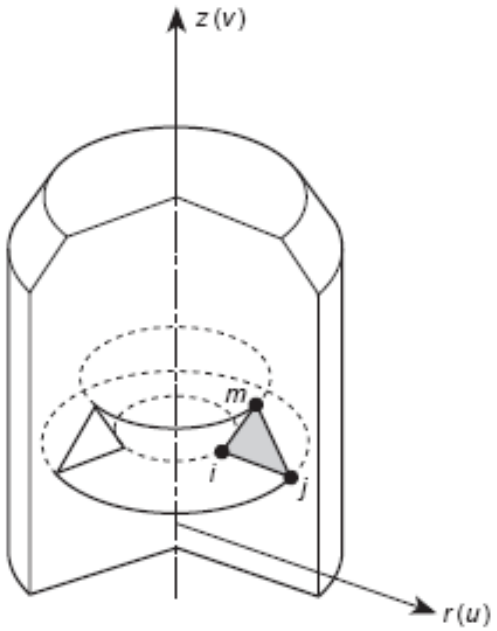

Figure 4.1: Element of an axisymmetric solid [50]

$$\{a\}_k = \left\{ \begin{array}{c} u_k \\ v_k \end{array} \right\}, \qquad k \; = \; i, j, m \tag{4.26}$$

and the displacement by the vector:

$$\{a\}^e = \left\{ \begin{array}{c} \{a\}_i \\ \{a\}_j \\ \{a\}_m \end{array} \right\}^e \tag{4.27}$$

where e indicates a single element.

Displacement at each point within an element need to be defined by these six

values. The simplest representation is given by two linear polynomials:

$$\begin{aligned} u &= \alpha_1 \ + \ \alpha_2 \, r \ + \ \alpha_3 \, z \\ v &= \alpha_4 \ + \ \alpha_5 \, r \ + \ \alpha_6 \, z \end{aligned} \tag{4.28}$$

The six constants α can be evaluated by solving two sets of three simultaneous equations, which will arise if the nodal coordinates are inserted and the displacements equated to the appropriate nodal displacements. For example:

$$\begin{aligned} u_i &= \alpha_1 + \alpha_2 \, r_i + \alpha_3 \, z_i \\ u_j &= \alpha_1 + \ \alpha_2 \, r_j + \alpha_3 \, z_j \\ u_m &= \alpha_1 + \alpha_2 \, r_m + \alpha_3 \, z_m \end{aligned} \tag{4.29}$$

α_1, α_2 and α_3 can be solved in terms of nodal displacement u_i, u_j, u_m and displacements become:

$$\begin{aligned} u \ = \ \frac{1}{2\Delta}\Big[(a_i + b_i \, r + c_i \, z)u_i \ &+ \ (a_j + b_j \, r + c_j \, z)u_j \ + \\ &+ \ (a_m + b_m \, r + c_m \, z)u_m\Big] \end{aligned} \tag{4.30}$$

in which

$$\begin{aligned} a_i &= r_j z_m \ - \ r_m z_j \\ b_i &= z_j \ - \ z_m \ = \ z_{jm} \\ c_i &= r_m \ - \ r_j \ = \ r_{mj} \end{aligned} \tag{4.31}$$

with the other components obtained by a cyclic permutation of subscripts in the order i, j, m and where

$$2\Delta = det \begin{vmatrix} 1 & r_i & z_i \\ 1 & r_j & z_j \\ 1 & r_m & z_m \end{vmatrix} = 2 \times \text{area of triangle } ijm \tag{4.32}$$

Similarly for v:

$$\begin{aligned} v \ = \ \frac{1}{2\Delta}\Big[(a_i + b_i \, r + c_i \, z)v_i \ &+ \ (a_j + b_j \, r + c_j \, z)v_j \ + \\ &+ \ (a_m + b_m \, r + c_m \, z)v_m\Big] \end{aligned} \tag{4.33}$$

Equations 4.30 and 4.33 can be represented in the form:

$$\{p\} = \left\{ \begin{array}{c} u \\ v \end{array} \right\} = \Big[[I]N_i \; [I]N_j \; [I]N_m \Big] \; \{a\}^e \tag{4.34}$$

with

$$N_k \; = \; \frac{a_k + b_k r + c_k z}{2\Delta}, \qquad k \; = \; i, j, m \tag{4.35}$$

and $[I]$ is a two by two unit matrix. Equations 4.34 with 4.35 and 4.27 with 4.26 express the displacement at any point within the triangular finite element in terms of the displacements of its corners.

Four components of strain have to be considered. The strain vector defined below lists the strain components involved and defines them in terms of displacement at a point.

$$\{\varepsilon\} = \left\{ \begin{array}{c} \epsilon_r \\ \epsilon_z \\ \epsilon_\phi \\ \epsilon_{rz} \end{array} \right\} \; = \; \left\{ \begin{array}{c} \frac{\partial u}{\partial r} \\ \frac{\partial v}{\partial z} \\ \frac{u}{r} \\ \frac{\partial u}{\partial z} + \frac{\partial v}{\partial r} \end{array} \right\} \; = \; [S] \; \{p\} \tag{4.36}$$

Using the displacement function in Equations 4.34 and 4.31

$$\{\varepsilon\} = [B] \, \{a\}^e = \Big[[B]_i \; [B]_j \; [B]_m \Big] \, \{a\}^e \tag{4.37}$$

in which

$$[B]_k = \left[\begin{array}{cc} \frac{\partial N_k}{\partial r} & 0 \\ 0 & \frac{\partial N_k}{\partial z} \\ \frac{N_k}{r} & 0 \\ \frac{\partial N_k}{\partial z} & \frac{\partial N_k}{\partial r} \end{array} \right] \; = \; \frac{1}{2\Delta} \left[\begin{array}{cc} b_k & 0 \\ 0 & c_k \\ \frac{a_k}{r} + b_k + \frac{c_k z}{r} & 0 \\ c_k & b_k \end{array} \right], \qquad k \; = \; i, j, m \tag{4.38}$$

With the $[B]$ matrix involving the coordinates r and z, the strains are not constant within an element as in the plane stress or strain case. This strain variation is due to the ϵ_ϕ term. If the imposed nodal displacements are such that u is proportional to r then indeed the strains will all be constant.

The stiffness matrix of the element (not to be confused with the material stiffness matrix), which is used to compute the effect of node j on node i of element e, can be computed according to the relationship

$$[K]_{ij}^{e} = 2\pi \int [B]_{i}^{T} [C] [B]_{j} \, r dr \, dz \tag{4.39}$$

where $[B]$ is given by Equation 4.38 and $[C]$ is given by Equation 4.25. Since $[B]$ matrix depends on coordinates in axisymmetric case, the integration can be performed numerically or by explicit multiplication and term by term integration.

4.3 ANSYS

Finite element analysis tool ANSYS [46] is employed in the analysis. This section summarizes the general features of the program.

ANSYS is a computer program for the finite element analysis and design. It is a general purpose program that can be used in any type of finite element analysis in virtually any industry such as automobile, aerospace, railway, machinery, electronics, sporting goods, power generation, power transmission and biomechanics. Also, the program can be used in many engineering disciplines such as structural, mechanical, electrical, electromagnetic, electronic, thermal, fluid and biomedical. The ANSYS program is used as an educational tool at universities. ANSYS software is available on many types of computers including PCs and workstations. Several operating systems are supported.

The procedure for a typical ANSYS analysis can be divided into three distinct steps [65]:

- build the model
- apply loads and obtain the solution
- review the results

Build the Model

Building the model is probably the most time-consuming portion of the analysis. In this step, the job name and analysis title are chosen and the element types, element real constants, material properties, and the model geometry are defined under the pre-processor part (PREP 7).

The ANSYS element library contains over 80 different element types. Each element type is identified by a unique number and a prefix that identifies the element category: BEAM4, SOLID96, PIPE16, etc. The following categories are available: BEAM, COMBINation, CONTACT, FLUID, HYPERelastic, INFINite, LINK, MASS, MATRIX, PIPE, PLANE, SHELL, SOLID, SOURCe, SURFace, USER, and VISCOelastic (or viscoplastic).

The element type determines, among other things, the degree-of-freedom set (which implies the discipline: structural, thermal, magnetic, electric, fluid, or coupled-field), the characteristic shape of the element (line, quadrilateral, brick, etc.), and whether the element lies in 2-D or 3-D space.

The size and number of elements are determined by the desired accuracy and available computer resources. An increase in the number of elements generally means more accurate results. However, the use of large number of elements involves large number of degrees of freedom and it may not be possible to store the resulting matrices in the available computer memory.

Material properties are required for most element types. Depending on the application, material properties may be linear, nonlinear and/or anisotropic.

The main objective of this step is to generate a finite element model: nodes and elements that adequately describe the model geometry. There are two methods to create the finite element model: solid modelling and direct generation. With solid modelling geometric boundaries of the model can be described and then the ANSYS program is instructed to automatically generate a mesh of nodes and elements. The size and shape of the elements can be controlled. With direct generation, the location of each node and the connectivity of each element are manually defined. Several convenience operations, such as copying patterns of existing nodes and elements, symmetry

reflection, etc., are available. For simple geometries solid modelling is generally easier to apply. The generated model, along with the material properties input are written to a database.

Apply Loads and Obtain the Solution

In this step, SOLUTION menu is used to define the analysis type and analysis options, to apply loads, specify load step options and initiate the finite element solution.

The analysis type is chosen based on the loading conditions and the response to be calculated. For example, if natural frequencies and mode shapes are to be calculated a modal analysis would be chosen. The following analysis types are available in the ANSYS program: static, transient, harmonic, modal, spectrum, buckling, and substructuring.

The word 'loads' as used in the ANSYS program includes boundary conditions as well as other externally and internally applied loads. Loads in the ANSYS program are divided into six categories:

- DOF constraints
- forces
- surface loads
- body loads
- inertia loads
- coupled-field loads

Most of these loads can be applied either on the solid model (keypoints, lines and areas) or the finite element model (nodes and elements).

Loads are applied to the model in steps. A load step is simply a configuration of loads for which a solution is to be obtained. In a structural analysis, for example, wind loads may be applied in one load step and gravity in a second load step. Load steps are also useful in dividing a transient load history curve into several segments.

Substeps are incremental steps taken within a load step. They are mainly used for accuracy and convergence purposes in transient and nonlinear analyses. Substeps are also known as time steps – steps taken over a period of time. Load steps have options that can be changed at each load step, such as the number of substeps, time at the end of a load step, and output controls.

After the SOLVE command, the ANSYS program reads the model and the loading information from the database and calculates the results. Results are written to the results file (*Jobname*.RST, *Jobname*.RTH or *Jobname*.RMG, where *Jobname* is the name chosen before building the model) and also to the database. The difference is that only one set of results can reside in the database at one time, whereas all sets of results (for all substeps) can be written to the results file. Any set of results can be read from the results file into the database at any time for further processing.

Review the Results

Once the solution has been obtained the ANSYS postprocessors can be used to review the results. Two postprocessors are available: POST 1 and POST 26.

POST 1, the general postprocessor, is used to review results at one substep (time step) over the entire model. Contour displays, deformed shapes and tabular listings can be obtained to aid review and interpret the results of the analysis. Other capabilities are available in POST 1, including error estimation, load case combinations, calculations among results data, and path operations.

POST 26, the time history postprocessor, is used to review results at specific points in the model over all time steps. Graphical plots of results versus time (or frequency) and tabular listings can be obtained. Other POST 26 capabilities include arithmetic calculations and complex algebra.

Chapter 5

The Coated Fuel Particle Finite Element Model

In this study, a finite element model of the coated fuel particle of high temperature reactors is prepared and structural and thermal analyses are performed with this model. This chapter summarizes the model used in the analyses.

5.1 Mechanical Model

The aim of the mechanical analysis is to determine the stress distribution inside the coated fuel particle layers for predicting the particle failure probability. Details of the mechanical model of a coated fuel particle is presented below.

The coated fuel particle is in the form of a sphere. With the exception of asymmetric behavior due to operating conditions or manufacturing defects, it preserves its spherical shape. Therefore, the coated fuel particle can be modelled in two dimensions with rotational symmetry. This approach reduces the computing time in the analysis. The particle is modelled as a quarter circle in the first quadrant with axisymmetry to form a half sphere, with symmetry boundary conditions to represent the other half. The load bearing layers of the coated fuel particle are IPyC, SiC and OPyC, and these three layers are modelled. In CRP-6 study presented in Appendix A, one- and two-layered particles are also modelled. Since ANSYS produces all results in cartesian coordinates, a new local coordinate system of spherical type is defined in order to read the results in spherical coordinates. Figure 5.1 presents the finite element model of a TRISO coated particle with three load bearing layers. This three-layered model is employed in kernel migration and reactivity initiated accident analyses.

The 2D, 8-node, structural solid element Plane 82 with axisymmetric element behavior is employed in the modelling. Plane 82 is defined by eight nodes having two degrees of freedom at each node: translations in the nodal x and y directions. The element may be used as a plane element or as an axisymmetric element that represents a torus around the y axis. The element has plasticity, creep, swelling, stress

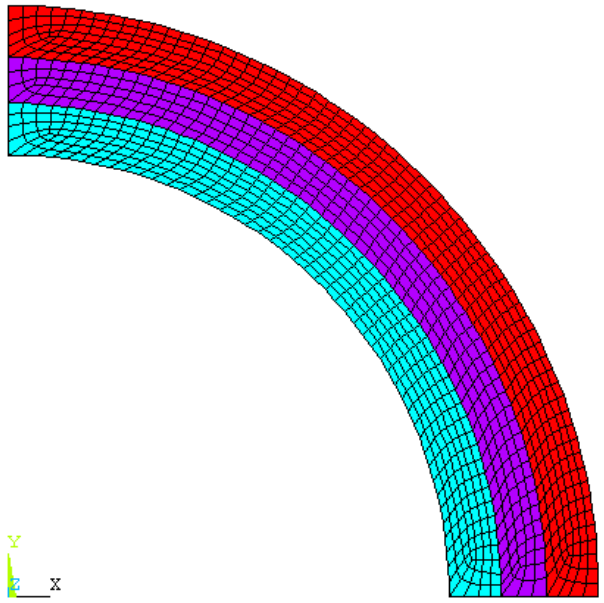

Figure 5.1: Finite element model of mechanical analysis

stiffening, large deflection and large strain capabilities. Plane 82 provides output of displacements, stress and strain components in nodal and element solutions. Figure 5.2 presents Plane 82 geometry [46].

Two sets of material properties are defined for the finite element input. The IPyC and OPyC layers have the same material properties, and the SiC is the second material. Material properties employed for CRP-6 study, kernel migration analysis and reactivity insertion accident are presented in the corresponding chapters. The SiC shows isotropic behavior for the conditions analyzed. However, pyrocarbon layers show anisotropic behavior and change of material property in radial and tangential directions is taken into account.

Material properties are composed of modulus of elasticity, density, Poisson's ratio, creep constants and thermal expansion coefficients. Since ANSYS has no built-in swelling model, the effect of swelling or shrinkage is modelled as thermal expansion and are represented by temperature-dependent thermal expansion coefficients with time being represented by the temperature.

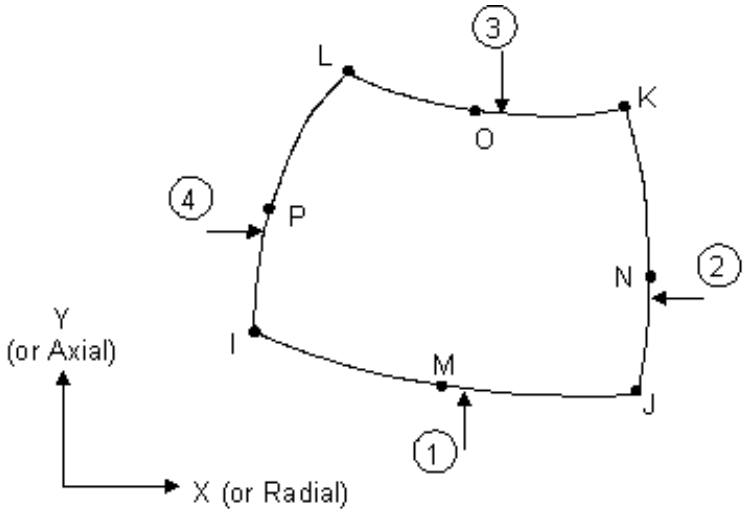

Figure 5.2: Plane 82 geometry [46]

The anisotropy of PyC layers manifests itself in shrinkage under neutron fluence. IPyC and OPyC layers behave differently in radial and tangential directions as a result of anisotropy. Radial and tangential swelling/shrinkage rates as a function of fast neutron fluence are presented in the equations in Appendix A. Equations change according to the initial BAF of the case and also depend on material properties and irradiation conditions. These equations give the strain rate as a function of fast neutron fluence. The resulting strain in each directions is calculated externally and imposed on the model as if it were due to thermal expansion. Thus, thermal expansion coefficient values in radial and tangential directions used in the calculations also represent swelling or shrinkage data.

Since the geometry is not complicated, free mesh is employed in the ANSYS meshtool. Sensitivity of the problem to the mesh size is also investigated. The optimum mesh size has been determined in order to gain computing time without affecting the results. The effect of mesh size variation on stress values is on the order of 1%.

Loads for the transient structural finite element model are:

- pressure history, with burnup, on the IPyC layer due to fission gases, calculated externally
- 0.1 MPa of ambient pressure

- thermal expansion for IPyC, SiC and OPyC layers
- creep for IPyC and OPyC layers
- irradiation-induced swelling/shrinkage on radial and tangential directions, represented by the coefficients of thermal expansion

The swelling/shrinkage rate of the coated fuel particle depends on the fluence, so fluence is employed as the time variable. Results can be presented against either burnup or the actual time, since both are linearly related to fluence.

Structural analyses have been performed as transient cases, for the pressure load changes with time. Stress distributions inside the coated fuel particle are obtained from the analyses. These values are employed in calculation of the particle failure probability.

5.2 Thermal Model

Thermal analysis aims to determine the temperature distribution inside the coated fuel particle. Results of thermal analysis also provide input for mechanical analysis.

All five layers of the coated fuel particle are modelled, including the kernel, buffer and the TRISO coating layers. The coated fuel particle is modelled axisymmetrically in two dimensions. The spherical local coordinate system defined under mechanical analysis is also employed. Figure 5.3 presents the finite element model for thermal analysis of a TRISO coated particle with five layers.

The 2D, 6-node, triangular thermal solid element Plane 35 is employed in the modelling. The element has one degree of freedom, temperature, at each node. The element may be used as a plane element or as an axisymmetric element. The nodal solution of the element produces temperature distributions. Figure 5.4 presents Plane 35 geometry [46].

Four sets of material properties are defined for the finite element input. The IPyC and OPyC layers have the same material properties. Material properties em-

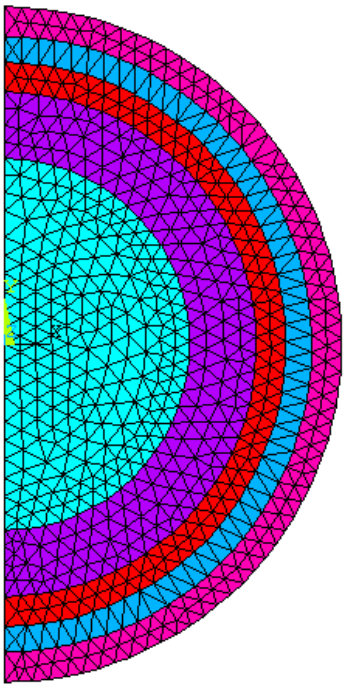

Figure 5.3: Finite element model of thermal analysis

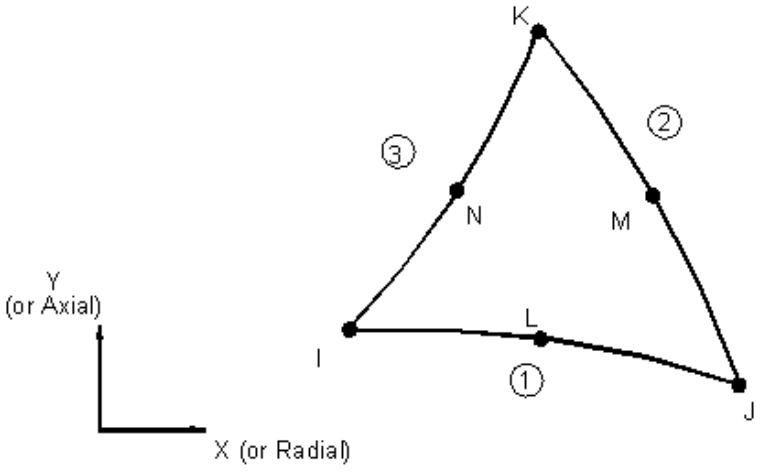

Figure 5.4: Plane 35 geometry [46]

ployed for CRP-6 study, kernel migration analysis and reactivity insertion accident are presented in the corresponding chapters. All material properties are isotropic in thermal analysis. Thermal conductivity, density and specific heat capacity are the input values for material properties of the transient thermal analysis.

Since the geometry is not complicated, free mesh is employed in ANSYS meshtool. Sensitivity of the problem to the mesh size is also investigated.

Loads for the thermal analysis finite element model are:

- constant heat generation from kernel
- constant surface temperature

Thermal analysis has been performed for kernel migration and reactivity insertion accident cases. CRP-6 study cases are at constant temperature. Steady state calculations are performed for kernel migration analysis. Thermal analysis of reactivity insertion accident is performed as a transient.

Chapter 6

Kernel Migration Analysis

Kernel migration is simply defined as the movement of the kernel towards TRISO coated layers. The driving force for the kernel migration is extreme operating conditions and asymmetrical kernel production during manufacturing [42]. This so-called "amoeba effect" strongly depends on power density, temperature, and temperature gradient across the fuel. Therefore, prismatic fuel elements have a greater susceptibility to kernel migration compared to pebble bed reactor fuel elements due to the presence of a more severe temperature gradient.

Kernel migration is associated with carbon transport inside the particle in the presence of a temperature gradient. In the fuel kernel chemical equilibrium is established among C, UO_2, and CO. When there is a thermal gradient across the particle, the equilibrium is different on each side of the particle. This thermal gradient may be as high as 15,000 °C/m, which is about four to five times the normal temperature gradient. The different equilibrium conditions lead to mass transport of carbon down the temperature gradient. This movement of carbon appears in photomicrograph of fuel as a movement of the kernel up the temperature gradient and hence the name kernel migration as shown in Figure 6.1. The net effect of this carbon transport is to gradually push the kernel in the direction of increasing temperature, across the buffer so that the kernel moves toward the SiC layer and may eventually damage it, which is undesirable. This phenomenon is strongly dependent on the temperature and temperature gradient in the fuel, with secondary dependence on burnup [41].

The present study includes thermal and mechanical analyses of a TRISO coated particle with a migrated kernel using finite element techniques. Details on analysis and kernel migration phenomena are presented in the following sections.

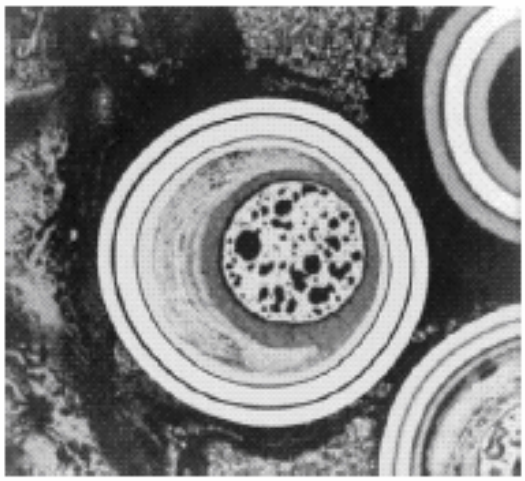

Figure 6.1: Photomicrograph of kernel migration [4]

6.1 CO Formation and Kernel Migration

In oxide based fuel kernels, free oxgen is formed as a result of the consumption of fissionable nuclides. This free oxygen first oxidizes the rare earth elements, which have the greatest affinity for oxygen. The remaining oxygen oxidizes the other elements such as Sr, Eu, Zr, and Ba in UO_2 fuels [52]. If there is still free oxygen left remaining in the system, it may diffuse out of the kernel and react with the carbon in the coating layers under appropriate conditions, resulting in CO and CO_2 production. Under HTR operating conditions, CO is formed; the CO_2 contribution is usually below a few percent [53]. In the case of UO_2, the lowest charge state of uranium is +4. It is the common charge state of uranium in the fresh fuel and it is more difficult to oxidize uranium to higher charge states than oxidizing other constituents of the fuel. On the other hand, hypostoichiometric mixed oxide fuel kernels obtained by mixing +3 and +4 valanced Pu will not be susceptible to CO/CO_2 formation until very high burnup levels since oxygen liberated with fission reactions will be preferentially oxidizing plutonium to its +4 charge state. Figure 6.2 presents an illustration of the amoeba effect. There are other remedies to CO production such as placing a getter in or near the kernel to bind the excess oxygen and making a two-phase kernel such as UCO, i.e., a mixture of UO_2 and UC_2, allowing the released oxygen to react with the carbide phase without

diffusing through the kernel.

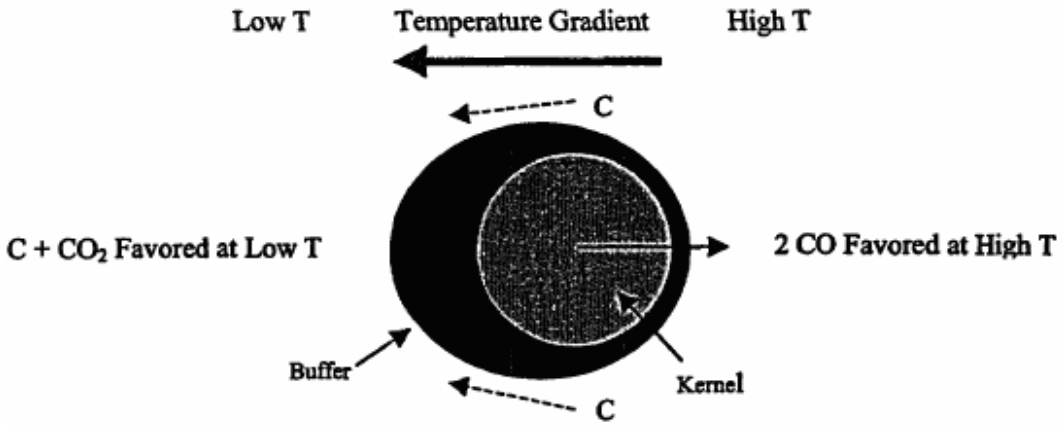

Figure 6.2: Illustration of the amoeba effect [4]

6.2 Previous Studies

Mass spectrometric measurements of CO contained in irradiated UO_2 fuel particles are evaluated and summarized in Proksch et al.'s study [53]. The study presents the oxygen release per fission with the empirical formula

$$\log_{10}((O/f)/t^2) \quad = \quad -0.21 - \frac{8500}{T} \tag{6.1}$$

where O/f is the number of oxygen atoms released per fission, t is the irradiation time in days and T is the time averaged particle surface temperature during irradiation in K. Details on CO calculations are presented in Appendix B.

Kernel migration has been studied experimentally by Lindemer et al. [54] for different types of HTR fuels. Their analysis includes coated fuel particles of BISO and TRISO type with UO_2, ThO_2, ThC_2 and UC_2 kernels. The result obtained by a least squares fit to the laboratory and reactor data is the following equation:

$$\log_{10}(KMC) \quad = \quad \alpha - \alpha_1 T^{-1} \tag{6.2}$$

where α's are the coefficients of equation, T is temperature in Kelvins and KMC is the kernel migration constant in m^2K/s, which is the proportionality constant between the kernel migration rate and $(dT/dr)/T^2$. α values are presented only for in-reactor UO_2 fuel and values include the fit of 69 coated fuel particle irradiations including BISO and TRISO coated fuel particles with $^{233}UO_2$ and $^{235}UO_2$ in the range of temperature gradient 20,000 to 57,500 °C/m.

This study covers a wide spectrum of data in design and operating conditions. Current design coated fuel particles are of TRISO type with $^{235}UO_2$ fuel. Also, current design HTRs have an average temperature gradient of 15,000 °C/m, which is below the range of Lindemer et al.'s data.

The study of Choi et al. offers an analytical model for the amoeba effect in coated fuel particles with UO_2 kernels [55]. In Choi's model, amoeba effect is analyzed in terms of an interactive transport phenomenon between the solid state diffusion of oxygen ions in a UO_2 kernel and flow of CO gas molecules through the pyrocarbon buffer layer. The model assumes a cylindrical shaped particle for mathematical simplicity. The results of the study show that not only a concentration gradient in oxygen ions but also a temperature gradient with a negative heat of transport for oxygen ions can cause the amoeba effect in UO_2 fueled coated fuel particles.

Study of Sawa et al. [56] presents the results of experiments on the amoeba effect that were carried out by capsule irradiation, where a temperature gradient of about 15,000 °C/m was imposed on the coated fuel particles embedded in graphite disks. Kernel migration distance in the coated fuel particles was measured by X-ray radiography during postirradiation examination. Experimental data on kernel migration distances from irradiation tests of the High Temperature Test Reactor (HTTR) is presented in Figure 6.3.

One of the results of the study is the fit of experimental data to the following correlation:

$$KMR = 2 \times 10^{-6} \exp\left(-\frac{14800}{T}\right) \frac{1}{T^2} \frac{dT}{dr} \tag{6.3}$$

where r is the radial distance in meters, T is the temperature in K and KMR is the kernel migration rate in m/s. This correlation is applicable to TRISO type coated fuel

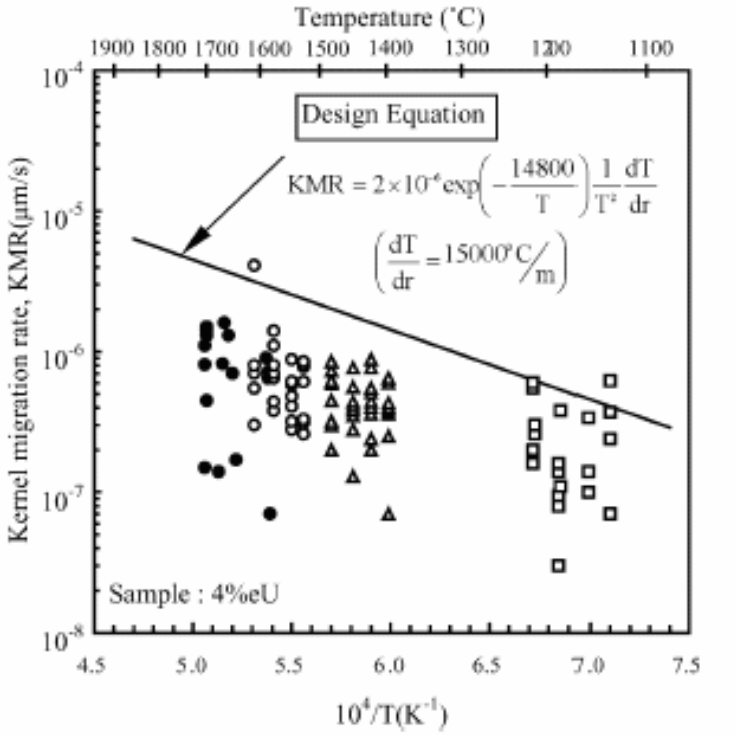

Figure 6.3: Experimental data on kernel migration distances from irradiation tests [56]

particles having UO_2 kernels within the irradiation temperature range of 1300-2100 K and valid for the temperature gradient of 15,000 °C/m.

Equation 6.3 is employed in the present study to evaluate the position of the migrated kernel as a function of temperature. Therefore, the fuel and its operational parameters utilized in this study represent a typical coated fuel particle utilized in the HTTR.

6.3 Kernel Migration Model

The present study includes thermal and mechanical analyses of a TRISO coated particle with a migrated kernel using finite element techniques. These analyses depend on calculation of kernel migration distance.

There exists two main approaches for determining the kernel migration distance. First approach is the application of Equation 6.3, which depends on experimental data and considers the presence of CO inherently. This approach assumes that the

volume left behind the migrated kernel is filled with fission product gases and CO. The second approach is calculation of the number of CO molecules with burnup by Equation 6.1 and assuming that mass reduction due to reaction of oxygen with carbon layers provide the necessary empty volume for gases to move and for the kernel to migrate. In order to compare the two approaches, number of CO molecules and kernel migration distance are calculated for a sample case. The sample case involves a particle operating at 1723 K and producing 0.3 W power up to a burnup of 20% FIMA. The temperature is within the operating limits; however, 20% FIMA is a relatively high burnup value. Change of the number of CO molecules with burnup for the two approaches is presented in Figure 6.4 and the kernel migration distances calculated from carbon and oxygen reaction are presented in Figure 6.5.

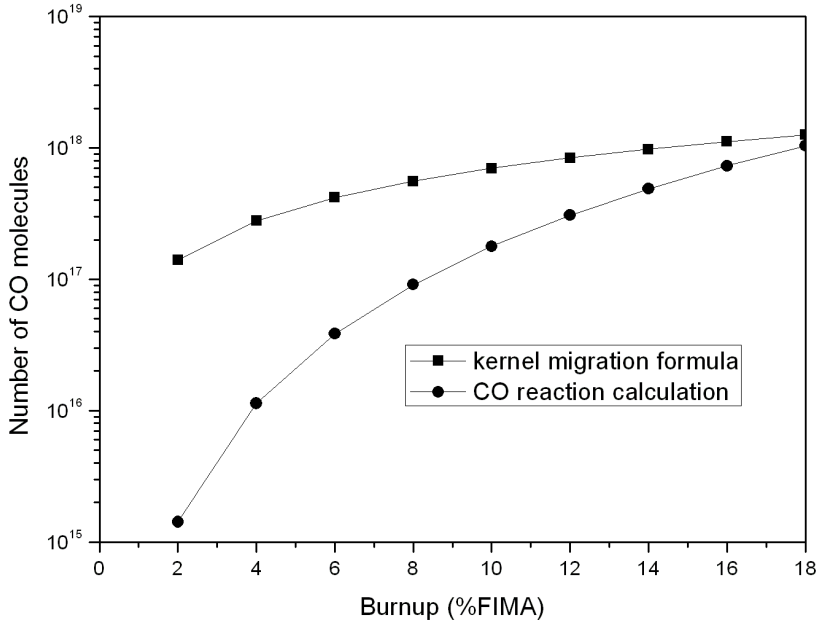

Figure 6.4: Change of CO molecules with burnup

Kernel migration equation 6.3 gives higher results in comparison. However, the difference between the two approaches decrease as burnup proceeds. CO reaction calculation does not consider the secondary effects that may play an important role in

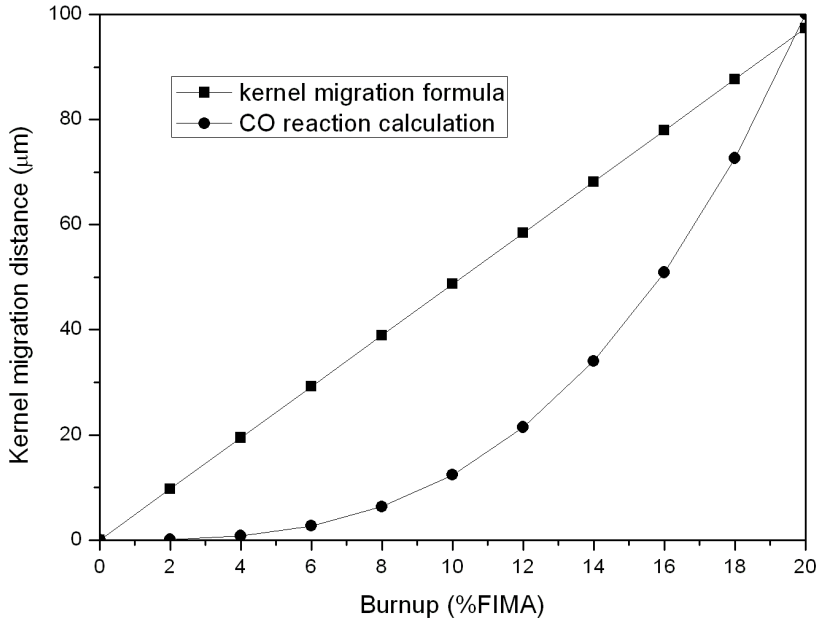

Figure 6.5: Change of kernel migration distance with burnup

predicing the kernel migration distance. One of these effects is the compression of the buffer layer by the migrated kernel. Since the buffer is a porous medium, compression by the kernel may decrease the porosity of the buffer layer in the direction of kernel migration. Equation 6.3 is employed in this study for predicting the kernel migration distance.

6.4 Analysis Steps

The present study includes thermal and mechanical analyses of a TRISO coated particle with a migrated kernel using finite element techniques. Analysis is composed of structural, thermal and probabilistic parts. Table 6.1 presents the properties of a TRISO coated fuel particle.

The CFP is assumed to produce about 0.3 W power in a typical kernel. The outer surface temperatures of the CFP are chosen to be 1473 K and 1723 K. Both

Table 6.1: Properties of TRISO CFP

Fuel material	UO_2
Oxygen to uranium ratio	2
Kernel diameter (μm)	600
Coating layer materials	PyC / PyC / SiC / PyC
Coating layer thicknesses (μm)	60 / 30 / 25 / 45

surface temperatures are within the normal operating temperatures of HTTR, the higher one being near the upper limit. Irradiation condition is 8% FIMA, which is higher than the target burnup [57]. A temperature gradient of 15,000 °C/m is assumed to be present on the particle in order to simulate kernel migration conditions. This temperature gradient has been applied to measure the kernel migration distances in HTTR fuel.

6.5 Analysis Methodology

Structural analysis is performed to determine the stress distributions in the load bearing layers IPyC, SiC and OPyC with increasing burnup. Thermal analysis determines the temperature distributions inside the whole coated fuel particle. Maximum kernel temperature at each time step is used to calculate the kernel migration distance. Probabilistic analysis employs the stress distribution from structural analysis in order to determine particle failure probability.

Kernel migration calculations start with the calculation of the temperature distribution inside a nominal coated fuel particle. The maximum kernel temperature value is employed in the calculation of the kernel migration distance for the next time step. It is chosen so that the most conservative results will be yielding from the nuclear safety point of view. The kernel is assumed to migrate along the z axis and a displacement equal to the kernel migration distance calculated from Equation 6.3 is applied on the kernel. The kernel is assumed to preserve its spherical shape during migration. A new temperature distribution is obtained and a new migration distance is calculated for the next time step. The time steps are chosen small enough so that further reduction will not change the results. All of the free oxygen formed as a result of fission is assumed to bind the carbon of the buffer layer to form CO. The maximum

Table 6.2: Thermal properties for layers of coated fuel particle and CO gas

	UO_2	Buffer	IPyC	SiC	OPyC	CO
ρ (kg/m^3)	10,800	900	1,900	3,200	1,900	0.421
k (W/m.K)	5	2	7	25	7	55×10^{-3}
c_p (J/kg.K)	247	1,800	1,300	1,800	1,300	1,140

temperature value is also employed for the calculation of the pressure due to fission gases and CO inside the IPyC layer. The number of fission gas atoms diffused out of the kernel and the number of CO molecules formed inside the CFP are calculated at each time step. Fission product gases Xe, Kr and CO molecules are assumed to fill the free volume of the buffer and the gap left behind the kernel after migration. Moreover, kernel swelling is also taken into account in the calculation of the free volume available for the gas molecules. Ideal gas equation of state is employed for the calculation of pressure inside the IPyC layer. Flow chart of the kernel migration analysis methodology is presented in Figure 6.6.

In Figure 6.6 *KMD* is the kernel migration distance, T_n is the temperature at time step *n*, *P* is the pressure inside the IPyC layer and σ is the stress value to be calculated.

6.5.1 Thermal Analysis

Thermal analysis involves calculation of the nodal temperatures at specified time steps up to the desired burnup. Thermal analysis model includes all five layers: UO_2 kernel, buffer, IPyC, SiC and OPyC.

Finite element model is initially composed of four types of materials since IPyC and OPyC are assumed to have identical material properties [16]. Table 6.2 presents the thermal properties of the five layers of the coated fuel particle. The properties do not change significantly within the range of temperature being analyzed [16, 59].

In Table 6.2 ρ is the density, c_p is the specific heat capacity and k is the thermal conductivity of the material. Kernel migration is modelled as the change of z coordinate of the UO_2 kernel as it is assumed to migrate in that direction. Change in

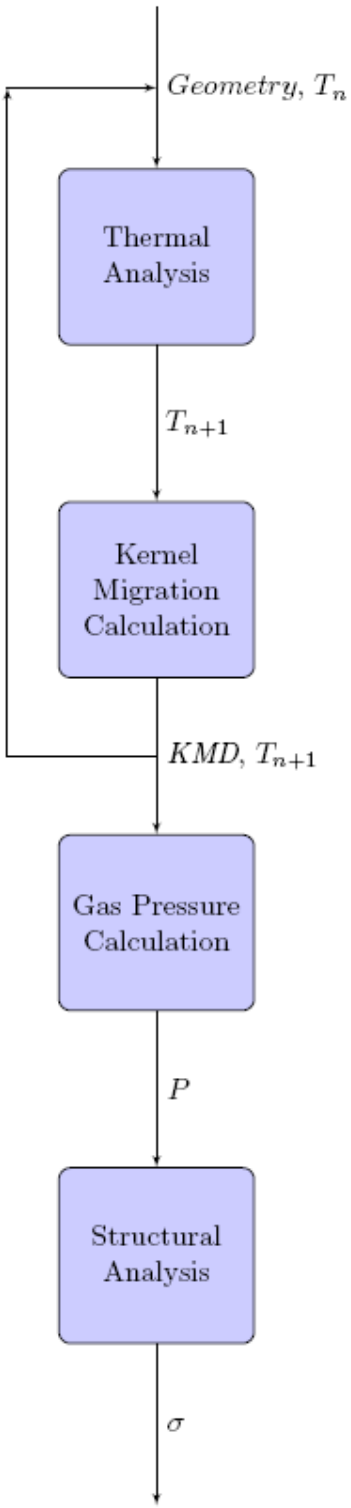

Figure 6.6: Flowchart of the kernel migration analysis methodology

z coordinate is calculated from Equation 6.3 with the input of temperature value from the previous time step. The volume left behind the migrated kernel is assumed to be filled with CO gas, the amount of which is calculated from Equation 6.1 at each time step, and the fission product gases released from the kernel, the amount of which is calculated as explained in Appendix B. Figure 6.7 presents the finite element model of thermal analysis with a migrated kernel.

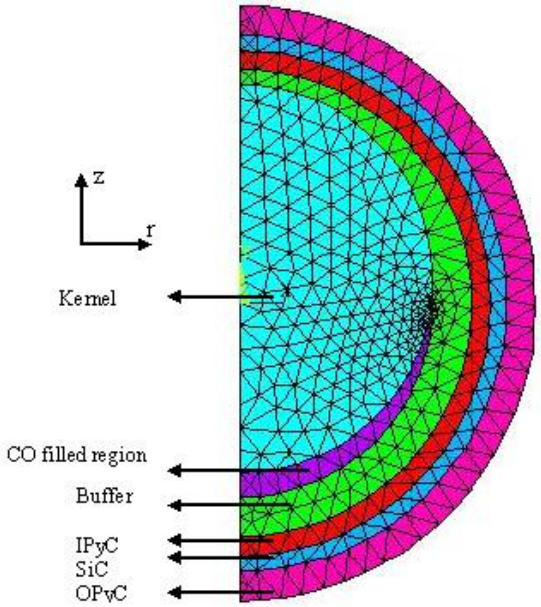

Figure 6.7: Finite element model of thermal analysis

The maximum kernel temperature value is employed in calculating the kernel migration distance for each time step. Therefore, it is expected to yield a conservatively large kernel migration distance. Presence of a gas-filled region causes a greater temperature gradient within the particle in the migration direction compared to that in the transverse direction.

Kernel migration distances and temperature distributions are calculated for a coated fuel particle with 1473 K and 1723 K surface temperatures. The limiting burnup values for the two cases are 18 and 8% FIMA, respectively. Figure 6.8 presents the kernel migration distances for both cases.

The kernel migration distance values for the low temperature case is 30 μm

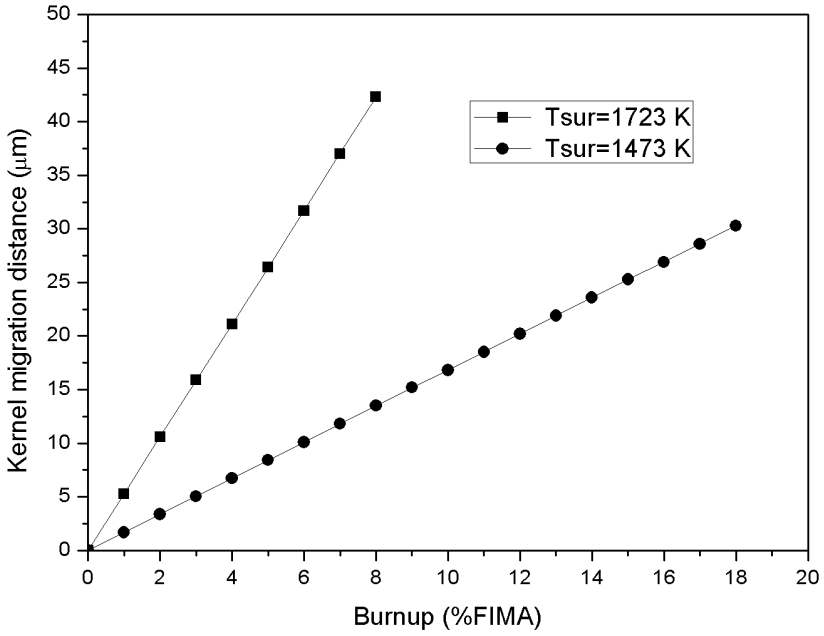

Figure 6.8: Kernel migration distances for two cases

(with longer burnup) and for the high temperature case it is 43 μm (with shorter burnup). In reactor conditions the limiting burnup is 5 to 10% FIMA; therefore, the analysis covers the normal operating conditions of the particle. In both cases, the kernel migration is limited within the buffer layer. Temperature distribution inside the coated fuel particle with the lower temperature at the end of irradiation period is presented in Figure 6.9.

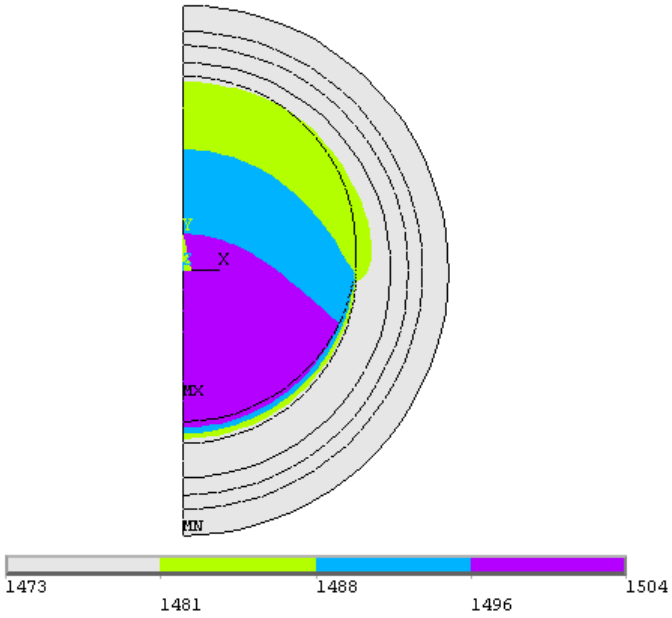

Figure 6.9: Temperature distribution inside the the coated fuel particle

The kernel is assumed to migrate along the z axis and an asymmetry in the temperature distribution along this axial direction is observed as a result of the loss of concentricity. Due to relatively low heat conduction of the CO gas, the heat transfer is poor on the opposite direction of kernel migration. This results in increased temperatures near the gap. Figure 6.10 shows the change in this asymmetric temperature distribution along the axial direction z at several burnup steps for a particle with 1473 K surface temperature. Figure 6.11 presents the same distributions for a particle with 1723 K surface temperature. For both particles, the maximum kernel temperature is about 15-20 K greater than that for the unmigrated particle. For the particle with 1473 K on the surface, the maximum temperature reaches 1503 K. For the particle with

1723 K surface temperature, the maximum temperature is 1755 K. The temperature distributions along the direction perpendicular to the migration for the two cases are given in Figures 6.12 and 6.13. A significant change in temperature distribution is also observed for the transverse radial direction as the kernel migrates. However, the slope is not as steep as is in the direction of kernel migration, for the CO layer is very small in the direction of heat transfer.

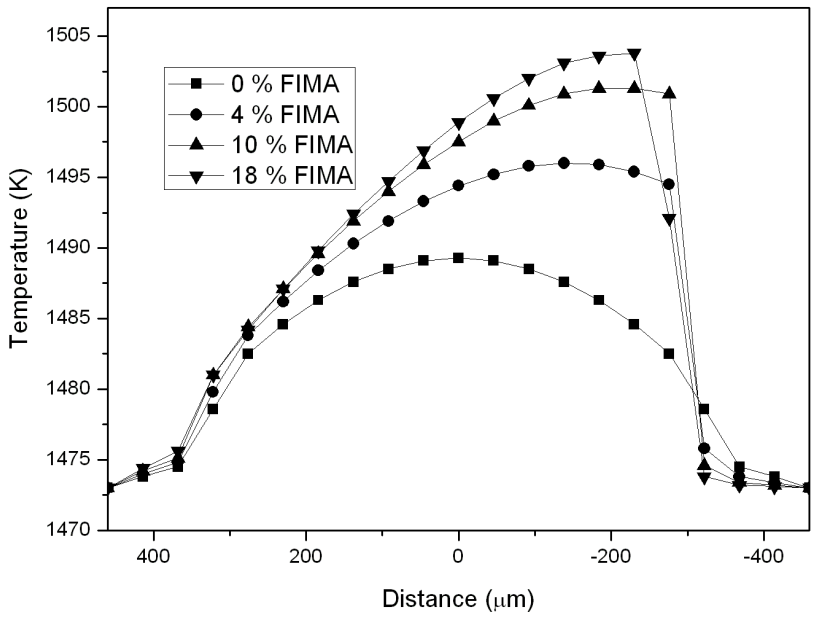

Figure 6.10: Temperature distribution along the z direction for 1473 K surface temperature

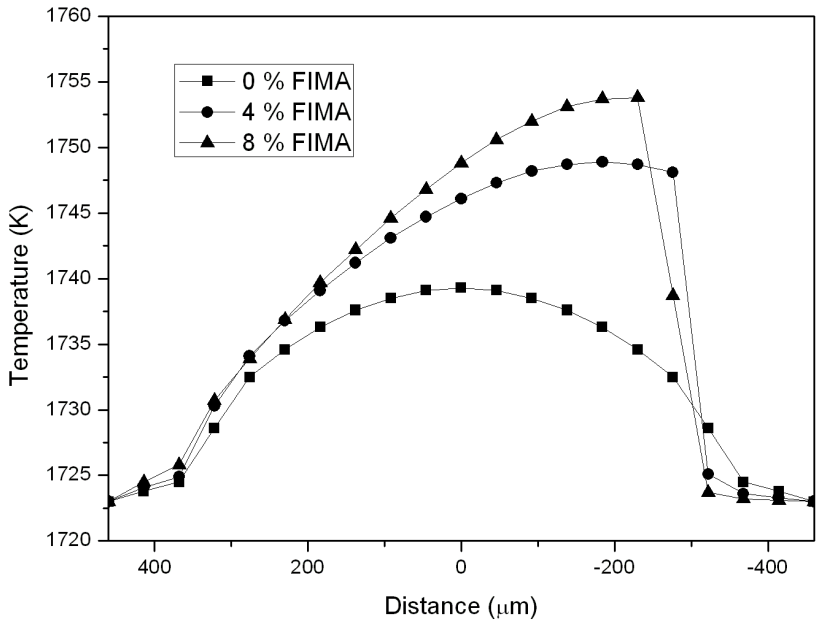

Figure 6.11: Temperature distribution along the z direction for 1723 K surface temperature

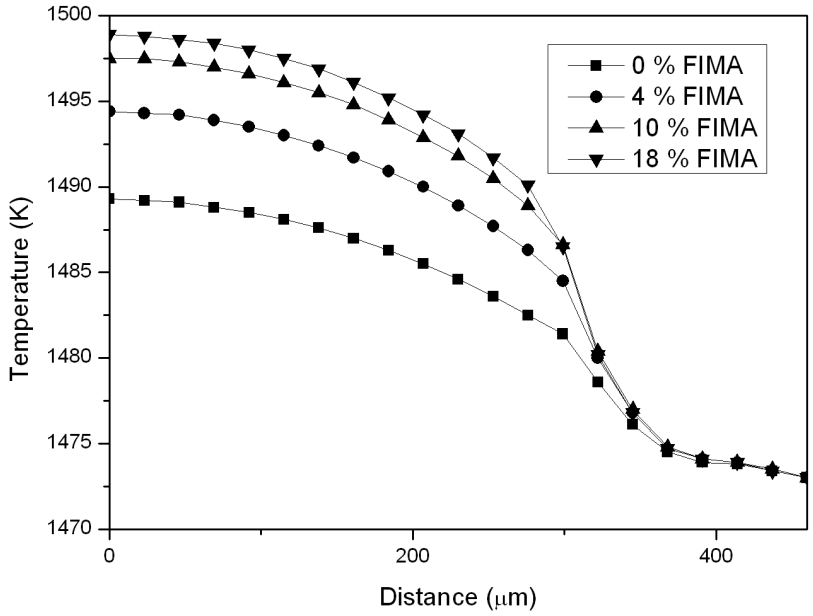

Figure 6.12: Temperature distribution along the r direction for 1473 K surface temperature

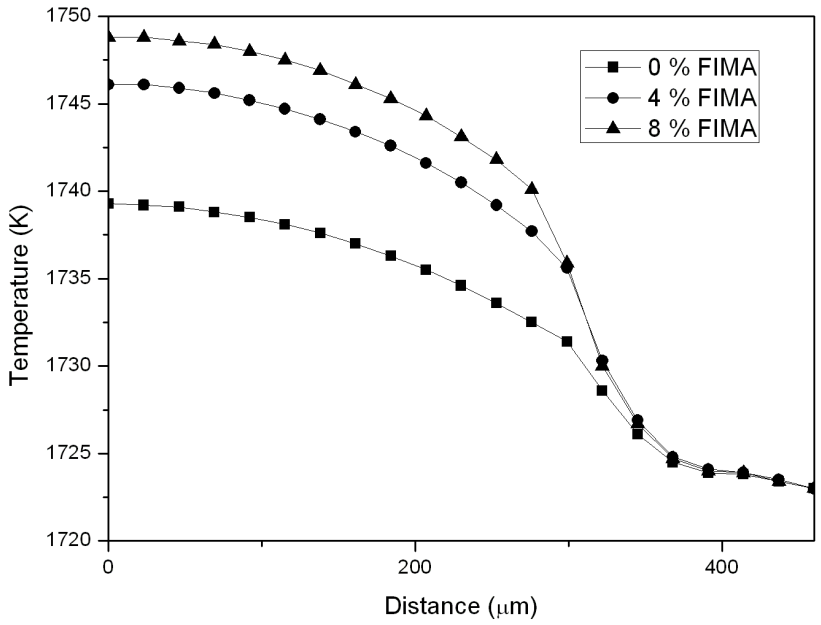

Figure 6.13: Temperature distribution along the r direction for 1723 K surface temperature

Table 6.3: Material properties for pyrocarbon and SiC layers

PyC modulus of elasticity (MPa)	3.96×10^{4}
PyC Poisson's ratio	0.33
PyC coefficient of thermal expansion (K^{-1})	5.50×10^{-6}
PyC creep coefficient (MPa-10^{25}/m^2)$^{-1}$ E>0.18 MeV	4.93×10^{-4}
SiC modulus of elasticity (MPa)	3.70×10^{5}
SiC Poisson's ratio	0.13
SiC coefficient of thermal expansion (K^{-1})	4.90×10^{-6}

6.5.2 Structural Analysis

Stress distributions for the load bearing layers are obtained at each time step using the internal gas pressure calculated at each time step as the boundary condition on the inner surface of the IPyC layer. The calculated maximum tangential stress value is then employed to calculate the failure probability of the coated fuel particle at each time step. The structural model performs transient analysis taking into account the results of thermal analysis. The model is composed of three load bearing layers: IPyC, SiC and OPyC. Material properties for the SiC and pyrocarbon layers employed in the structural analysis is presented in Table 6.3.

Details on fission gases and CO calculations are presented in Appendix B. Details on the creep model employed in finite element analysis is presented in Chapter 5.

Structural analysis starts with the calculation of gas pressure inside the IPyC layer. Pressure inside the IPyC layer for the case with 1473 K is presented in Figure 6.14. Figure 6.15 presents the gas pressure for 1723 K case. The pressure calculation considers the presence of the volume left by the migrated kernel.

The CO contribution to the total internal pressure is dominant at the high temperature case due to the greater oxygen release promoting CO formation with increasing fuel burnup. However, fission product gases are the main contributors up to a burnup level of about 16% FIMA due to a rather limited oxygen release for the low temperature case. The temperature distribution and pressure inside the IPyC is employed in determination of the stress distribution within layers. Gas pressure as a function of burnup is employed as the pressure boundary condition in the finite element

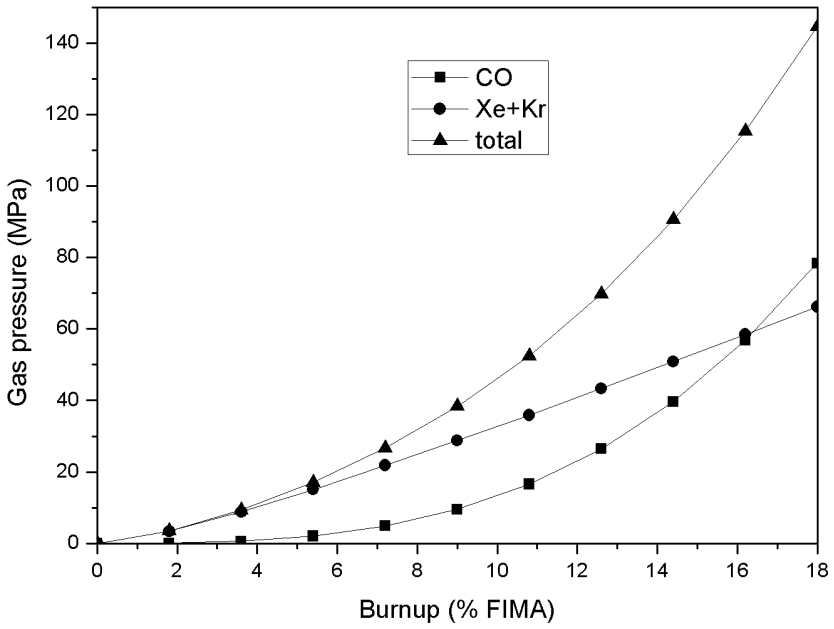

Figure 6.14: Internal gas pressure with burnup for the case with 1473 K surface temperature

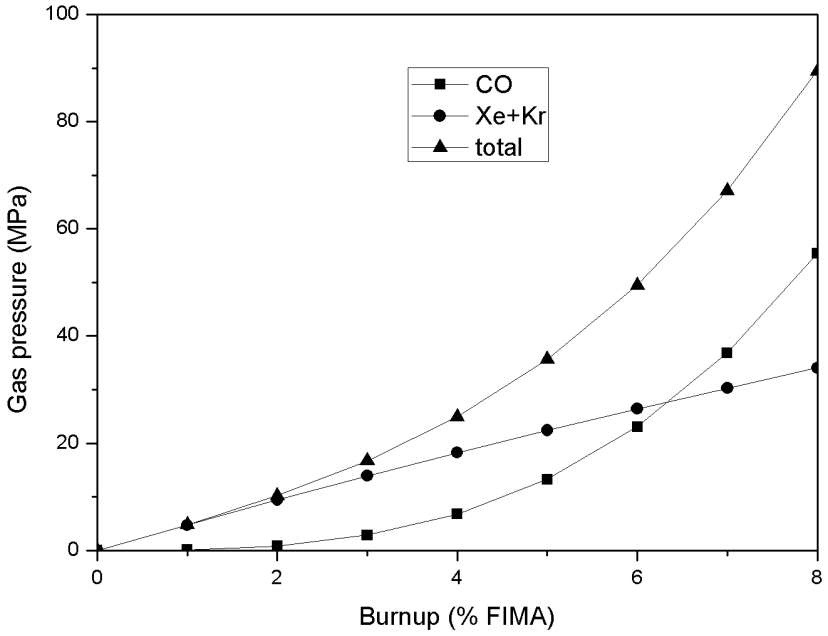

Figure 6.15: Internal gas pressure with burnup for the case with 1723 K surface temperature

analysis.

Figure 6.16 shows the variation of the tangential stress as a function of burnup in three load bearing layers for a particle with surface temperature of 1473 K. The IPyC and OPyC layers shrink at the initial stages of the irradiation, keeping the SiC layer under compression. Also, chemical bonding between the layers is an important force keeping the SiC under compression at the initial stages of irradiation. This condition persists until about 3.5% FIMA burnup. Due to the relaxation in pyrolitic carbon layers in the following period, tangential stress on the SiC becomes tensile and increases continously with increasing internal pressure. The mean failure stress is reached at about a burnup of 17% FIMA. Figure 6.17 shows the same variation for the particle with surface temperature of 1723 K. The initial compression state of the SiC is preserved until the burnup of 2.4% FIMA, and the mean failure stress is reached at about a burnup of 8% FIMA.

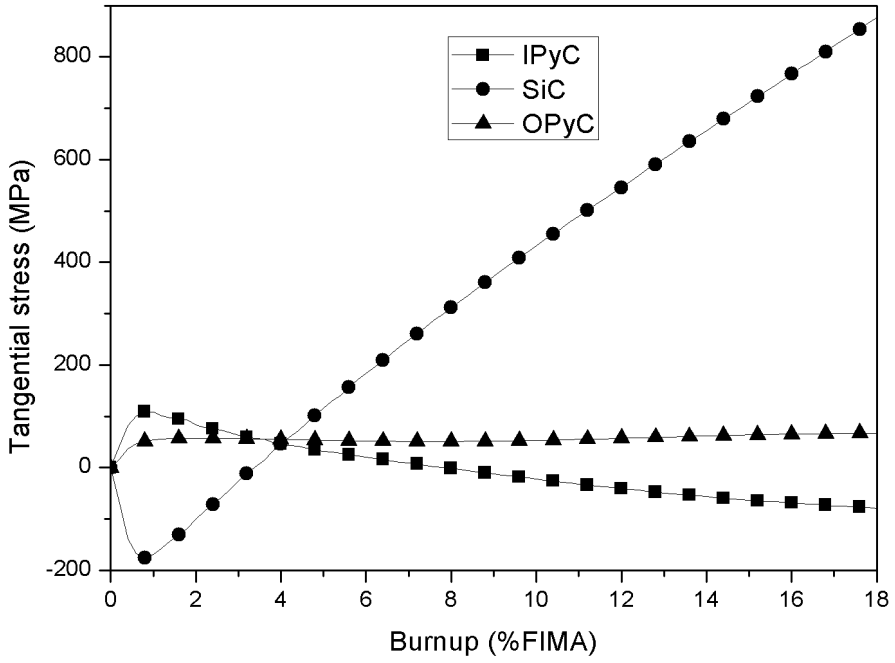

Figure 6.16: Maximum tangential stress in the CFP with surface temperature of 1473K

Determination of the tangential stress distribution is important for the SiC layer since the prefered condition for the pyrocarbon layers is keeping the SiC under

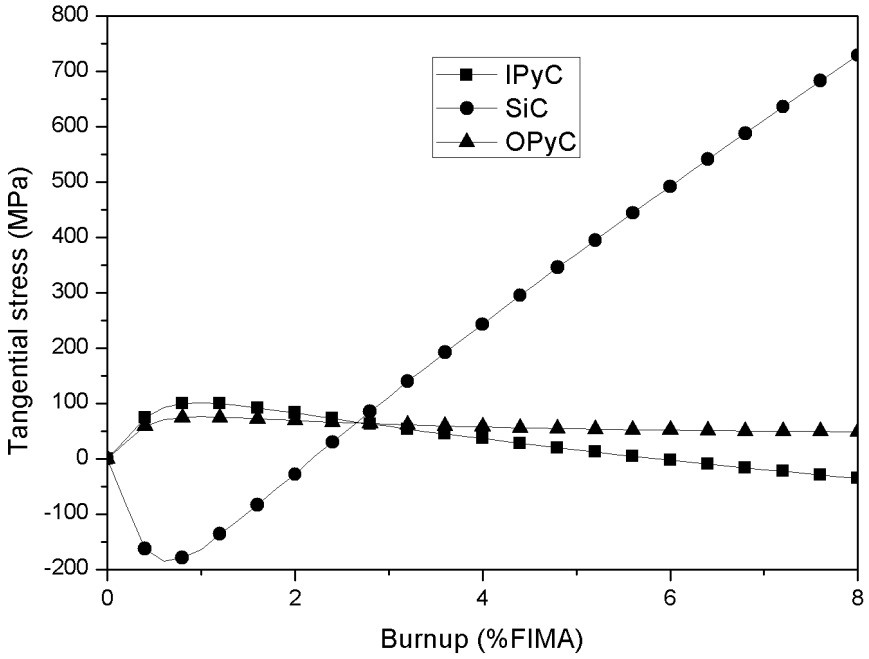

Figure 6.17: Maximum tangential stress in the CFP with surface temperature of 1723K

compression at all times during irradiation. Tension in the SiC layer may lead to failure and threaten the coated fuel particle integrity. Increase in tangential stress also increase crack tip stress values if a crack is present inside the SiC.

For analyzing the integrity of the SiC layer, a conservative approach that neglects the load bearing capacity of the IPyC layer is modelled. For that purpose, the effect of kernel migration is considered in coated fuel particles with a defective IPyC layer. Analysis involves the evaluation of maximum stress values in the SiC layer and the corresponding failure probabilities for a TRISO CFP with a failed IPyC layer. This case may be viewed as a scenario of common mode of failures. The IPyC layer fails at the initial stages of operation due to increased tangential stress combined with a manufacturing defect. The finite element model, shown in Figure 6.18(b) is constructed assuming a fully developed circumferential crack across the IPyC layer. The IPyC layer has no load bearing capability due to the crack. The finite element model includes all layers and the internal pressure is applied on the inner surface of the failed IPyC as a boundary condition. Calculations are carried out with the two

surface temperatures as defined earlier. The maximum tangential stress values as a function of burnup inside the SiC layer are presented in Figure 6.19 as the "failed IPyC" case. The absence of IPyC support on the SiC results in the exertion of higher tensile stresses and the stress reversal takes place at a lower burnup compared to that for the intact particle.

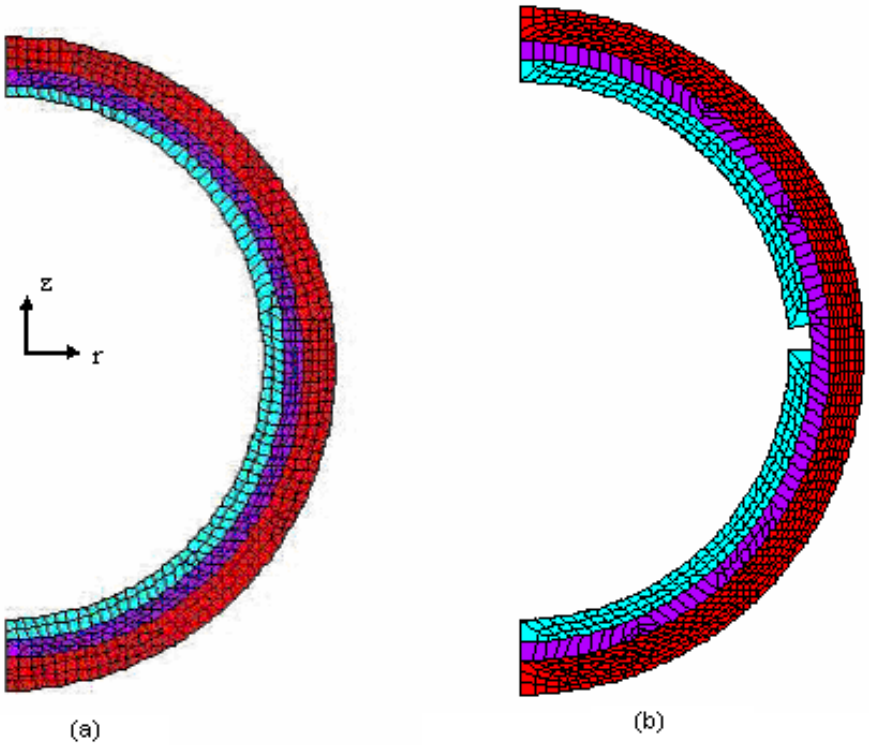

Figure 6.18: Finite element model of the CFP with (a) thin and (b) failed IPyC

Another analysis involves the prediction of stress distribution inside the SiC layer for the case of defective IPyC containing a thin section. The kernel migration is still confined within the buffer layer. Otherwise, the burnup necessary for the penetration of the kernel up to the buffer-IPyC boundary is so high that pressure vessel failure is expected in advance. Pressure build-up due to CO formation as well as fission product release is significant at high burnups. Figure 6.18(a) shows the finite element model of the coating layers with a thin IPyC layer section of 15 μm, half of the nominal thickness. The maximum tangential stress values as a function of burnup

inside the SiC layer are presented in Figure 6.19 as the “thin IPyC” case.

Faulty particles have higher tangential stress and the stress reversal to tension is observed at lower burnups. This results in the observation of higher failure probabilities especially at low burnups in such cases. The difference, however, is not so pronounced at high burnups as presented in Figure 6.20.

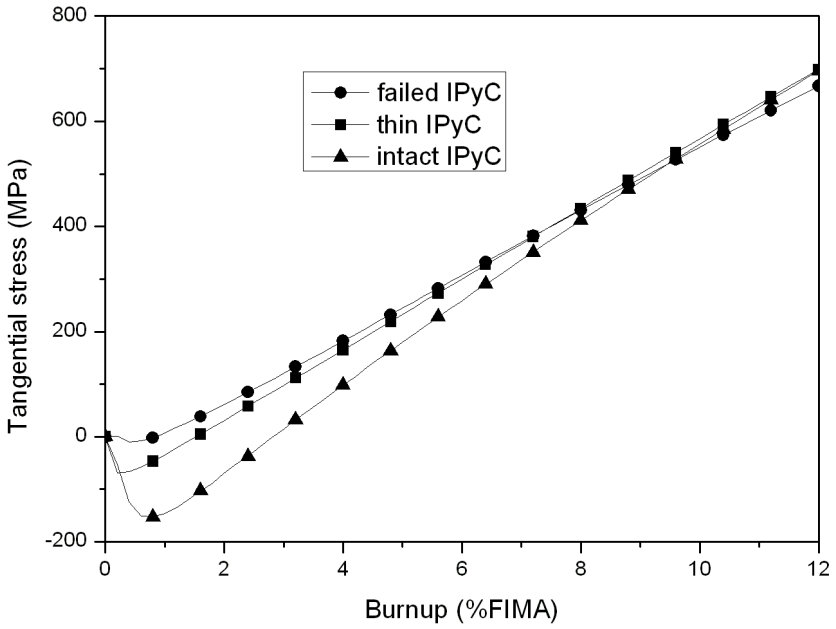

Figure 6.19: Tangential stress inside the SiC layer with failed, thin and intact IPyC layers

The cumulative failure probability for each coating layer is expressed by a Weibull distribution. Details on the Weibull distribution are presented in Appendix C. Median strength, σ_0, values for the pyrocarbon and SiC layers are 200 MPa and 873 MPa, respectively. Weibull moduli, m, for those layers are 5.0 and 8.02, respectively [25].

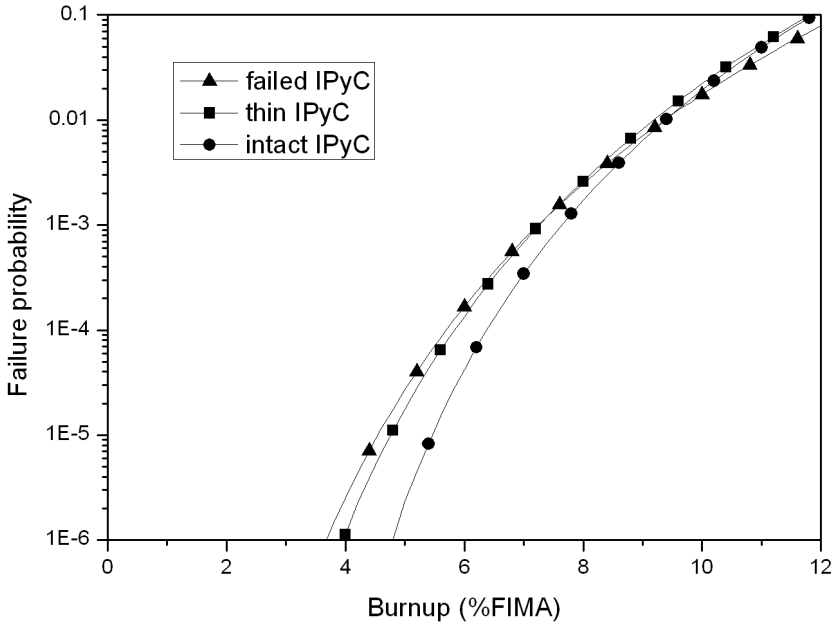

Figure 6.20: Failure probability of the SiC with failed, thin and intact IPyC layers

6.6 Conclusions

Kernel migration is considered a possible failure mode for coated fuel particles as presented in Chapter 2. Thermal and mechanical responses of a typical coated fuel particle are evaluated in this study for a number of cases representing different operational conditions and physical status of the particle. Also current coated fuel particle analysis tools do not model the kernel migration process satisfactorily, as described in Chapter 2. Results of this study can be summarized as follows:

- Operating temperature is the key parameter in fuel particle failure. There is no failure expected for the particle with a surface temperature of 1473 K even with kernel migration. This temperature is within the operating temperature limits of the HTTR. However, failure probabilities become appreciable when the surface temperature is 1723 K. This temperature is a typical upper limit for HTTR steady state operation. The extent of kernel migration is significantly affected by the temperature.

- The effect of kernel migration itself is not so critical on fuel failure. This is justified when temperature and stress values are compared for the same case with and without kernel migration. Pressure vessel failure is the primary mode of failure in high temperature and high burnup conditions.

- CO formation is a critical issue at the high temperature case. As temperature increases contribution of CO to the total gas pressure increases. Total gas pressure is the dominant term increasing the tangential stress values in the coated fuel particle, especially as burnup proceeds. The magnitude of the maximum stress experienced by the particle also indicates the importance of CO.

- The integrity of the IPyC layer is also critical in determining the failure probability of the primary pressure boundary, the SiC layer. IPyC and OPyC layers keep the SiC under compression for avoiding the failure of that layer. Early failure of the IPyC leads to higher tensile tangential stresses in the SiC layer at earlier stages of operation.

- The burnup levels considered here in this study are much higher than the operational discharge burnup for HTTR (about 3.8% FIMA). Higher burnup values are observed for the particles tested in experiments. Failure probabilities calculated in this study are quite high for the higher burnup values. Although cases presented here are relevant for the HTTR, similar cases may be analyzed for other reactors.

- One of the solutions for avoiding the high tensile stress values inside the layers is increasing the thickness of the buffer layer. Since the buffer layer has half the density of its fully dense material form, increasing its thickness will provide empty volume for the fission and CO gases.

The current study may be extended to cover the following areas:

- The results presented in this study only take the kernel migration and pressure vessel failure modes into account. Failure probabilities for the other failure modes should also be evaluated to correctly predict the coated fuel particle integrity.

- The present study does not take into account the CO_2 formation and compression of the buffer layer by kernel migration.

- The analysis reflects only the results for CFPs with a UO_2 kernel. A similar analysis may be performed for a CFP with a PuO_2 kernel, which operates under higher temperature and higher burnup conditions. Also, different temperature gradients may be imposed to broaden the scope of kernel migration analysis.

Chapter 7

Reactivity Insertion Accident

An important class of potential accidents for reactors in general is the sudden increase in reactor local or core-wide power due to a reactivity increase. This might be caused by a control system malfunction, control rod ejection, or a sudden change in the core internal arrangement such as pebble compaction in a pebble bed reactor.

Because of the constant cycling of the fuel, a pebble bed reactor has low excess reactivity. The prismatic core design is more like an LWR in terms of excess reactivity (and burnable poisons) at the start of life, which is reduced as the core nears the end of life [4].

A sudden pulse of power might damage the fuel elements and the fuel particles, leading to a large release of fission products from the fuel. If the pressure boundary has also been damaged, such as in a rod ejection accident, a driving force would be available to potentially transport fission products outside of the reactor boundary.

The large amount of graphite in the core along with its high heat capacity eliminates concerns of core melting, but the kernel can still see high temperatures and the resulting pressures can fail coatings.

In this study, one of the scenarios for sudden increase in reactor power due to reactivity insertion is analyzed. The scenario includes sudden insertion of reactivity due to withdrawal of one of the control rods in the HTR-10 reactor. The reactivity control and shutdown systems are assumed not to be available during the event.

7.1 HTR-10 Reactor

The 10 MW high temperature gas cooled reactor (HTR-10) is a graphite-moderated helium cooled reactor with the outlet temperature of 700 °C. HTR-10 fuel is the pebble bed type. Key design parametres are presented in Table 7.1 [2].

Fuel elements used are spherical pebbles 6 cm in diameter filled with coated particles. The reactor equilibrium core contains about 27,000 fuel elements forming

Table 7.1: Key design parameters of the HTR-10

Reactor thermal power (MW)	10
Primary helium pressure (MPa)	3.0
Reactor core diameter (m)	1.8
Average core height (m)	1.97
Average helium temperature at reactor outlet (°C)	700
Average helium temperature at reactor inlet (°C)	250
Helium mass flow rate at full power (kg/s)	4.3
Number of control rods in side reflector	10
Number of absorber ball units in side reflector	7
Nuclear fuel	UO_2
Heavy metal loading per fuel element (g)	5
Enrichment of fresh fuel element	17%
Number of fuel elements in equilibrium core	27,000
Fuel loading mode	Multi-pass

a pebble bed. The fuel element characteristics are presented in Table 7.2 [2]. Fuel element schematic is presented in Figure 7.1.

Table 7.2: Fuel element characteristics

Diameter of ball (cm)	6
Diameter of fuel zone (cm)	5
Density of graphite in matrix and outer shell (g/cm^3)	2.2
Heavy metal (uranium) loading (weight) per ball (g)	5.0
Volumetric filling fraction of balls in the core	0.61
Radius of the fuel kernel (μm)	250
UO_2 density (g/cm^3)	10.4
Coating layer materials (starting from buffer)	PyC/PyC/SiC/PyC
Coating layer thickness (μm)	90/40/35/40
Coating layer density (g/cm^3)	1.1/1.9/3.18/1.9

7.2 Previous Studies

Safety demonstration tests on the 10 MW High Temperature Gas-cooled Reactor (HTR-10) were conducted to demonstrate the inherent safety features as well as to obtain the core and primary cooling system transient data for validation of safety analysis codes. These tests have been performed at 3 MW (Ref. [60]). One of these tests include withdrawal of one of the control rods of the HTR-10 reactor. The reactor

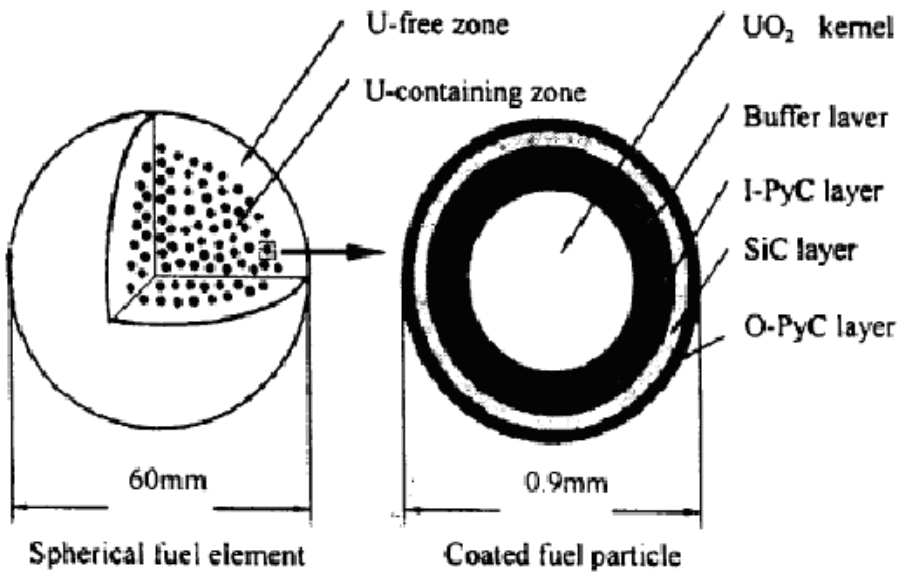

Figure 7.1: HTR-10 fuel element [2]

power increases 2.3 times and then decreases due to the strong temperature feedback of the reactor, without the actuation of the safety systems.

Other studies [4] involve prediction of coated fuel particle behavior by pulse tests. Those performed in Japan and Russia involve a set of different types of coated fuel particles tested under relatively high reactivity insertion. The analysis aims to determine the energy deposition inside the kernel. However, the reactivity insertions in the tests are relatively fast when compared to real reactor conditions. As a result, particles with vaporized kernels and failed coating layers are observed during these tests.

7.3 Analysis Methodology

This study analyzes the HTR-10 coated fuel particle behavior during a reactivity insertion accident in which the reactivity control system is not available. The transient scenario includes withdrawal of one of the control rods located at the reflector, which causes a reactivity insertion of 1.4×10^{-2} Δk/k (\$2.18) in 200 seconds.

Since the change of reactivity with time is determined as a linear ramp, the change of power and delayed neutron precursor concentration with time can be calculated. One effective delayed neutron group is employed in point kinetics equations for the sake of simplicity. However, the analysis can be extended to six groups of precursors. The Runge-Kutta method is employed for numerical solution of the point kinetics equations.

The reactivity insertion analysis is performed for a number of time steps. The model involves three parts:

1. Solution of the point kinetics equations with temperature feedbacks taken into account and determining the power level at the specified time step.

2. Determination of the temperature distribution inside the pebble employing the power obtained from the point kinetics equations for the specified time step in part 1.

3. Determination of the temperature distribution inside the coated fuel particle employing the power obtained from the point kinetics equations for the specified time step in part 1, together with the pebble temperature obtained in part 2 as a boundary condition.

All three parts provide input and output to each other and programmed to the finite element code ANSYS using APDL (Ansys Parametric Design Language).

Temperature distribution inside the pebble is determined by the analytical solution of nonhomogenous, two region, time dependent heat conduction equation in spherical coordinates. The pebble is assumed to be cooled by helium at 800 °C, which is 100 °C higher than the average helium outlet temperature of the HTR-10 reactor. The maximum value of He temperature in the original design is 950 °C [2]. Green's function method is employed for obtaining the solution, details of which are presented in the following sections. The temperature at the center of the pebble is taken as the surface temperature of the coated fuel particle as a conservative approach. The volume averaged temperature of the fueled region of the pebble is assumed to represent the moderator temperature and employed as an input to the point kinetics equations.

Since the coolant temperature is assumed constant in the analysis, change of reflector temperature is also neglected. Therefore, the feedback effect of reflector temperature change is not present in the current analysis.

Coated fuel particle temperature distribution is calculated by the finite element code ANSYS. Particle surface temperature obtained from the pebble temperature distribution and the power calculated at specified time steps are input values for the analysis. Maximum fuel temperature of the coated fuel particle is calculated to determine whether the design values are exceeded.

The flow chart for the calculation is presented in Figure 7.2 with the following parameters defined:

T_m^0 = initial moderator temperature

T_f^0 = initial fuel temperature

$T_{sur,p}(t)$ = particle surface temperature

$P(t)$ = power

$\rho_i(t)$ = reactivity inserted due to control rod withdrawal

The analysis begins with determination of input parameters. These are geometry of the coated fuel particle and pebble, properties of materials and kinetic parameters.

First, the steady state temperature distribution for the coated fuel particle is calculated. The initial temperature distribution inside the pebble is determined by analytical solution. Also, coefficients of the analytical solution are obtained to calculate the moderator temperature (i.e. the average temperature of the fueled region of the pebble) and the coated fuel particle surface temperature (i.e. the temperature at the center of the pebble) at each time step.

Initial values of the moderator and fuel temperatures from the initial parameters step provides input to the point kinetics equations. Kinetic parameters and change of external reactivity with time are also employed in the point kinetics step.

The point kinetics step calculates normalized power for each time step and provides the power level for calculation of the temperature distribution inside the pebble and coated fuel particle. The results of the analysis provide change of temperatures

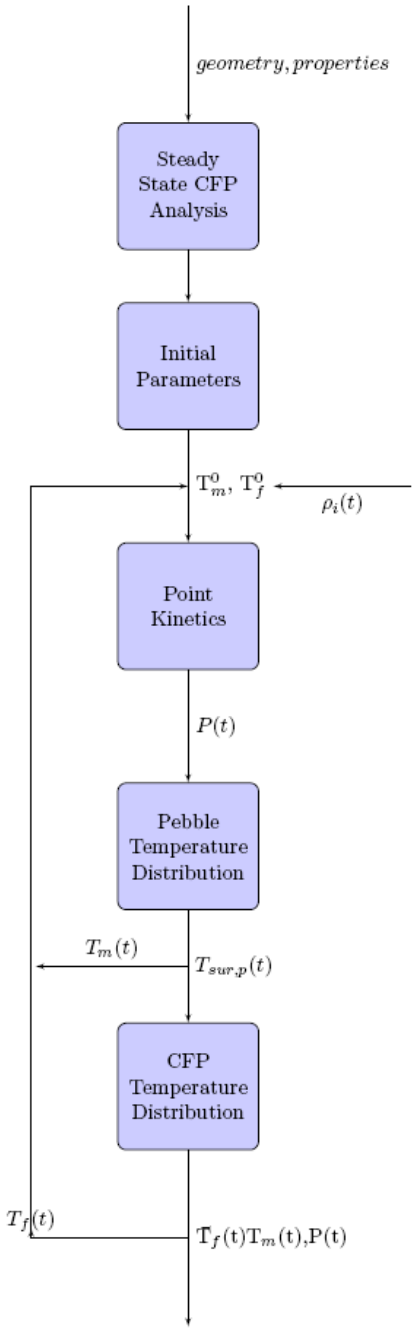

Figure 7.2: Flowchart of the APDL code

for the CFP and the pebble with time.

In the mechanical analysis of the reactivity insertion accident, temperature and power distributions are employed to calculate the stress distribution inside the load bearing layers.

7.3.1 Point Kinetics Equations

The effect of reactivity on power is described by the point reactor kinetics model. The input values for the point reactor kinetics equations are initial values of power and delayed neutron precursor concentrations, kinetic parameters, and external reactivity as a function of time. The output of the point reactor kinetics equations are the power and delayed neutron precursor concentrations at each time step. Point kinetics equations are presented in Equations 7.1, 7.2 [61].

$$\frac{dP(t)}{dt} = \frac{\rho(t)-\beta}{\Lambda}P(t) + \sum_{i=1}^{J}\lambda_i C_i(t) \tag{7.1}$$

$$\frac{dC_i(t)}{dt} = \frac{\beta_i}{\Lambda}P(t) - \lambda_i C_i(t) \tag{7.2}$$

where

$P(t)$ = power as a function of time
$C_i(t)$ = concentration for delayed neutron precursor group i
$\rho(t)$ = reactivity as a function of time
β_i = delayed neutron fraction for precursor group i
β = $\sum_{i=1}^{J}\beta_i$
λ_i = decay constant for precursor group i
Λ = prompt neutron lifetime

The above equations are valid for J groups of delayed neutron precursors, where J is usually six. With the assumption of one effective group of delayed neutrons, the following equations are obtained:

$$\lambda = <\lambda> = \left[\frac{1}{\beta}\sum_{i=1}^{J}\frac{\beta_i}{\lambda_i}\right]^{-1} \tag{7.3}$$

and one group point kinetics equations become:

$$\frac{dP}{dt} = \frac{\rho(t)-\beta}{\Lambda}P(t) + \lambda C(t) \tag{7.4}$$

$$\frac{dC}{dt} = \frac{\beta}{\Lambda}P(t) - \lambda C(t) \tag{7.5}$$

Neutron kinetics parameters are presented in Table 7.3 [62]. Calculations are performed for the equilibrium core.

Table 7.3: Neutron kinetics parameters for HTR-10 reactor

	initial core	equilibrium core
β	0.00726	0.0066
Λ (s)	0.00168	0.00119
λ (s)	0.10245	0.09696

The change of reactivity with time is presented as:

$$\rho(t) = \rho_i(t) + \rho_{fb}(t) + \rho_c(t) \tag{7.6}$$

where

$\rho_i(t)$ = reactivity caused by initiating event (e.g. control rod ejection)

$\rho_{fb}(t)$ = reactivity from temperature feedbacks

$\rho_c(t)$ = reactivity from power control system

In the current study, the control systems are assumed to be unavailable (except for maintaining the initial steady state) and the reactivity is expressed only with the reactivity from the initiating event and from feedbacks. Reactivity from temperature feedbacks is expressed in three terms:

$$\rho_{fb}(t) = \alpha_f \, \Delta T_f(t) + \alpha_m \, \Delta T_m(t) + \alpha_r \, \Delta T_r(t) \tag{7.7}$$

where

α_f = fuel temperature coefficient of reactivity

ΔT_f = temperature change in fuel with respect to reference temperature

α_m = moderator temperature coefficient of reactivity

ΔT_m = temperature change in moderator with respect to reference temperature

α_r = reflector temperature coefficient of reactivity

ΔT_r = temperature change in reflector with respect to reference temperature

In the current study, temperature change in the reflector is assumed to be negligible for the transient. Therefore, only the effects of fuel and moderator feedback coefficients are taken into consideration. The feedback coefficients for the initial and equilibrium core are presented in Table 7.4 [62].

Table 7.4: Temperature coefficients of reactivity

	initial core	equilibrium core
fuel $(\Delta k/k)/°\text{C}$	-1.42×10^{-5}	-2.55×10^{-5}
moderator $(\Delta k/k)/°\text{C}$	-10.8×10^{-5}	-5.62×10^{-5}
reflector $(\Delta k/k)/°\text{C}$	$+5.14 \times 10^{-5}$	$+4.29 \times 10^{-5}$

The Runge-Kutta Method is employed to solve the point kinetics equations. The Runga-Kutta algorithm is programmed as an APDL code in ANSYS.

7.3.2 Solution of Heat Conduction Equation Inside the Pebble

The Green's function approach can be used to solve the nonhomogeneous problems of heat conduction in composite medium. The heat conduction equation in a multi-layered spherically symmetric system is:

$$\frac{\partial T_i}{\partial t} = \alpha_i \frac{1}{r^2}\frac{\partial}{\partial r}\left(r^2 \frac{\partial T_i}{\partial r}\right) + \frac{\alpha_i}{k_i} g_i(r,t), \qquad r_i < r < r_{i+1}, \quad i = 1, \ldots, M \tag{7.8}$$

where $T_i(r,t)$ is the time dependent temperature at point r in region i, $g_i(r,t)$ is the heat generation rate per unit volume at point r in region i, $\alpha_i = k_i/(\rho c_p)_i$ and k_i are the thermal diffusivity and conductivity of region i, respectively, and M is the number of concentric spherical regions. The internal and external boundary conditions are:

$$\begin{aligned}
&T_1(r_1 = 0, t) \quad \text{finite} \\
&T_i(r_{i+1}, t) = T_{i+1}(r_{i+1}, t), \quad \text{and} \\
&k_i \frac{\partial T_i}{\partial r}|_{r_{i+1}} = k_{i+1} \frac{\partial T_{i+1}}{\partial r}|_{r_{i+1}}, \qquad i = 1, \ldots, M-1 \\
&-k_M \frac{\partial T_M}{\partial r}|_{r_{M+1}} = h_{M+1} T_M(r_{M+1}, t)
\end{aligned} \tag{7.9}$$

where h_{M+1} is the heat transfer coefficient just outside the outermost region M. The ambient temperature of the outside is assumed constant and T_i's are measured with respect to this datum.

Initially, the temperature distribution is assumed to satisfy the steady state form of the equation 7.8, together with the boundary conditions 7.9, as follows:

$$
\begin{aligned}
&T_i(r,0) = F_i(r) \quad \text{with} \\
&\frac{1}{r^2}\frac{d}{dr}\left(r^2\frac{dF_i}{dr}\right) + \frac{1}{k_i}g_i(r) = 0, \qquad i = 1,\ldots,M \\
&F_1(r_1 = 0) \quad \text{finite} \\
&F_i(r_{i+1}) = F_{i+1}(r_{i+1}), \quad \text{and} \\
&k_i\frac{dF_i}{dr}|_{r_{i+1}} = k_{i+1}\frac{dF_{i+1}}{dr}|_{r_{i+1}}, \qquad i = 1,\ldots,M-1 \\
&-k_M\frac{dF_M}{dr}|_{r_{M+1}} = h_{M+1}F_M(r_{M+1})
\end{aligned}
\tag{7.10}
$$

where $F_i(r)$ is the initial temperature and $g_i(r) \equiv g_i(r,0)$ is the steady state heat generation rate per unit volume, both at point r in region i.

The general solution of the heat conduction equation with initial and boundary conditions, as defined in Eqs. 7.8, 7.9 and 7.10, with the Green's function method is [58]:

$$
\begin{aligned}
T_i(r,t) = \sum_{j=1}^{M} \Bigg\{ &\int_{r'=r_j}^{r_{j+1}} r'^{\,2}\, G_{ij}(r,t|r',\tau)_{\tau=0}\, F_j(r')\, dr' \\
&+ \int_{\tau=0}^{t} d\tau \int_{r'=r_j}^{r_{j+1}} r'^{\,2}\, G_{ij}(r,t|r',\tau)\, [\frac{\alpha_j}{k_j}\, g_j(r',\tau)]\, dr' \Bigg\}
\end{aligned}
\tag{7.11}
$$

where i and j are region indices and $G_{ij}(r,t|r',\tau)$ is the Green's function for regions i and j, which is the temperature at (r,t) in region i due to an instantaneous unit source at (r',τ) in region j. The Green's function $G_{ij}(r,t|r',\tau)$ satisfies the time dependent heat conduction equation 7.8 with instantaneous unit source $\delta(r-r')\delta(t-\tau)$, together with the boundary conditions 7.9. Initial conditions do not play a role in finding the Green's function; however, they certainly are essential in finding the temperature distribution, as indicated in equation 7.11.

The Green's function can be obtained as follows [58]. First, seperation of variables can be applied to the heat conduction equation at all points (r,t) except the source point (r',τ). If β_n^2 are the separation constants, then the spatial equations

become:

$$
\begin{aligned}
&\alpha_i \frac{1}{r^2}\frac{d}{dr}\left(r^2\frac{d\psi_{i,n}(r)}{dr}\right) = -\beta_n^{\,2}\,\psi_{i,n}(r), \qquad i = 1,\ldots,M \\
&\psi_{1,n}(r_1 = 0) \quad \text{finite} \\
&\psi_{i,n}(r_{i+1}) = \psi_{i+1,n}(r_{i+1}), \quad \text{and} \\
&k_i \frac{d\psi_{i,n}}{dr}|_{r_{i+1}} = k_{i+1}\frac{d\psi_{i+1,n}}{dr}|_{r_{i+1}}, \qquad i = 1,\ldots,M-1 \\
&-k_M \frac{d\psi_{M,n}}{dr}|_{r_{M+1}} = h_{M+1}\psi_{M,n}(r_{M+1})
\end{aligned}
\tag{7.12}
$$

where $\psi_{i,n}(r)$ is the solution in region i corresponding to nth seperation constant:

$$
\psi_{i,n}(r) = A_{i,n}\,\frac{1}{r}\,\sin\left(\frac{\beta_n}{\sqrt{\alpha_i}}\,r\right) + B_{i,n}\,\frac{1}{r}\,\cos\left(\frac{\beta_n}{\sqrt{\alpha_i}}\,r\right) \tag{7.13}
$$

$A_{i,n}$ and $B_{i,n}$ being constants. Equations 7.12 with solutions 7.13 uniquely determine the eigenvalues β_n and the eigenfunctions $\psi_{i,n}$ apart from an overall multiplicative constant.

The Green's function of equation 7.11 can be expressed in terms of the eigenfunctions of 7.12 as follows:

$$
G_{ij}(r,t|r',\tau) = \sum_{n=1}^{\infty} e^{-\beta_n^{\,2}\,(t-\tau)}\,\frac{1}{N_n}\,\frac{k_j}{\alpha_j}\,\psi_{i,n}(r)\,\psi_{j,n}(r') \tag{7.14}
$$

where N_n is the normalization constant defined as:

$$
N_n = \sum_{j=1}^{M}\frac{k_j}{\alpha_j}\int_{r'=r_j}^{r_{j+1}} r'^{\,2}\,\psi_{j,n}^2(r')\,dr' \tag{7.15}
$$

Substitution of equation 7.14 into equation 7.11 yields:

$$
\begin{aligned}
T_i(r,t) &= \sum_{n=1}^{\infty}\sum_{j=1}^{M}\left\{\int_{r'=r_j}^{r_{j+1}} r'^{\,2}\,e^{-\beta_n^{\,2}\,t}\,\frac{1}{N_n}\,\frac{k_j}{\alpha_j}\,\psi_{i,n}(r)\,\psi_{j,n}(r')\,F_j(r')\,dr'\right. \\
&+ \left.\int_{\tau=0}^{t} d\tau\int_{r'=r_j}^{r_{j+1}} r'^{\,2}\,e^{-\beta_n^{\,2}\,(t-\tau)}\,\frac{1}{N_n}\,\psi_{i,n}(r)\,\psi_{j,n}(r')\,g_j(r',\tau)\,dr'\right\} \\
&= \sum_{n=1}^{\infty}\sum_{j=1}^{M}\left\{e^{-\beta_n^{\,2}\,t}\,\frac{1}{N_n}\,\frac{k_j}{\alpha_j}\,\psi_{i,n}(r)\int_{r'=r_j}^{r_{j+1}} r'^{\,2}\,\psi_{j,n}(r')\,F_j(r')\,dr'\right. \\
&+ \left.\int_{r'=r_j}^{r_{j+1}} dr'\,r'^{\,2}\,\frac{1}{N_n}\,\psi_{i,n}(r)\,\psi_{j,n}(r')\int_{\tau=0}^{t} d\tau\,e^{-\beta_n^{\,2}\,(t-\tau)}\,g_j(r',\tau)\right\}
\end{aligned}
\tag{7.16}
$$

In this equation, the first term represents the effect of the initial distribution, which decays exponentially with time; and the second term is due to the heat source, where the effect of heat generated closer to time t is pronounced and those in the past are subdued. Thus, $T_i(r,t)$ starts with the initial distribution and follows the heat generation rate more and more closely as transient progresses.

Further simplification is possible for the integral of the first term in equation 7.16 due to the similarity between equations 7.10 and 7.12. Substitution yields:

$$\begin{aligned} & \sum_{j=1}^{M} \frac{k_j}{\alpha_j} \int_{r=r_j}^{r_{j+1}} r^2\, \psi_{j,n}(r)\, F_j(r)\, dr \\ = & \sum_{j=1}^{M} \frac{k_j}{\alpha_j} \int_{r=r_j}^{r_{j+1}} dr\, r^2 \left[\frac{-\alpha_j}{\beta_n^{\,2}} \frac{1}{r^2} \frac{d}{dr} \left(r^2 \frac{d\psi_{j,n}(r)}{dr} \right) \right] F_j(r) \end{aligned} \tag{7.17}$$

Integrating by parts twice, using internal and external boundary conditions in equations 7.10 and 7.12, and simplifying yields:

$$\sum_{j=1}^{M} \frac{k_j}{\alpha_j} \int_{r=r_j}^{r_{j+1}} r^2\, \psi_{j,n}(r)\, F_j(r)\, dr \;=\; \frac{1}{\beta_n^{\,2}} \sum_{j=1}^{M} \int_{r=r_j}^{r_{j+1}} r^2\, \psi_{j,n}(r)\, g_j(r)\, dr \tag{7.18}$$

Therefore, equation 7.16 becomes:

$$\begin{aligned} T_i(r,t) \;=\; & \sum_{n=1}^{\infty} \sum_{j=1}^{M} \left\{ e^{-\beta_n^{\,2} t} \frac{1}{N_n}\, \psi_{i,n}(r) \frac{1}{\beta_n^{\,2}} \int_{r'=r_j}^{r_{j+1}} r'^{\,2}\, \psi_{j,n}(r')\, g_j(r')\, dr' \right. \\ & + \left. \int_{r'=r_j}^{r_{j+1}} dr'\, r'^{\,2} \frac{1}{N_n}\, \psi_{i,n}(r)\, \psi_{j,n}(r') \int_{\tau=0}^{t} d\tau\, e^{-\beta_n^{\,2}(t-\tau)}\, g_j(r',\tau) \right\} \\ = \; & \sum_{n=1}^{\infty} \frac{1}{N_n}\, \psi_{i,n}(r) \sum_{j=1}^{M} \int_{r'=r_j}^{r_{j+1}} dr'\, r'^{\,2}\, \psi_{j,n}(r') \;\cdot \\ & \cdot \left\{ \frac{e^{-\beta_n^{\,2} t}}{\beta_n^{\,2}}\, g_j(r') + \int_{\tau=0}^{t} d\tau\, e^{-\beta_n^{\,2}(t-\tau)}\, g_j(r',\tau) \right\} \end{aligned} \tag{7.19}$$

As can be easily verified from equation 7.19, if $g_j(r,t) = g_j(r,0)$ for all t, then $T_i(r,t) = T_i(r,0)$ for all t.

Equation 7.19 can now be applied to the two-region spherical pebble of an HTR ($M = 2$). The coated fuel particles are assumed to be dispersed inside a graphite sphere of radius a, which is covered with a pure graphite spherical shell of thickness $b - a$. Uniform heat generation in the central fueled region and no heat generation in

the outside shell is assumed, i.e., $g_1(r,t) = q'''(t),\ g_2(r,t) = 0$. Equation 7.19 for the fueled region ($i = 1$) and the graphite region ($i = 2$) becomes:

$$T_1(r,t) = \sum_{n=1}^{\infty} \frac{1}{N_n}\,\psi_{1,n}(r) \left(\int_0^a dr'\, r'^{\,2}\, \psi_{1,n}(r') \right) \cdot \cdot \left(\frac{e^{-\beta_n^2\, t}}{\beta_n^{\,2}}\, q_0''' \;+\; \int_0^t d\tau\, e^{-\beta_n^2\,(t-\tau)}\, q'''(\tau) \right) \tag{7.20}$$

and

$$T_2(r,t) = \sum_{n=1}^{\infty} \frac{1}{N_n}\,\psi_{2,n}(r) \left(\int_0^a dr'\, r'^{\,2}\, \psi_{1,n}(r') \right) \cdot \cdot \left(\frac{e^{-\beta_n^2\, t}}{\beta_n^{\,2}}\, q_0''' \;+\; \int_0^t d\tau\, e^{-\beta_n^2\,(t-\tau)}\, q'''(\tau) \right) \tag{7.21}$$

or, substituting equation 7.12 and integrating by parts once:

$$T_1(r,t) = \sum_{n=1}^{\infty} \frac{1}{N_n}\,\psi_{1,n}(r) \left(-\frac{\alpha_1}{\beta_n^{\,2}}\, a^2\, \left.\frac{d\psi_{1,n}}{dr}\right|_{r=a} \right) \cdot \cdot \left(\frac{e^{-\beta_n^2\, t}}{\beta_n^{\,2}}\, q_0''' \;+\; \int_0^t d\tau\, e^{-\beta_n^2\,(t-\tau)}\, q'''(\tau) \right) \tag{7.22}$$

and

$$T_2(r,t) = \sum_{n=1}^{\infty} \frac{1}{N_n}\,\psi_{2,n}(r) \left(-\frac{\alpha_1}{\beta_n^{\,2}}\, a^2\, \left.\frac{d\psi_{1,n}}{dr}\right|_{r=a} \right) \cdot \cdot \left(\frac{e^{-\beta_n^2\, t}}{\beta_n^{\,2}}\, q_0''' \;+\; \int_0^t d\tau\, e^{-\beta_n^2\,(t-\tau)}\, q'''(\tau) \right) \tag{7.23}$$

where $q_0''' = q'''(0)$. The eigenfunctions of equation 7.13 becomes:

$$\psi_{1,n}(r) = A_{1,n}\,\frac{1}{r}\,\sin\left(\frac{\beta_n}{\sqrt{\alpha_1}}\,r\right) + B_{1,n}\,\frac{1}{r}\,\cos\left(\frac{\beta_n}{\sqrt{\alpha_1}}\,r\right) \tag{7.24}$$

$$\psi_{2,n}(r) = A_{2,n}\,\frac{1}{r}\,\sin\left(\frac{\beta_n}{\sqrt{\alpha_2}}\,r\right) + B_{2,n}\,\frac{1}{r}\,\cos\left(\frac{\beta_n}{\sqrt{\alpha_2}}\,r\right) \tag{7.25}$$

Applying boundary conditions 7.12 yields:

$$
\begin{aligned}
&B_{1,n} = 0 \\
&A_{2,n} = \frac{A_{1,n}}{2}\Bigg[\left(1+\frac{k_1}{k_2}\frac{\sqrt{\alpha_2}}{\sqrt{\alpha_1}}\right)\cos\beta_n a\left(\frac{1}{\sqrt{\alpha_1}}-\frac{1}{\sqrt{\alpha_2}}\right) \\
&-\left(1-\frac{k_1}{k_2}\frac{\sqrt{\alpha_2}}{\sqrt{\alpha_1}}\right)\cos\beta_n a\left(\frac{1}{\sqrt{\alpha_1}}+\frac{1}{\sqrt{\alpha_2}}\right) \\
&+\frac{(k_2-k_1)\sqrt{\alpha_2}}{k_2\,\beta_n\,a}\left\{\sin\beta_n a\left(\frac{1}{\sqrt{\alpha_1}}-\frac{1}{\sqrt{\alpha_2}}\right)+\sin\beta_n a\left(\frac{1}{\sqrt{\alpha_1}}+\frac{1}{\sqrt{\alpha_2}}\right)\right\}\Bigg] \\
&B_{2,n} = \frac{A_{1,n}}{2}\Bigg[\left(1+\frac{k_1}{k_2}\frac{\sqrt{\alpha_2}}{\sqrt{\alpha_1}}\right)\sin\beta_n a\left(\frac{1}{\sqrt{\alpha_1}}-\frac{1}{\sqrt{\alpha_2}}\right) \qquad (7.26)\\
&+\left(1-\frac{k_1}{k_2}\frac{\sqrt{\alpha_2}}{\sqrt{\alpha_1}}\right)\sin\beta_n a\left(\frac{1}{\sqrt{\alpha_1}}+\frac{1}{\sqrt{\alpha_2}}\right) \\
&-\frac{(k_2-k_1)\sqrt{\alpha_2}}{k_2\,\beta_n\,a}\left\{\cos\beta_n a\left(\frac{1}{\sqrt{\alpha_1}}-\frac{1}{\sqrt{\alpha_2}}\right)-\cos\beta_n a\left(\frac{1}{\sqrt{\alpha_1}}+\frac{1}{\sqrt{\alpha_2}}\right)\right\}\Bigg]
\end{aligned}
$$

together with the equation for eigenvalues:

$$
\begin{aligned}
&\left\{\left(\frac{\beta_n b}{\sqrt{\alpha_2}}\right)^2\left(1+\frac{k_1}{k_2}\frac{\sqrt{\alpha_2}}{\sqrt{\alpha_1}}\right)+(1-Bi_2)\left(1-\frac{k_1}{k_2}\right)\frac{b}{a}\right\}\cos\beta_n\left(\frac{a}{\sqrt{\alpha_1}}+\frac{b-a}{\sqrt{\alpha_2}}\right) \\
&-\left\{\left(\frac{\beta_n b}{\sqrt{\alpha_2}}\right)^2\left(1-\frac{k_1}{k_2}\frac{\sqrt{\alpha_2}}{\sqrt{\alpha_1}}\right)+(1-Bi_2)\left(1-\frac{k_1}{k_2}\right)\frac{b}{a}\right\}\cos\beta_n\left(\frac{a}{\sqrt{\alpha_1}}-\frac{b-a}{\sqrt{\alpha_2}}\right) \qquad (7.27)\\
&+\left(\frac{\beta_n b}{\sqrt{\alpha_2}}\right)\Bigg\{\left[\left(1-\frac{k_1}{k_2}\right)\frac{b}{a}-(1-Bi_2)\left(1+\frac{k_1}{k_2}\frac{\sqrt{\alpha_2}}{\sqrt{\alpha_1}}\right)\right]\sin\beta_n\left(\frac{a}{\sqrt{\alpha_1}}+\frac{b-a}{\sqrt{\alpha_2}}\right) \\
&+\left[\left(1-\frac{k_1}{k_2}\right)\frac{b}{a}-(1-Bi_2)\left(1-\frac{k_1}{k_2}\frac{\sqrt{\alpha_2}}{\sqrt{\alpha_1}}\right)\right]\sin\beta_n\left(\frac{a}{\sqrt{\alpha_1}}-\frac{b-a}{\sqrt{\alpha_2}}\right)\Bigg\}=0
\end{aligned}
$$

where $Bi_2 = h_3 b/k_2$ and $h_3 \equiv h_{He}$, the heat transfer coefficient between the pebble and the coolant gas He. N_n can be calculated from equation 7.15, which is proportional to $A_{1,n}^2$. Therefore, $A_{1,n}$ cancels out in equations 7.22 and 7.23, and can be taken as unity in equation 7.26.

To summarize: once the dimensions and material properties are known, eigenvalues β_n^2 are calculated from 7.27, and the eigenfunctions from 7.24, 7.25 and 7.26. Substituting these into equations 7.22 and 7.23, and adding the datum temperature T_{He}, yields the temperature distribution inside the pebble for the fueled and the

non-fueled graphite regions, respectively.

For practical applications, the infinite series in equations 7.22 and 7.23 need to be truncated. The fact that these equations to reproduce the initial temperature distribution, which is assumed to be that of the steady state, provides a simple way to determine the number of terms to be retained. The steady state distribution, obtained by solving equations 7.10 for two regions, is the following:

$$F_1(r) = \frac{q_0''' \, a^3}{3} \left[\frac{1}{k_2} \left(\frac{1}{a} - \frac{1}{b} \right) + \frac{1}{2k_1 \, a} \left(1 - \frac{r^2}{a^2} \right) + \frac{1}{b^2 \, h_{He}} \right] + T_{He} \quad (7.28)$$

$$F_2(r) = \frac{q_0''' \, a^3}{3} \left[\frac{1}{k_2} \left(\frac{1}{r} - \frac{1}{b} \right) + \frac{1}{b^2 \, h_{He}} \right] + T_{He} \quad (7.29)$$

It was observed that, using 5 terms from equations 7.22 and 7.23 at $t = 0$ reproduces the distributions 7.28 and 7.29 to an acceptable accuracy.

In the thermal analysis of the coated fuel particle, the volume averaged value of $T_1(r, t)$ is used as the moderator temperature value. Also, the temperature value at the center of the pebble, $T_1(0, t)$, is employed as the surface temperature of the coated fuel particle.

Table 7.5 presents material properies for fueled (region 1) and non-fueled (region 2) regions of the pebble. The model geometry is presented in Figure 7.1 [59, 25, 64]. The fueled region is composed of 15,000 particles embedded inside the carbon matrix, so the material property calculations involve volume averaged values.

Table 7.5: Pebble material properties for thermal analysis

	Fueled region (1)	Non-fueled region (2)
k (W/m.K)	38.74	40
ρ (kg/m^3)	2311	2200
c_p (J/kg.K)	1800	1800

7.3.3 Thermal Analysis of Coated Fuel Particle

Thermal analysis of the coated fuel particle involves determination of the temperature distribution inside the particle. The heat generation inside the kernel is calculated by the point kinetics equations, taking into account the reactivity feedback

from temperature changes in the kernel and the moderator inside the pebble. The boundary condition for the coated fuel particle is the surface temperature, which is obtained from the temperature distribution inside the pebble, calculated by the analytical method described in the previous section, by evaluating at the pebble center.

Thermal analysis provides the power and temperatures as a function of time. In this study, an external reactivity insertion of $2 in 200 s, such as one of the control rods of the HTR-10 being withdrawn due to an earthquake would provide, is analyzed at full power. This is one of the Design Basis Accidents for the HTR-10 reactor.

With the assumption that no safety systems are available at the time of the accident, the reactor power increases to 2.8 times the initial power and stabilizes. Change of normalized power with time is presented in Figure 7.3 and temperatures in Figure 7.4. In this figure, moderator temperature is the spatial average of the temperature in the fueled region of the pebble, fuel surface temperature is the temperature at the pebble center and the fuel temperature is the temperature at the center of the kernel.

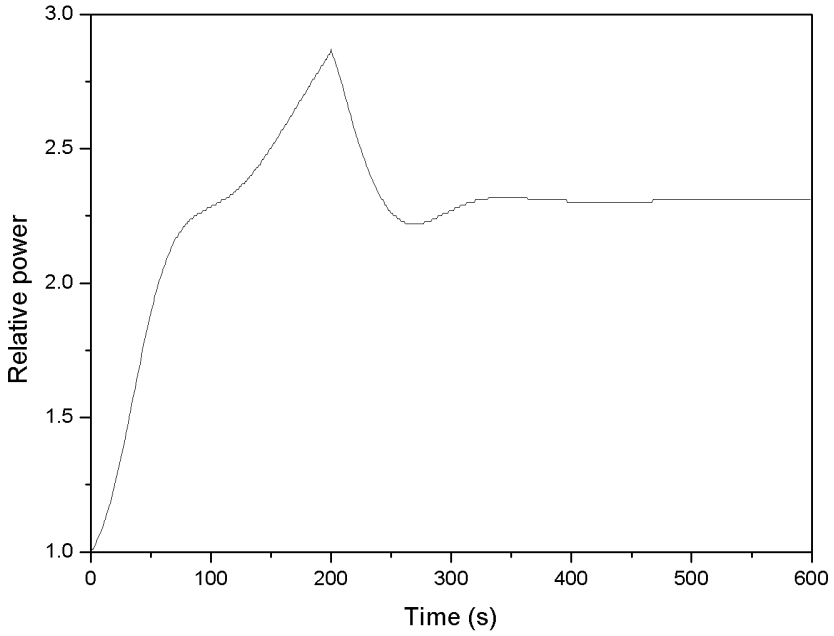

Figure 7.3: Change of power for $2 reactivity insertion accident

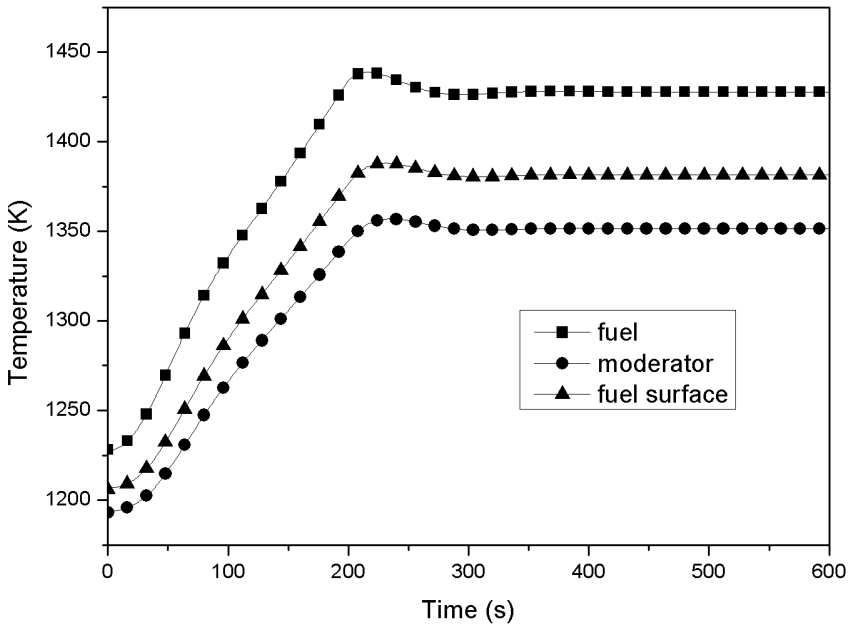

Figure 7.4: Change of temperatures for $2 reactivity insertion accident

As can be seen from the figure, fuel temperature change is about 200 K in such an accident. This change occurs in 200 s, which also causes an increase in fuel enthalpy. The maximum fuel temperature is 1440 K, which is below the operating limit temperature of the reactor.

The second part of the analysis involves determination of the stress distribution with time. Mechanical analysis is performed for the coated fuel particle that has the three load bearing layers. It employs temperature distributions from the thermal analysis. Under normal operating conditions, the particle goes up to 8% FIMA burnup at the end of 1050 days. The pressure inside the IPyC layer due to CO and fission gases is about 16 MPa at the end of 8% FIMA. Details on the finite element model for mechanical analysis is presented in Chapter 5. In analyzing the mechanical effect of the accident, the accident is assumed to occur at different burnup levels. From the beginning of life up to the burnup at which the accident occurs, the effects of thermal expansion, creep, swelling-shrinkage and the pressure build-up due to gases are taken into account.

For modelling the effect of the accident, which occurs in a relatively small time period when compared to the operation time, a second analysis is performed. This analysis assumes that increase in gas pressure due to increase in diffusion constant of the kernel as well as the gas temperature are the loads for the duration of the accident, together with thermal expansion. These loads depend on the time-dependent temperature distribution from thermal analysis. Creep and other long-term changes are neglected for the period of the accident. Figure 7.5 presents the change of tangential stress inside the IPyC layer with time. The magnitude of the tangential stress is reduced by increased loads during the reactivity insertion accident. However, it is the opposite for the SiC layer. As presented in Figure 7.6, the stress inside the SiC layer changes significantly during the accident. Especially at high burnup values, the SiC is under tension, therefore failure probability due to pressure vessel failure mode is pronounced. When the accident occurs at the end of life, the stress level will be about 50 MPa and the failure probability with Weibull distribution is calculated to be about 2×10^{-10}.

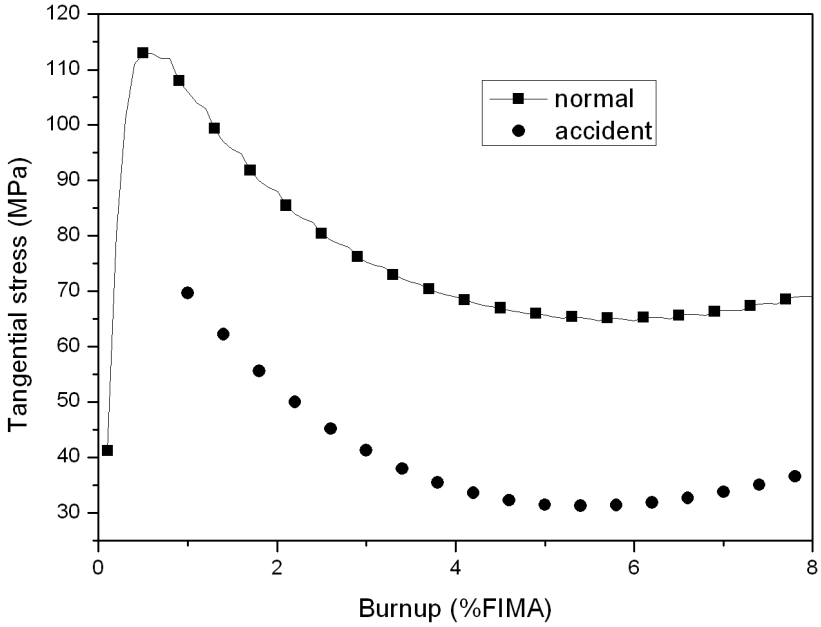

Figure 7.5: Stress distribution inside the IPyC for normal and accident conditions

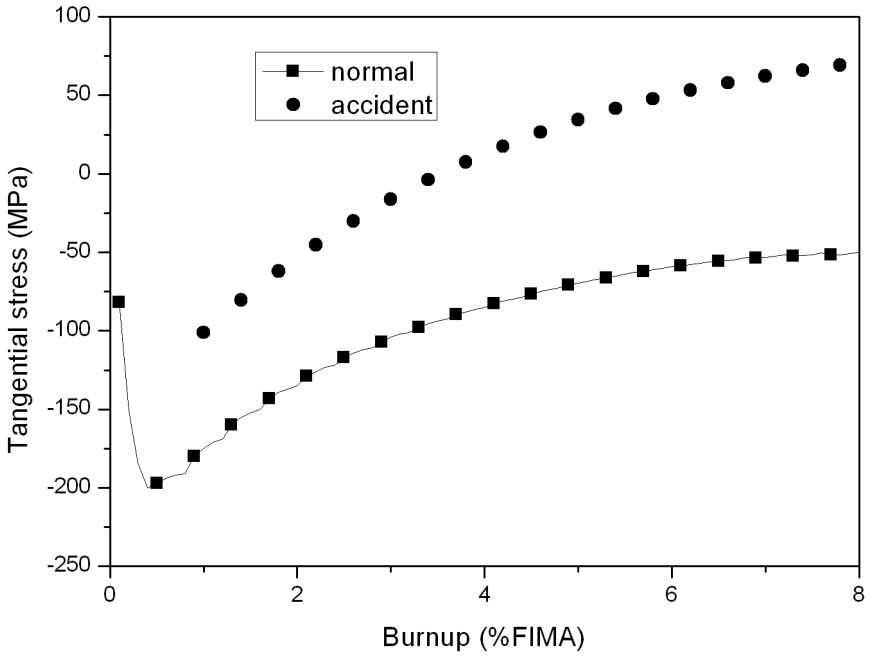

Figure 7.6: Stress distribution inside the SiC for normal and accident conditions

7.4 Conclusions

A reactivity insertion accident has been analyzed that includes the effect of temperature feedbacks for the HTR. The scenario for the accident involves withdrawal of one of the control rods, which has also been analyzed and simulated previously [62]. The analysis and experiments aim to show the inherently safe characteristic of the high temperature reactors. The main results of the analysis are:

- Feedbacks play an effective role in determining the power level of the reactor in case of a reactivity insertion accident. Results of the analysis show that in case of unavailabiliy of reactivity control systems, power level reaches a maximum value, starts to decrease and then stabilizes at a level. Power level has reached 2.8 times the initial value and is stabilized at a level of 2.2 times the initial power.

- Reactivity insertion accident causes a significant increase in fuel temperature, which is about 200 °C. This level is within the design limits of HTR-10 fuel in case of an accident [2]. Also, this value is under 1600 °C temperature limit, which is the general design limit for the SiC layer. This limitation is based on chemical reactions and attack of solid fission products on the SiC layer.

- It is assumed that the helium temperature is constant during the accident. Prediction of helium temperature behavior will provide more realistic results.

- Mechanical analysis results show an increase of tangential stress inside the SiC layer. This increase puts SiC under tension after 3% FIMA. The SiC layer is preferred to be in compression from the integrity point of view. Otherwise, the presence of failure probability is pronounced. Although the failure probability is small, tension of the SiC is clearly undesirable.

Chapter 8

Conclusions

This study presents an integrity analysis methodology for the coated fuel particle of HTRs. The methodology involves mechanical and thermal analyses. Mechanical analysis involves calculation of pressure inside the load bearing layers and prediction of stress distributions. Thermal analysis is used to determine temperature distribution inside the coated fuel particle.

Finite element analysis is employed in particle integrity studies. The finite element model developed in the present study takes into account all types of loads in normal operating conditions, which are pressure due to fission gases, thermal expansion, temperature loads, creep and swelling/shrinkage.

At the beginning of the study, a finite element model and associated integrity analysis methodology is proposed and tested with the benchmark cases. IAEA CRP-6 study is employed for model benchmarking. The results are consistent with the benchmark results of most of the countries participated in the study. CRP-6 study results are presented in Appendix A.

Three of failure modes has been analyzed in the study. Pressure vessel failure and kernel migration analysis has been performed as presented in Chapter 6. Reactivity insertion accident analysis is presented in Chapter 7.

The main conclusions of the kernel migration analysis for a UO_2 fueled kernel are presented below:

- Operating temperature is one of the key parameters in fuel particle failure.
- The effect of kernel migration itself is not so critical on fuel failure. Coated fuel particle failure is more pronounced when pressure vessel failure is probable.
- CO formation is a critical issue at high temperatures. The magnitude of the maximum stress experienced by the particle indicates the importance of CO.
- The integrity of the IPyC layer is also critical in determining the failure proba-

bility of the primary pressure boundary, the SiC layer.

For the reactivity insertion accident, the model takes into account the pebble temperature distribution and its effect on the coated fuel particle. Calculations are performed to obtain temperature distributions inside the pebble and the coated fuel particle caused by the change of power due to reactivity insertion. In case of unavailability of reactivity control systems, a high temperature reactor can stabilize its power level due to temperature feedback. This accident had been actually performed as a test in HTR-10 reactor at a lower power level.

The results of analysis show the increase in reactor power and its stabilized level at about 2 times the initial value for the specified scenario. However, the results are based on certain assumptions and those assumptions strongly affect the analysis results. Reactivity insertion accident also causes a significant increase in fuel temperature. This increase may reach to design limits at different operating conditions depending on the initial temperature. One important result of the analysis is the effect of the accident on mechanical response of the SiC layer. The SiC layer is under compression for normal operating conditions for the case analyzed. Compression turns to tension during the accident, which may lead to failure of the SiC layer; however, this tensile stress is calculated to be small for the present case.

The current study presents a coated fuel particle integrity analysis methodology. The methodology employs finite element models for mechanical and thermal parts. This methodology can be applied to different failure modes of the coated fuel particle except for failures due to chemical interactions. Different fuel materials as well as different coating materials and coating designs can be tested with this methodology, which can be the subject of future studies.

Bibliography

[1] Scherer W., 2002, Principles of HTR neutronics, HTR/ECS 2002 High Temperature Reactor School Topic Notes, Cadarache, France.

[2] IAEA-TECDOC-1382, 2003, Evaluation of high temperature gas cooled reactor performance: Benchmark analysis related to initial testing of the HTTR and HTR-10.

[3] Nickel H., Nabielek H., Pott G., Mehner A.W., 2002, Long time experience with the development of HTR fuel elements in Germany, Nuclear Engineering and Design, 217, 141-151.

[4] USNRC, 2002, TRISO Coated Particle Fuel Phenomenon Identification and Ranking Tables (PIRTs) for Fission Product Transport Due to Manufacturing, Operations and Accidents, NUREG/CR-6844, Vol.1.

[5] Gee D., 2002, The pebble bed modular reactor, EEE 460 WebProject.

[6] Brücher H., Fachinger J., 2002, HTR fuel back end, HTR/ECS 2002 Conference, Cadarache.

[7] Martin D.G., 2002, Considerations pertaining to the achievement of high burnups in HTR fuel, Nuclear Engineering and Design, 213, 241-258.

[8] Miller G.K., Petti D.A., Maki J.T., 2004, Consideration of the effects of partial debonding of the IPyC and particle asphericity on TRISO coated fuel behavior, Journal of Nuclear Materials, 334, 79-91.

[9] Martin D.G., 2004, Some simple analytical models to predict the irradiation performance of coated particles, paper presented at the 2nd Research Co-ordination Meeting on Coordinated Research Project 6 (CRP-6), Austria.

[10] Prados J.W., Scott J.L., 1967, Mathematical model for predicting coated particle behavior, Nuclear Applications, 3, 488-494.

[11] Kaae J.L., 1969, A mathematical model for calculating stresses in pyrocarbon and silicon carbide coated fuel particle, Journal of Nuclear Materials, 29, 249-266.

[12] Kaae J.L., 1969, A mathematical model for calculating stresses in a four-layer carbon-silicon-carbide-coated fuel particle, Journal of Nuclear Materials, 32, 322-329.

[13] Lu C., Danzer R., Fischer F.D., 2002, Fracture statistics of brittle materials: Weibull or normal distribution, Physical Review E, 65, 067102.

[14] Phelip M., 2004, European programme on high temperature reactor fuel technology, Presentation at Second CRP-6 Meeting, Vienna.

[15] Martin D.G., 2004, Uncertainties in material property values on the modelling of coated particle performance, Presentation at Second CRP-6 Meeting, Vienna.

[16] IAEA-TECDOC-1154, 2000, Irradiation in graphite due to fast neutrons in fission and fusion systems.

[17] Nabielek H., Verfondern K., Werner H., 2004, Can we predict coated particle failure? A conversation on CONVOL, PANAMA and other codes, Technical Meeing on Current Status and Future Prospects of Gas Cooled Reactor Fuels, IAEA, Vienna, Austria.

[18] Verfondern K., 2005, Prediction of Fuel Performance in Cases 9 - 14 of Normal Operation Benchmark with PANAMA, 3rd Research Coordination Meeting of CRP-6, Vienna, Austria.

[19] Verfondern K., Nabielek H., 1990, The mathematical basis of the PANAMA-I code for modeling pressure vessel failure of TRISO coated particles under accident conditions, HTA-IB-03/90, KFA, Jülich, Germany.

[20] Verfondern K., Sumita J., Ueta S., Sawa K., 2001, Modeling of fuel performance and metallic fission product release behavior during HTTR normal operating conditions, Nuclear Engineering and Design, 210, 225-238.

[21] McCardell R.K., Petti D.A., 1993, NP-MHTGR Fuel Development Program Results.

[22] Phelip M., Michel F., Pelletier M., Degeneve G., Guillermier P., 2004, The ATLAS fuel simulation code objectives, description and first results, 2nd International Topical Meeting on High Temperature Reactor Technology, Beijing, China.

[23] Guillermier P., Phelip M., 2003, CEA and AREVA R&D on HTR fuel technology, Technical Meeting on Current Status and Future Prospects of Gas Cooled Reactor Fuels, Vienna, Austria.

[24] Min K.Y., 2005, Calculations of IAEA CRP-6 benchmark cases using COPA, Third CRP-6 Meeting on Advances in HTGR Fuel Technology, IAEA, Vienna, Austria.

[25] Maki J.T., Miller G.K., TRISO coated fuel performance benchmark cases, Input parameters, 2005.

[26] Miller G.K., Petti D.A., Varacalle Jr. D.J., Maki J.T., 2003, Statistical approach and benchmarking for modeling of multi dimensional behavior in TRISO coated fuel particles, Journal of Nuclear Materials, 317,69-82.

[27] Miller G.K., Petti D.A., Maki J.T., Knudson D.L., 2006, An evaluation of the effects of SiC layer thinning on failure of TRISO coated fuel particles, Journal of Nuclear Materials, 355, 150-162.

[28] Miller G.K., Petti D.A., Maki J.T., Knudson D.L., 2004, Current capabilities of the fuel performance modeling code PARFUME, 2nd International Topical Meeting on High Temperature Reactor Technology, Beijing, China.

[29] Petti D., 2004, An overview of the AGR fuel development and qualification program, IAEA Coordinated Research Project Meeting, Austria.

[30] Petti D., 2004, Fuel performance benchmark results using the PARFUME code, IAEA Coordinated Research Project Meeting, Austria.

[31] Wanga J., Ballinger R.G., Macleana H.J., Diecker J.T., 2004, TIMCOAT: An integrated fuel performance model for coated particle fuel, 2nd International Topical Meeting on High Temperature Reactor Technology, China.

[32] Wang J., 2004, An integrated performance model for high temperature gas cooled reactor coated particle fuel, Ph.D. Thesis, MIT.

[33] Diecker J.T., 2005, Development of a high temperature gas cooled reactor TRISO coated particle fuel chemistry model, M.Sc. Thesis, MIT.

[34] Gelbard F., 2003, Analytical modeling of fission product releases by diffusion from multicoated fuel particles, SAND2002-3966.

[35] Bernard L.C., Jacoud J.L., Vesco P., 2002, An efficient model for the analysis of fission gas release, Journal of Nuclear Materials, 302, 125-134.

[36] Lösönen P., 2000, Methods for calculating diffusional gas release from spherical grains, Nuclear Engineering and Design, 196, 161-173.

[37] Minato K., Ogawa T., Sawa K., Ishikawa A., Tomita T., Iida S., 2002, Irradiation experiments on ZrC coated fuel particles for high temperature gas cooled reactors, Nuclear Technology, 130, 272-281.

[38] Maki J.T., Petti D.A., Knudson D.L., Miller G.K., 2007, The challenges associated with high burnup, high temperature and accelerated irradiation for TRISO-coated particle fuel, Journal of Nuclear Materials, doi: 10.1016/j. jnucmat.2007.05.019.

[39] Snead L.L., Nozawa T., Katoh Y., Byun T.S., Kondo S., Petti D.A., 2007, Handbook of SiC properties for fuel performance modeling, Journal of Nuclear Materials, doi: 10.1016/j.jnucmat.2007.05.016.

[40] IAEA, 2005, Compilation of IAEA CRP-6 normal operation fuel performance code benchmarks, CRP-6 Meeting, Austria.

[41] Petti D.A., Buongiorno J., Maki J.T., Hobbins R.R., Miller G.K., 2003, Key differences in the fabrication, irradiation and high temperature accident testing of US and German TRISO coated particle fuel and their implications on fuel performance, Nuclear Engineering and Design, 222, 281-297.

[42] IAEA-TECDOC-978, 1997, Fuel performance and fission product behavior in gas cooled reactors, International Atomic Energy Agency Technical Document.

[43] Liang T.X., Zhao H.S., Tang C.H., Verfondern K., 2006, Irradiation performance and modeling of HTR-10 coated fuel particles, Nuclear Engineering and Design, 236, 1922-1927.

[44] Verfondern K., Nabielek H., 1990, The mathematical basis of the PANAMA-I code for modeling pressure vessel failure of TRISO coated particles under accident conditions, HTA-IB-09/90, KFA, Germany.

[45] Martin D.G., 2004, Some fundamental considerations pertaining to modelling the mechanical behaviour of coated fuel particles during irradiation, paper presented in Technical Meeting on Current Status and Future Prospects of Gas Cooled Reactor Fuels, IAEA, Austria.

[46] Release 11 Documentation for ANSYS.

[47] Li L., Purkiss J., Stress strain constitutive equations of concrete material at elevated temperatures, doi:10.1016/j.physletb.2003.10.071.

[48] Hidalgo M.E., 2004, Implementation of Finite element analysis into the athletic shoe design process, M.Sc. Thesis, MIT.

[49] Huebner K.H., Thornton E.A., 1982, The Finite Element Method for Engineers, John Wiley and Sons.

[50] Zienkiewicz O.C., Taylor R.L., 2000, The Finite Element Method, Volume 1 The Basis, Butterworth-Heinemann.

[51] www.wikipedia.org, the web site.

[52] Olander D.R., 1976, Fundamental aspects of reactor fuel elements, Technical Information Center, Energy Research and Development Administration.

[53] Proksch E., Strigl A., Nabielek H., 1982, Production of carbon monoxide during burnup of UO_2 kerneled HTR fuel particles, Journal of Nuclear Materials, 107, 280-285.

[54] Lindemer T.B., Pearson R.L., 1977, Kernel migration for HTGR fuels from the system Th-U-Pu-C-O-N, Journal of American Ceramic Society, 60, 1-2.

[55] Choi Y., Lee J.K., 2006, An analytical model for the amoeba effect in UO_2 fuel pellets, Journal of Nuclear Materials, 357, 213-220.

[56] Sawa K., Ueta S., 2004, Research and development on HTGR fuel in the HTTR project, Nuclear Engineering and Design, 233, 163-172.

[57] Saito S., Shiozawa S., Fukuda K., Kondo T., 1990, Safety requirements and research and development on HTTR fuel, Proceedings of a specialists meeting held in Oak Ridge, USA.

[58] Özışık M.N., 1979, Heat Conduction, John Wiley and Sons.

[59] Incropera F.P., De Witt P.P., 1990, Fundamentals of Heat and Mass Transfer, Third Edition, John Wiley and Sons.

[60] Hu S., Wang R., Gao Z., 2004, Safety Demonstration Tests on HTR-10, 2nd International Topical Meeting on High Temperature Reactor Technology, China.

[61] Duderstadt J.J., Hamilton L.J., 1976, Nuclear Reactor Analysis, John Wiley and Sons.

[62] Zuying G., Lei S., 2002, Thermal hydraulic transient analysis of the HTR-10, Nuclear Engineering and Design, 218, 65-80.

[63] Hu S., Wang R., Gao Z., 2006, Transient tests on blower trip and rod removal at the HTR-10, Nuclear Engineering and Design, 236, 677-680.

[64] Cioni O., Marchand M., Geffraye G., Ducros F., 2006, 3D thermal-hydraulic calculations of a modular block-type HTR core, Nuclear Engineering and Design, 236, 565-573.

[65] Barkanov E., 2001, Introduction to the Finite Element Method, Lecture Notes, Riga Technical University.

[66] Nabielek H., personal communication.

Appendix A

CRP-6 Study

The finite element model of the coated fuel particle developed in this work is benchmarked with the International Atomic Energy Agency (IAEA) Coordinated Research Project-6 (CRP-6) study. USA, UK, France, Russia, South Africa, China, Japan and Korea are among the countries participated in CRP-6 TRISO Coated Fuel Performance Benchmark Cases. The benchmark is set up in five parts. First part involves simple analytical cases to test thermo-mechanical behavior. Pyrocarbon layer behavior is tested in the second part. The third part presents a single particle with more complexity added in terms of creep and swelling/shrinkage. In the fourth part, more complicated benchmarks of actual experiments are modelled. The fifth part includes calculations regarding experiments that are planned. The benchmark calculations are performed for the following cases:

Case 1 Elastic SiC

Case 2 Simple BISO

Case 3 IPyC/SiC Composite without fluence

Case 4a IPyC/SiC Composite with no creep and constant swelling/shrinkage

Case 4b IPyC/SiC Composite with constant creep and no swelling/shrinkage

Case 4c IPyC/SiC Composite with constant creep and constant swelling/shrinkage

Case 4d IPyC/SiC Composite with constant creep and fluence-dependent swelling/shrinkage

Case 5 TRISO, 350 μm kernel

Case 6 TRISO, 500 μm kernel

Case 7 TRISO, High BAF

Case 8 TRISO, Cyclic temperature history

Case 9 HRB-22 Experiment (past irradiation)

Case 10 HFR-K3 B/2 Experiment (past irradiation)

Case 11 HFR-P4 3 Experiment (past irradiation)

Case 12 NPR-1A 5 Experiment (past irradiation)

Case 13 HFR EU-1 Experiment (future irradiation)

Case 14 HFR EU-2 Experiment (future irradiation)

Explanation, properties, analysis and results comparison with those of the other countries are presented in the following subsections.

A.1 General Approach

CRP-6 study is performed to verify the finite element model of the coated fuel particle. The study involves cases starting from the simple one-layer particle to a real TRISO particle. As the number of layers increases, the particle also faces different loads that simulate different irradiation conditions.

Steady state calculations are performed for Cases 1 to 4c, where internal pressures, temperature and swelling/shrinkage rate do not change with time. For Cases 4d to 14, transient calculations are performed.

Cases 1 to 8 assume constant pressure inside the IPyC layer. For Cases 9 to 14, gas pressure inside the IPyC is calculated and presented as a comparison metric.

Tangential and radial stress as a function of fast neutron fluence are other items of the comparison metric for analyzing the performance of different coated fuel particle models. Also, for Cases 9 to 14, particle failure probability is calculated and compared with different models.

Individual layer failure probabilities are calculated for the relevant cases. One approach for prediciting the particle failure probability is assuming the SiC as the principal barrier and considering its failure probability as the representative of the particle failure probability [43, 44]. This approach is employed for the analysis. Since tension (not compression) of the SiC is the main contributor to the failure, tension values of the tangential stress in the SiC layer is used in the probability calculations. Weibull statistics is employed in probability calculations, the details of which is presented in Appendix C.

Main approaches and assumptions for the CRP-6 study are as follows:

- Under irradiation conditions or reactor operation, the particle is under pressure

load from fission gases and CO formed outside the kernel. Ambient pressure is assumed outside the OPyC layer. Details on pressure calculation are presented in Appendix B.

- Under irradiation, PyC shrinks in both radial and tangential directions. The behavior of PyC in radial and tangential directions for a sample case is presented in Figure A.1. Different swelling/shrinkage strain rate correlations generally show the same behavior. At modest fluences depending on the density, temperature and anisotropy of the material, it begins to swell in the radial direction and continues to shrink in the tangential direction. This behavior puts the PyC layers into tension in the tangential direction. At longer irradiation times, irradiation-induced creep works to relieve the tensile stress on the PyC layers. Creep is also modelled in the present study.

- The anisotropy of PyC layers affects swelling as a function of neutron fluence. The IPyC and OPyC layers behave differently in radial and tangential directions as a result of this anisotropy, which is represented by the Bacon Anisotropy Factor (BAF). Anisotropy of the PyC layers is taken into consideration starting from Case 4a. Radial and tangential swelling/shrinkage rates as a function of fast neutron fluence are presented in this chapter. These equations change according to the initial BAF of the case and also depend on material properties and irradiation conditions.

- Thermal expansion is another load factor affecting the SiC and PyC layers that is taken into consideration.

A.2 Individual Cases

Case 1 Elastic SiC

This case involves a particle with a kernel diameter of 500 μm and a buffer thickness of 100 μm. The particle has only one coating layer, the SiC. Diagrammatic

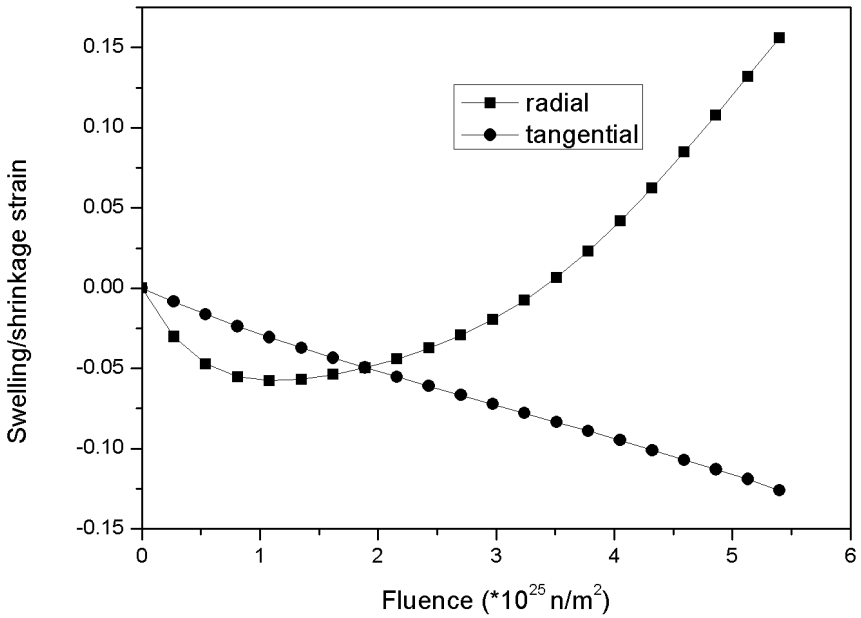

Figure A.1: Swelling/shrinkage behavior for a sample case

representation of Case 1 is shown in Figure A.2. Fuel characteristics and material properties for Case 1 are presented in Tables A.1 and A.2 [25].

ANSYS model of Case 1 involves a two dimensional axisymmetric model consisting of only the SiC layer with $\frac{1}{2}$ symmetry. Since free volumes of the kernel and buffer determine the pressure on layers, only the SiC layer is present in the model with constant internal and external pressures. The particle is assumed only under the pressure load of 25 MPa and an ambient pressure of 0.1 MPa. Figure A.3 presents the ANSYS finite element model of Case 1. Maximum tangential stress on the SiC layer is calculated as 125 MPa. This result is consistent with those of the other countries [40]. Case 1 results of participating countries are presented in Figure A.4.

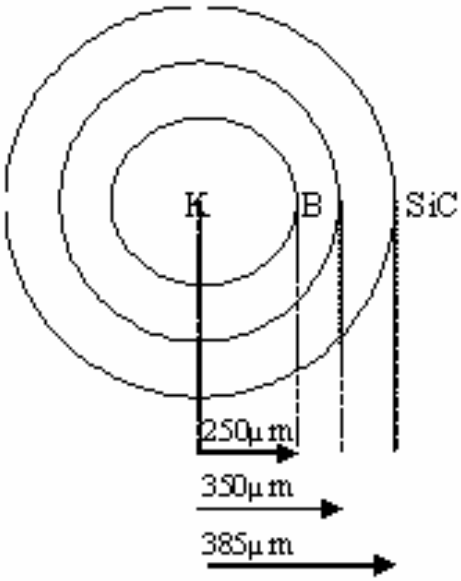

Figure A.2: Diagrammatic representation of Case 1

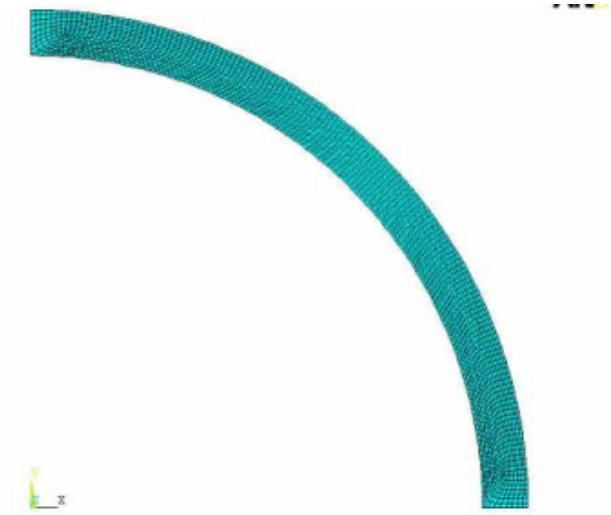

Figure A.3: Finite element model of Case 1

Table A.1: Fuel characteristics for Case 1

Oxygen to uranium ratio	2
U-235 enrichment (weight %)	10
Kernel diameter (μm)	500
Buffer thickness (μm)	100
SiC thickness (μm)	35
Kernel density (Mg/m^3)	10.8
Buffer density (Mg/m^3)	0.95

Table A.2: Material properties for Case 1

SiC density (Mg/m^3)	3.20
SiC modulus of elasticity (MPa)	3.70×10^5
SiC Poisson's ratio	0.13
SiC coefficient of thermal expansion (K^{-1})	4.9×10^{-6}

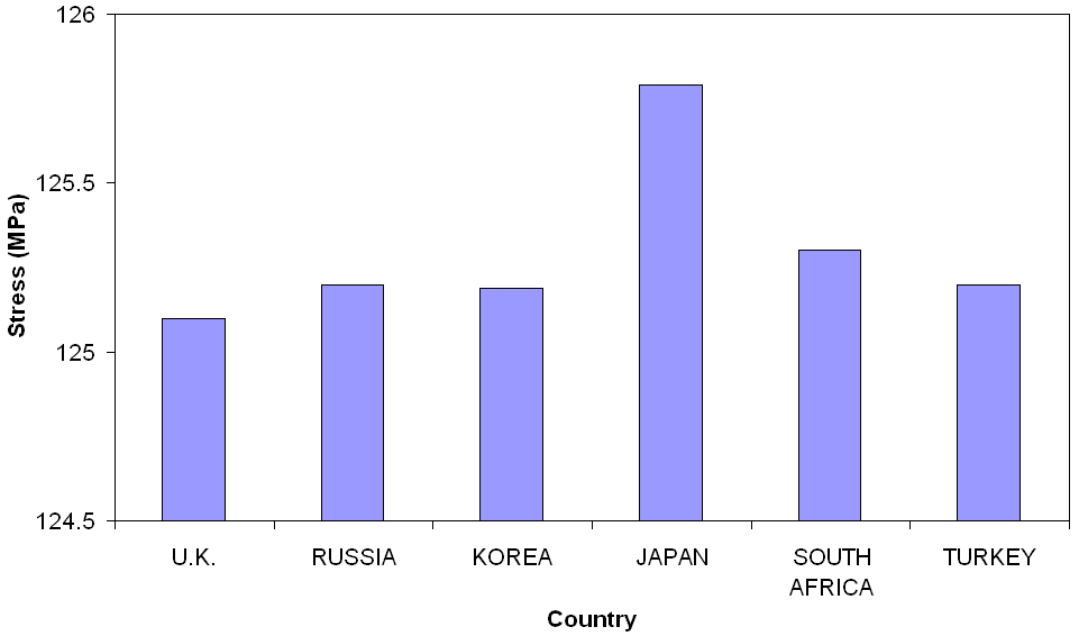

Figure A.4: Case 1 results of CRP-6 participating countries

Case 2 Simple BISO

This case involves a particle with kernel diameter of 500 μm and a buffer thickness of 100 μm. The particle has only one coating layer, the IPyC, which is 90 μm thick. Diagrammatic representation of Case 2 is shown in Figure A.5.

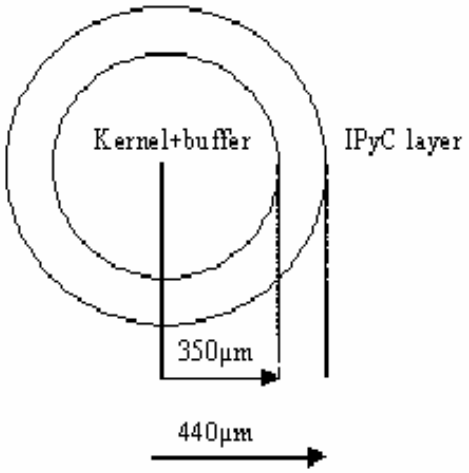

Figure A.5: Diagrammatic representation of Case 2

Table A.3: Fuel characteristics for Case 2

Oxygen to uranium ratio	2
U-235 enrichment (weight %)	10
Kernel diameter (μm)	500
Buffer thickness (μm)	100
IPyC thickness (μm)	90
Kernel density (Mg/m^3)	10.8
Buffer density (Mg/m^3)	0.95

Table A.4: Material properties for Case 2

IPyC density (Mg/m^3)	1.90
IPyC modulus of elasticity (MPa)	3.96×10^4
IPyC Poisson's ratio	0.33
IPyC coefficient of thermal expansion (K^{-1})	5.5×10^{-6}

Fuel characteristics and material properties for Case 2 are presented in Tables A.3 and A.4 [25]. The finite element model of Case 2 is a two dimensional axisym-

metric model consisting of only the IPyC layer with $\frac{1}{2}$ symmetry. The coating layer is assumed to be only under the pressure load of 25 MPa and an ambient pressure of 0.1 MPa. The finite element model is the same as that of the Case 1, except that layer properties and dimensions are those of the IPyC. Maximum tangential stress of 50.2 MPa is calculated on the IPyC layer.

This result is consistent with those of the other countries. Case 2 results of participating countries are presented in Figure A.6 [40].

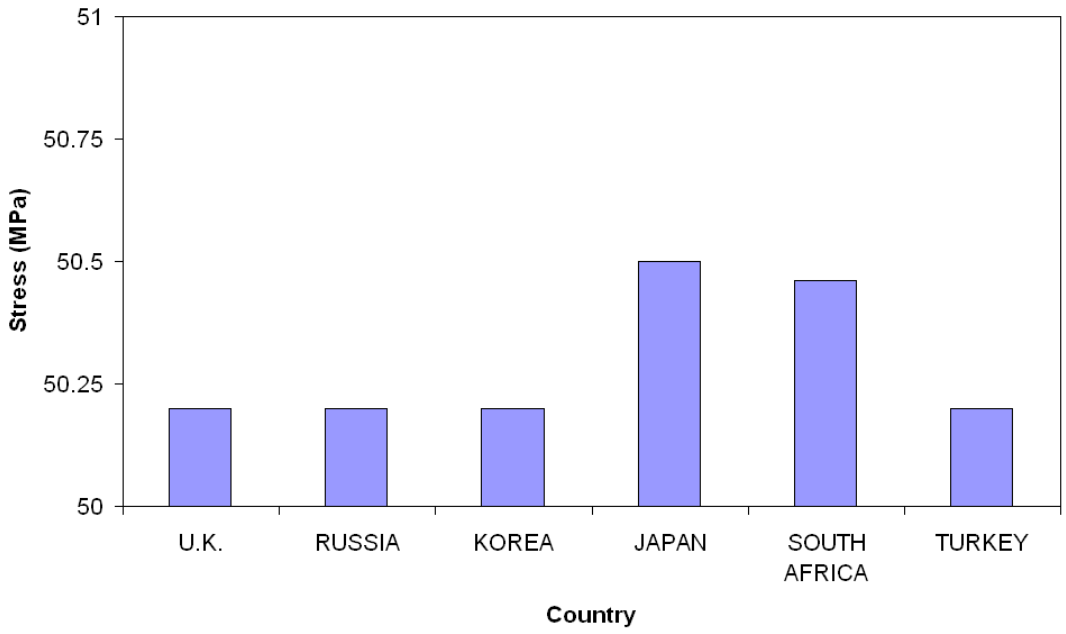

Figure A.6: Case 2 results of CRP-6 participating countries

Case 3 IPyC/SiC Composite without Fluence

This case involves a particle with kernel diameter of 500 μm and a buffer thickness of 100 μm. The particle has two coating layers: the IPyC, which is 40 μm thick, and the SiC, which is 35 μm thick. Fuel characteristics and material properties for Case 3 are presented in Tables A.1, A.2, A.3 and A.4 [25].

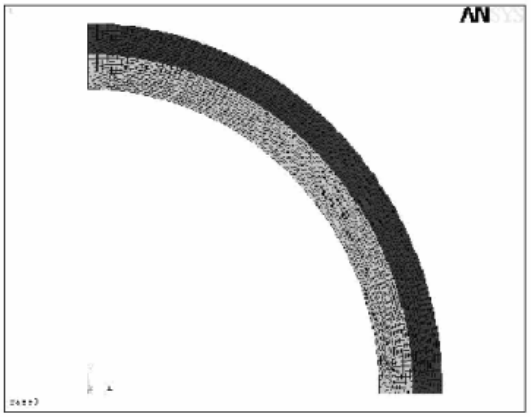

Figure A.7: Finite element model of Case 3

Finite element model of Case 3 involves a two dimensional axisymmetric model consisting of the IPyC and SiC layers with $\frac{1}{2}$ symmetry. The particle is assumed only under the pressure load of 25 MPa and an ambient pressure of 0.1 MPa. Figure A.7 presents the finite element model of Case 3. Maximum tangential stress on the IPyC and SiC layers are calculated as 8.7 MPa and 104.2 MPa, respectively. These results are consistent with those of the other countries [40]. Case 3 results of the participating countries are presented in Figures A.8 and A.9.

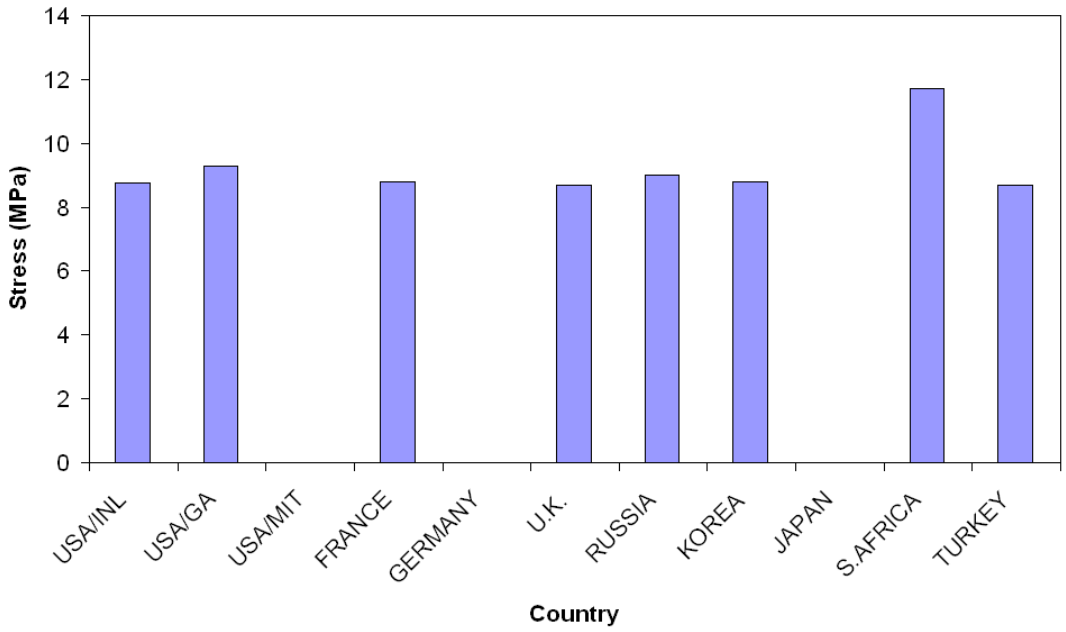

Figure A.8: Case 3 results of participating countries, maximum stress value on IPyC

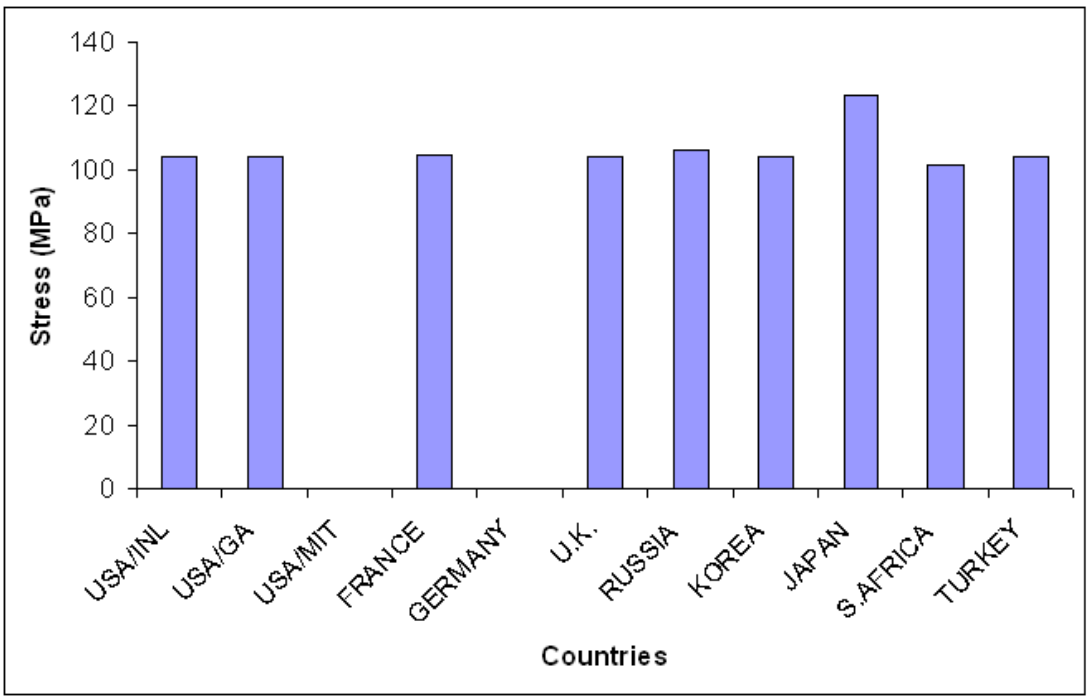

Figure A.9: Case 3 results of participating countries, maximum stress value on SiC

Case 4a IPyC/SiC Composite with No Creep and Constant Swelling/Shrinkage

Case 4a through 4d have the same particle as in Case 3, except that it experiences a fast neutron fluence with the IPyC layer allowed to swell/shrink. The particle is assumed under the pressure load of 25 MPa and an ambient pressure of 0.1 MPa. Cases 4a, 4b, 4c and 4d include modelling of the same particle with different combinations of creep and swelling/shrinkage effects imposed. Table A.5 presents the fuel characteristics, Table A.6 presents the irradiation conditions and Table A.7 presents the material properties for Cases 4a through 4d [25]. Finite element model of Case 4a through 4d is the same as Case 3 except for the swelling/shrinkage strain rate added.

Table A.5: Fuel characteristics for Cases 4a-4d

Parameter	Case 4a	Case 4b	Case 4c	Case 4d
Oxygen to uranium ratio	2	2	2	2
Carbon to uranium ratio	0	0	0	0
U-235 enrichment (weight $\%$)	10	10	10	10
Kernel diameter (μm)	500	500	500	500
Buffer thickness (μm)	100	100	100	100
IPyC thickness (μm)	40	40	40	40
SiC thickness (μm)	35	35	35	35
Kernel density (Mg/m^3)	10.8	10.8	10.8	10.8
Buffer density (Mg/m^3)	0.95	0.95	0.95	0.95
IPyC density (Mg/m^3)	1.90	1.90	1.90	1.90
SiC density (Mg/m^3)	3.2	3.2	3.2	3.2
IPyC BAF	1.03	1.03	1.03	1.03

Table A.6: Irradiation conditions for Cases 4a-4d

Parameter	Case 4a	Case 4b	Case 4c	Case 4d
End of life burnup ($\%$FIMA)	0	0	0	0
End of life fluence (10^{25} n/m^2, E $>$ 0.18 MeV)	3	3	3	3
Constant temperature (K)	1273	1273	1273	1273
Constant internal pressure (MPa)	25	25	25	25
Ambient pressure (MPa)	0.1	0.1	0.1	0.1

Table A.7: Material properties for Cases 4a-4d

Parameter	Case 4a	Case 4b	Case 4c	Case 4d
PyC modulus of elasticity (MPa)	3.96×10^4	3.96×10^4	3.96×10^4	3.96×10^4
PyC Poisson's ratio	0.33	0.33	0.33	0.33
PyC Poisson's ratio in creep	None	0.5	0.5	0.5
PyC coefficient of thermal expansion (K^{-1})	5.5×10^{-6}	5.5×10^{-6}	5.5×10^{-6}	5.5×10^{-6}
PyC creep coefficient ((MPa–10^{25} n/m^2)$^{-1}$, E $>$ 0.18 MeV)	None	2.71×10^{-4}	2.71×10^{-4}	2.71×10^{-4}
PyC swelling/shrinkage strain rate ((ΔL/L)/10^{25} n/m^2, E $>$ 0.18 MeV)	-0.005 (isotropic)	None	-0.005 (isotropic)	Eq. A.1, A.2
SiC modulus of elasticity (MPa)	3.70×10^5	3.70×10^5	3.70×10^5	3.70×10^5
SiC Poisson's ratio	0.13	0.13	0.13	0.13
SiC coefficient of thermal expansion (K^{-1})	4.9×10^{-6}	4.9×10^{-6}	4.9×10^{-6}	4.9×10^{-6}

A constant shrinkage strain rate is imposed in Case 4a. The comparison metric for CRP-6 in Case 4a consists of the maximum radial stress between IPyC and SiC and the maximum tangential SiC stress as a function of fast neutron fluence. The change of the radial stress between the IPyC and SiC layers with fast neutron fluence is presented in Figure A.10. The variations of the maximum tangential stress for the IPyC and SiC layers with fast neutron fluence are presented in Figures A.11 and A.12, respectively. The results are consistent with those of the other countries [40]. Case 4a results of the participating countries are presented in Figures A.13, A.14 and A.15.

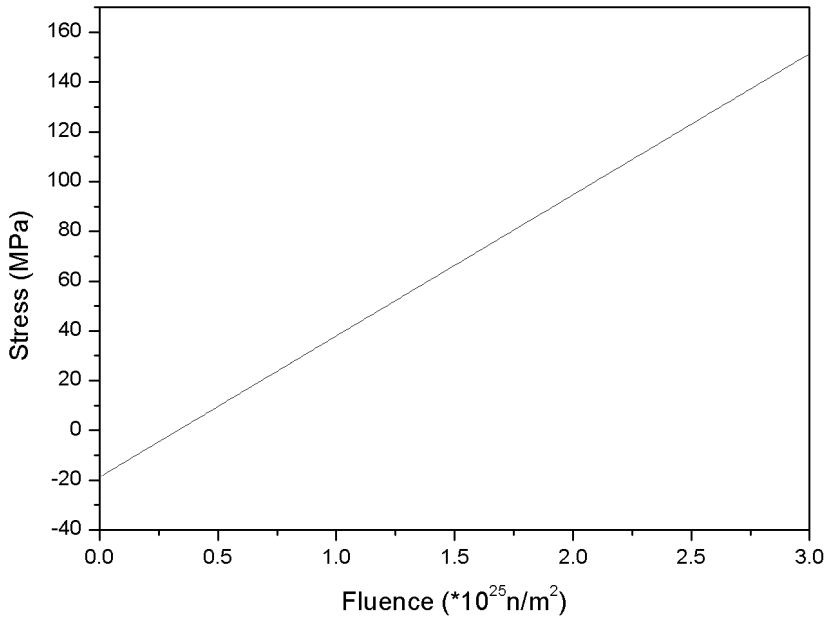

Figure A.10: Radial stress between IPyC and SiC layers for Case 4a

As can be seen from the figures A.11 and A.12, initial values of the tangential stresses are the same as those obtained in Case 3. As burnup progresses the IPyC shrinks but presence of the SiC limits the extent of this shrinkage. Therefore, tensile stress builds up on the IPyC layer, as shown in Figure A.11. By contrast, the shrinking IPyC layer pulls in the SiC layer and tangential stress on this layer becomes increasingly compressive as burnup progresses (see Fig. A.12). Thus, presence of a shrinking

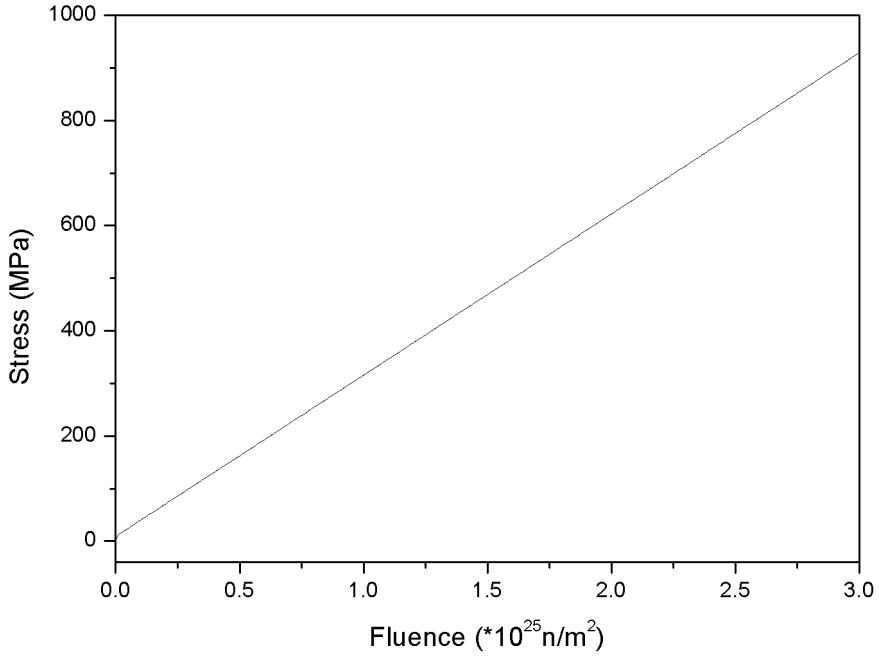

Figure A.11: Tangential stress on IPyC layer for Case 4a

IPyC layer keeps the SiC layer under compression for the duration of irradiation. This result ignores the pressure build-up due to fission product gases and CO inside the particle.

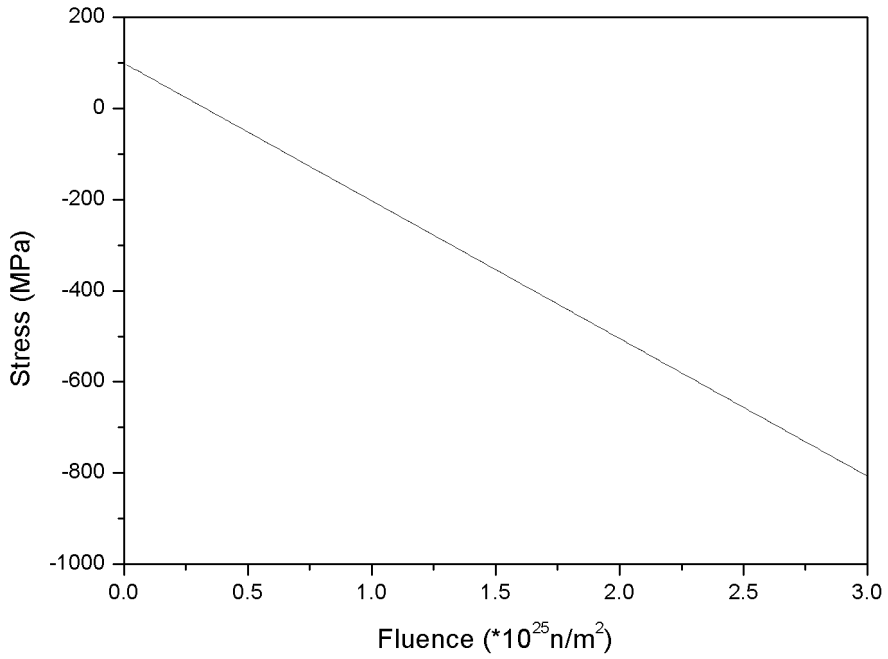

Figure A.12: Tangential stress on SiC layer for Case 4a

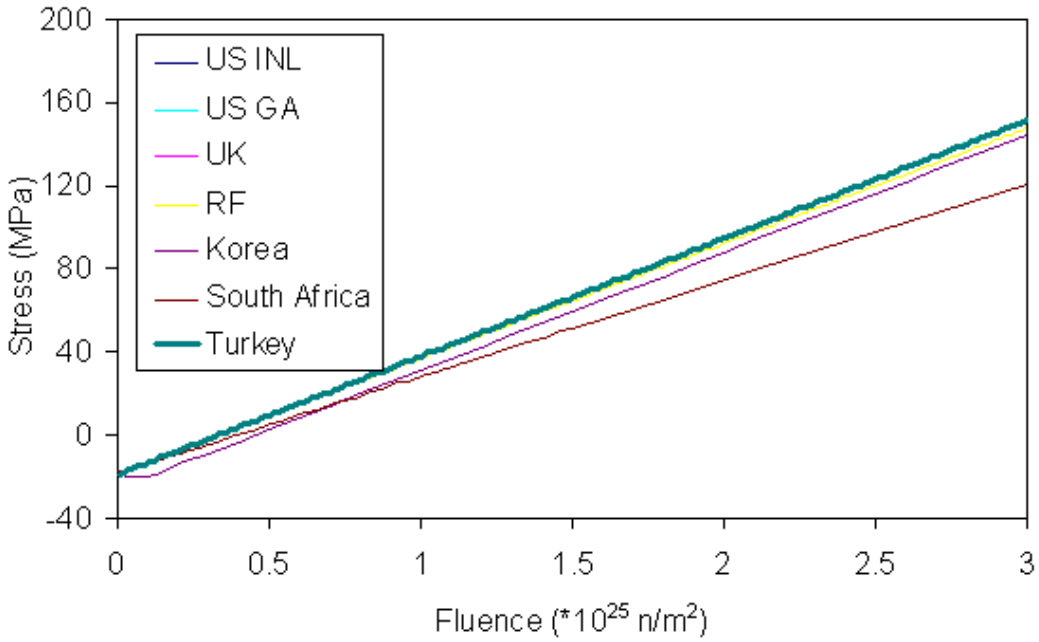

Figure A.13: Case 4a results of participating countries, radial stress between IPyC and SiC layers

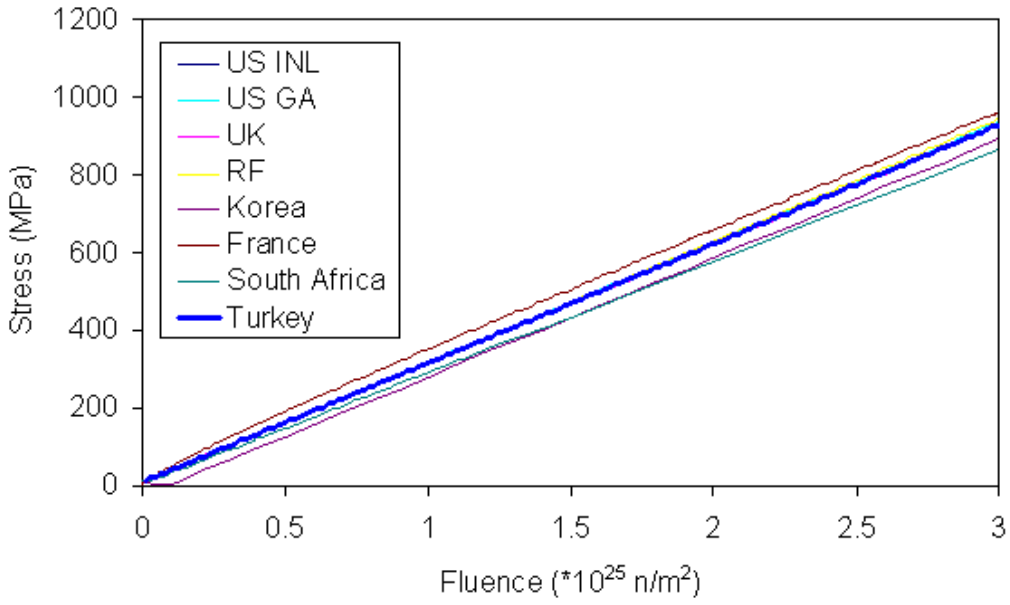

Figure A.14: Case 4a results of participating countries, tangential stress on IPyC layer

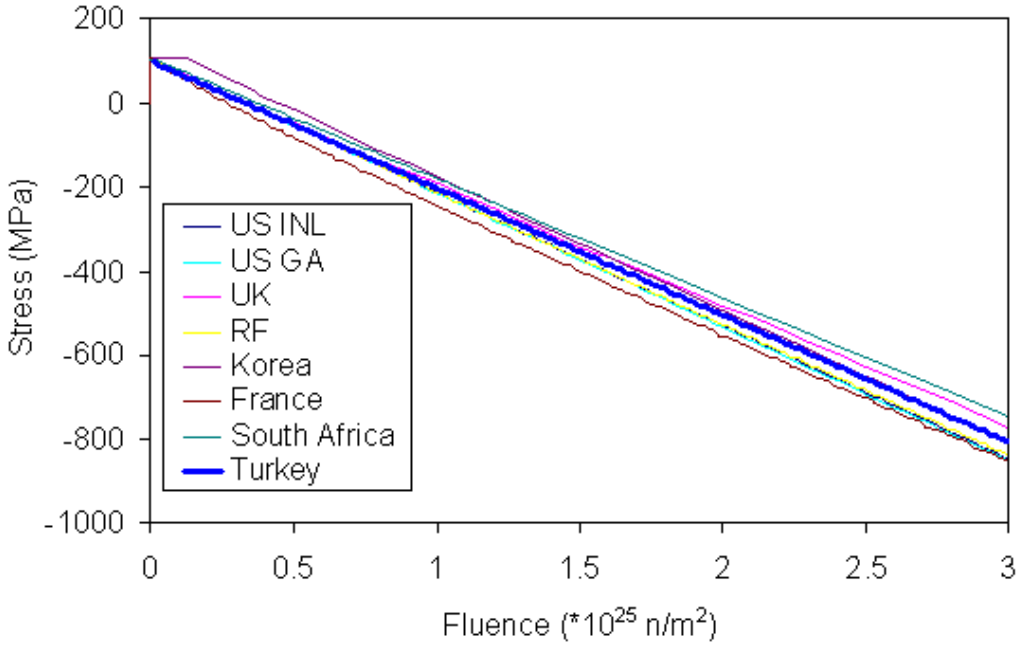

Figure A.15: Case 4a results of participating countries, tangential stress on SiC layer

Case 4b IPyC/SiC Composite with Constant Creep and No Swelling/Shrinkage

Case 4b has the same particle as in Case 3, except that it experiences a fast neutron fluence with the IPyC layer allowed to creep. A constant internal pressure of 25 MPa is assumed. The change of the radial stress between the IPyC and SiC layers with fast neutron fluence is presented in Figure A.16. The variations of the maximum tangential stress for the IPyC and SiC layers with fast neutron fluence are presented in Figures A.17 and A.18, respectively. The results are consistent with those of the other countries [40]. Case 4b results of the participating countries are presented in Figures A.19, A.20 and A.21.

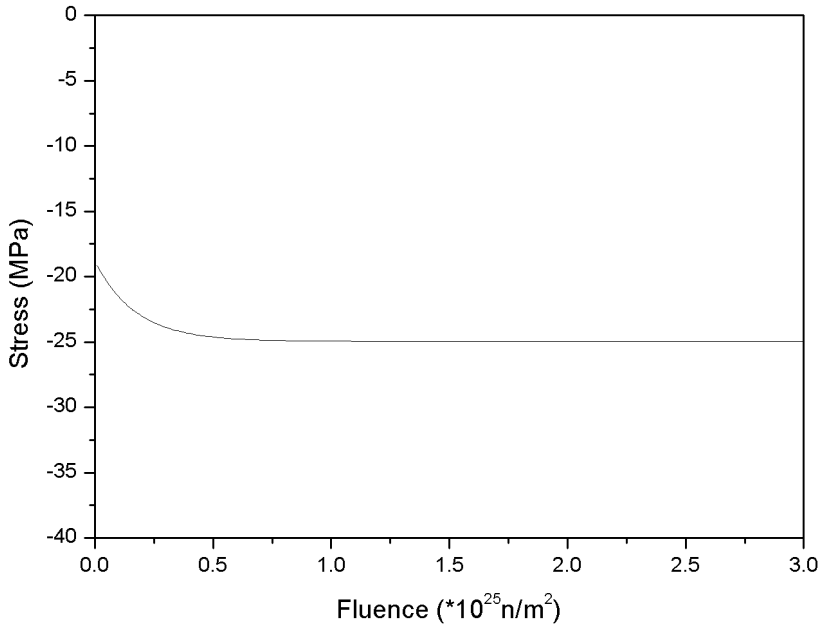

Figure A.16: Radial stress between IPyC and SiC layers for Case 4b

As can be seen from the figures A.17 and A.18, initial values of the tangential stresses are the same as those obtained in Case 4a. As burnup progresses the IPyC relaxes due to radiation-induced creep. Therefore, compressive stress builds up on the

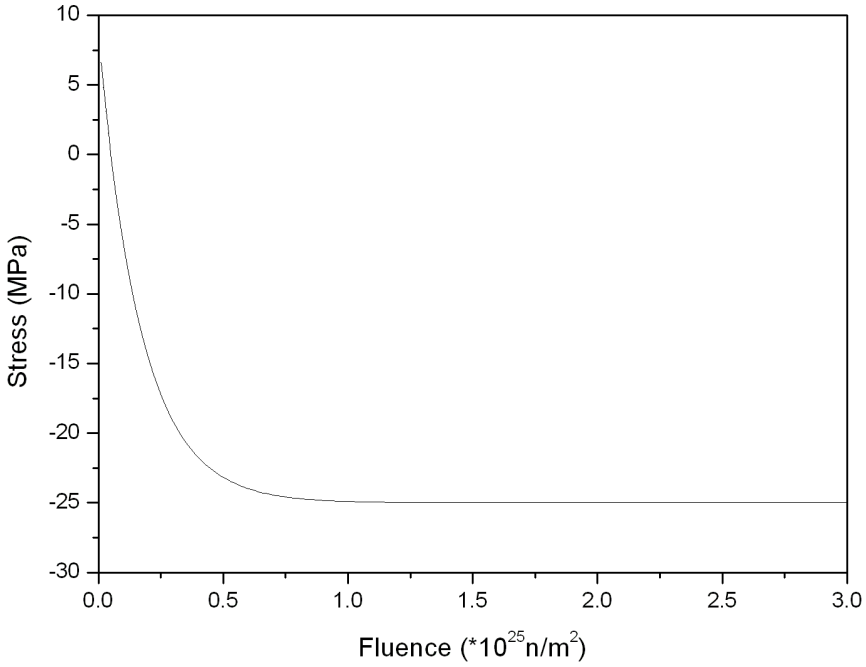

Figure A.17: Tangential stress on IPyC layer for Case 4b

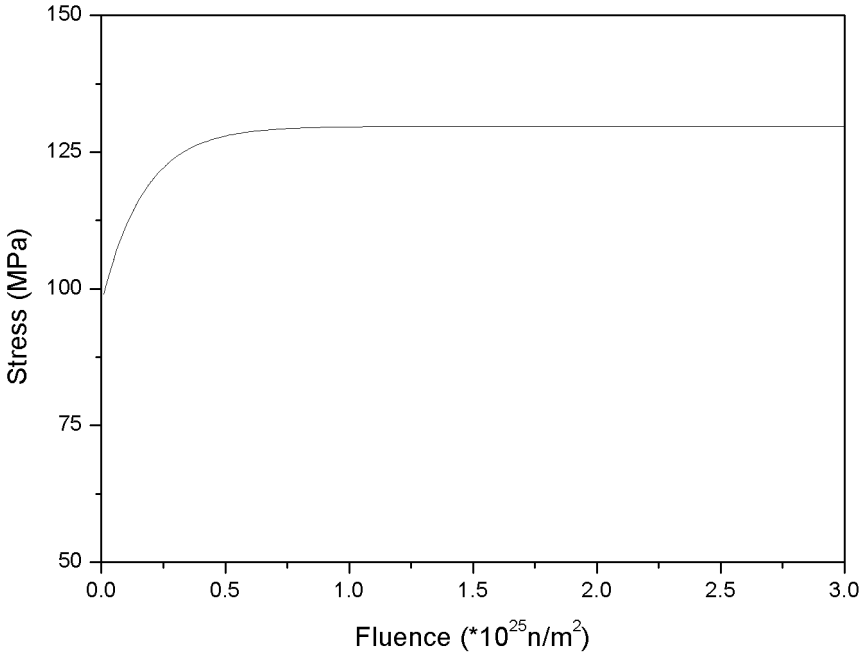

Figure A.18: Tangential stress on SiC layer for Case 4b

IPyC layer to a certain value, as shown in Figure A.17. By contrast, the relaxing IPyC layer pushes the SiC layer out and tangential tensile stress on this layer first increases and then levels off as burnup progresses (see Fig. A.18), following the relaxation behavior of the IPyC layer.

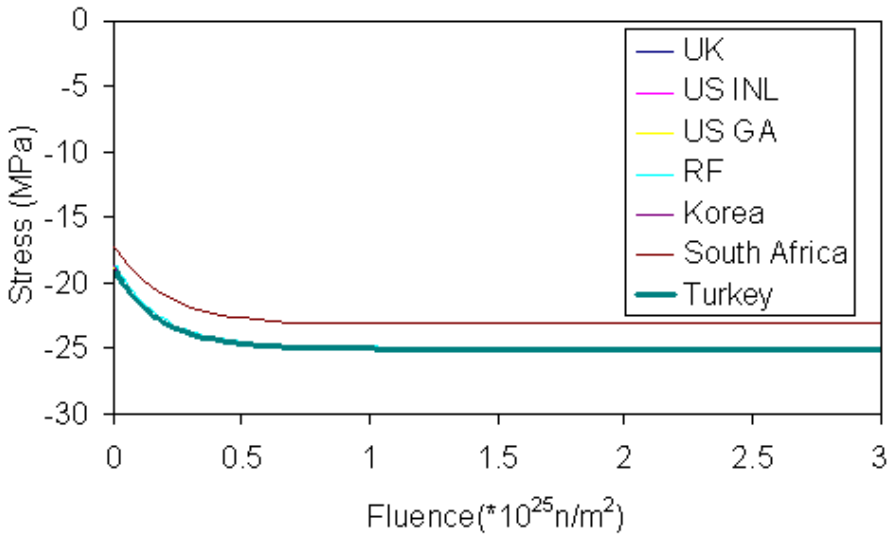

Figure A.19: Case 4b results of participating countries, radial stress between IPyC and SiC layers

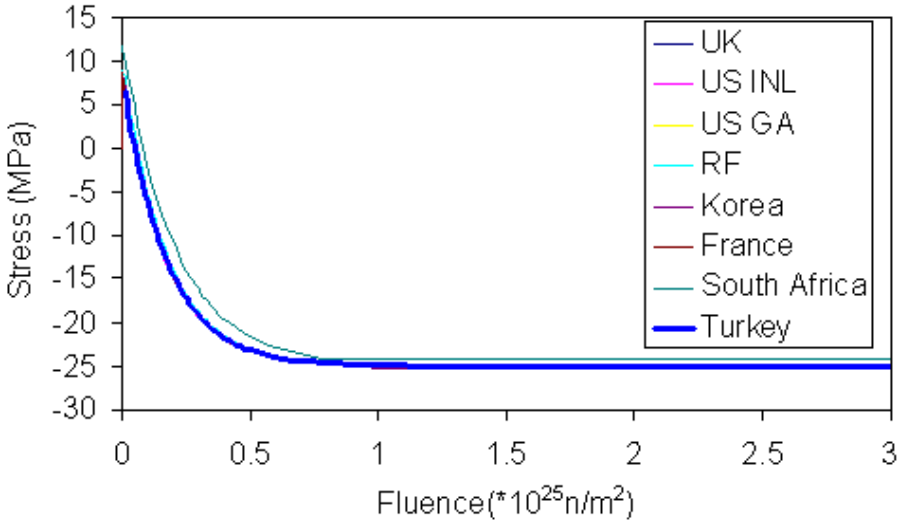

Figure A.20: Case 4b results of participating countries, tangential stress on IPyC layer

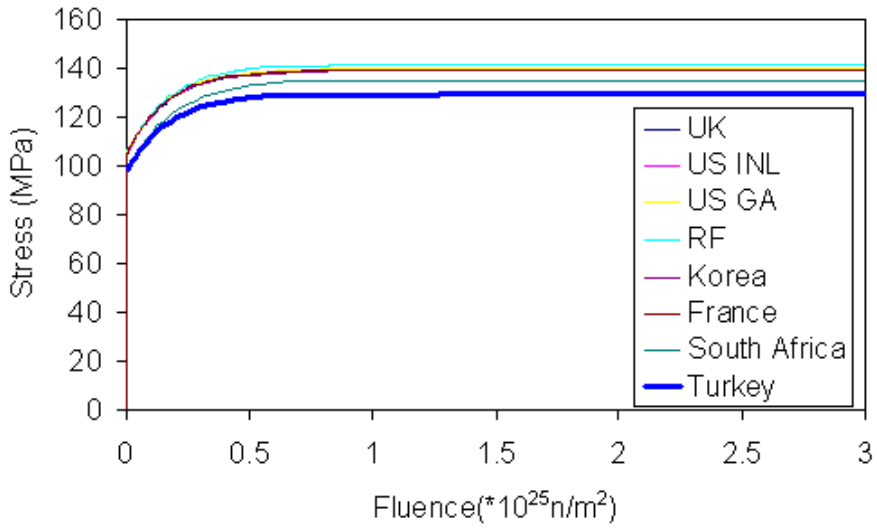

Figure A.21: Case 4b results of participating countries, tangential stress on SiC layer

Case 4c IPyC/SiC Composite with Constant Creep and Constant Swelling/Shrinkage

Case 4c has the same particle as in Case 3, except that it experiences a fast neutron fluence with the IPyC layer allowed to creep and shrink at constant rates. Shrinkage in Case 4c is isotropic. A constant internal pressure of 25 MPa is assumed. The change of the radial stress between the IPyC and SiC layers with fast neutron fluence is presented in Figure A.22. The variations of the maximum tangential stress for the IPyC and SiC layers with fast neutron fluence are presented in Figures A.23 and A.24, respectively. The results are consistent with those of the other countries [40]. Case 4c results of the participating countries are presented in Figures A.25, A.26 and A.27.

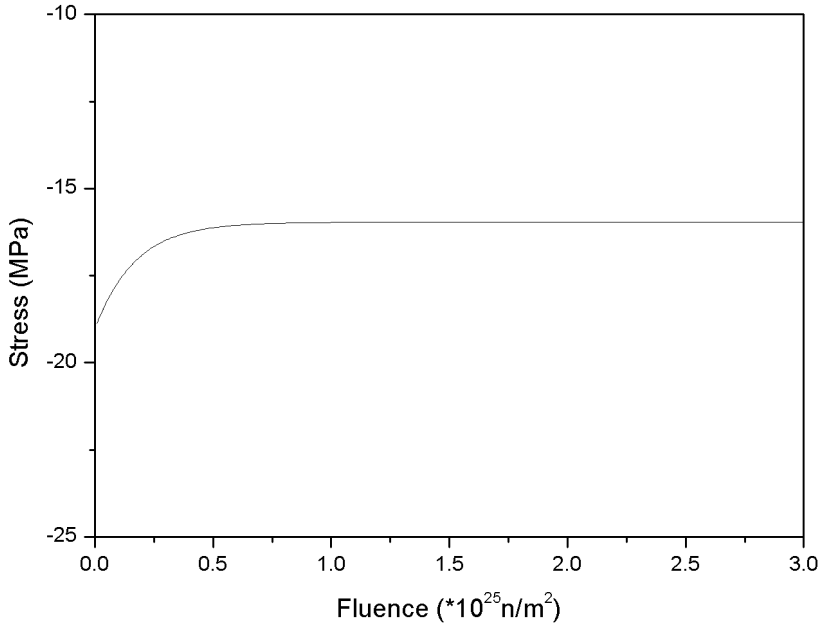

Figure A.22: Radial stress between IPyC and SiC layers for Case 4c

As burnup progresses the IPyC shrinks to the extent permitted by relaxation due to creep. Presence of the SiC is also effective in this limitation. Therefore, a limited

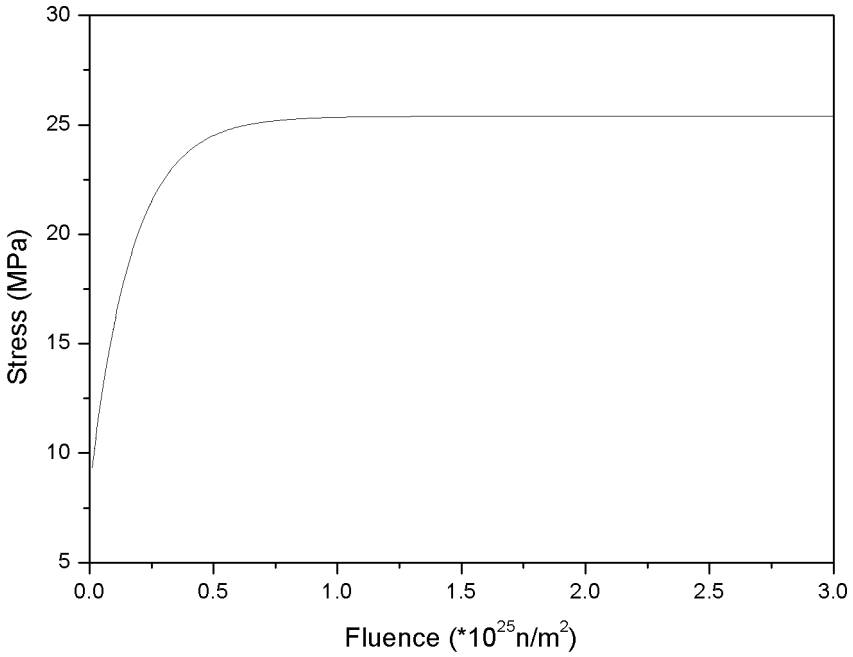

Figure A.23: Tangential stress on IPyC layer for Case 4c

tensile stress build-up is observed on the IPyC layer, as shown in Figure A.23. Tensile stress on the SiC layer is reduced only slightly by the combined effect of shrinkage and creep of the IPyC layer (see Fig. A.24). Stresses on each layer remain almost constant throughout most of the irradiation period.

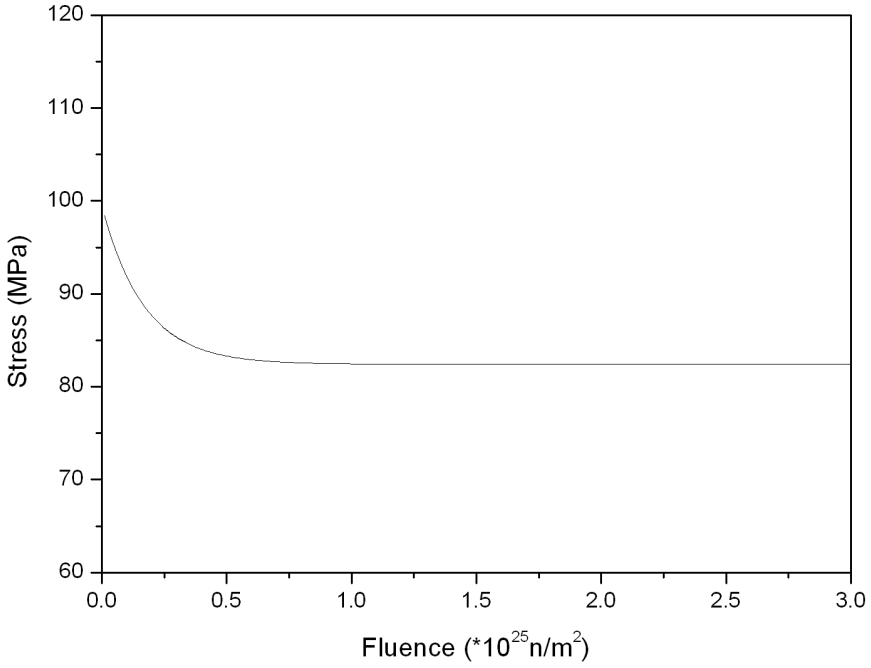

Figure A.24: Tangential stress on SiC layer for Case 4c

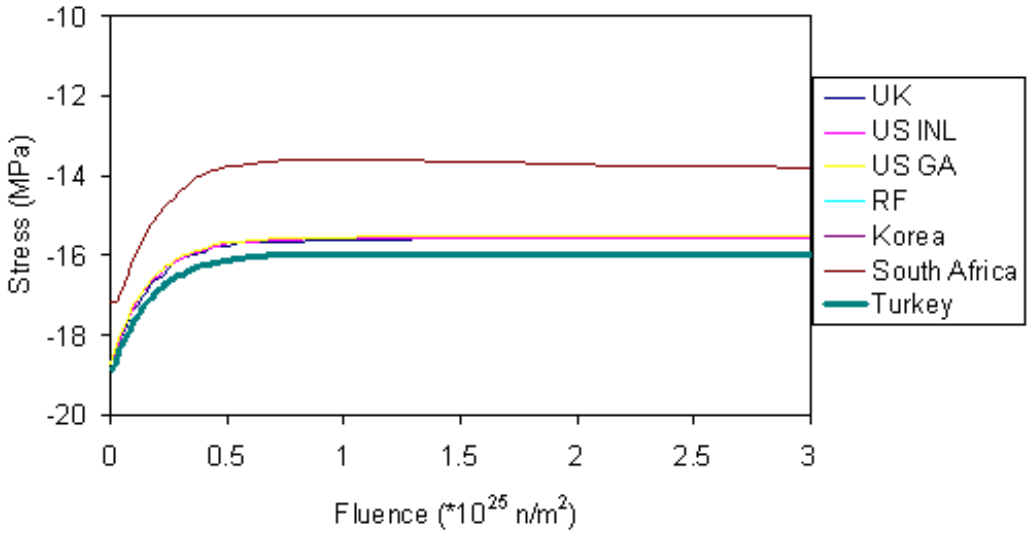

Figure A.25: Case 4c results of participating countries, radial stress between IPyC and SiC layers

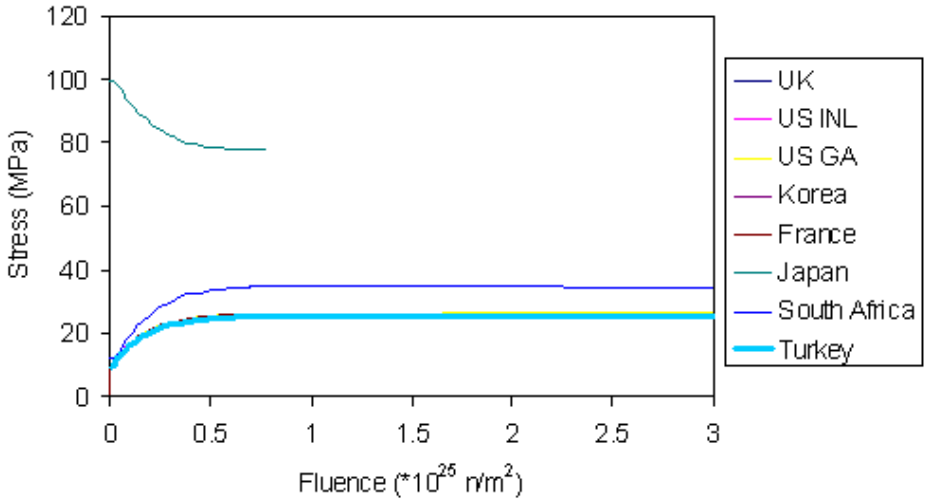

Figure A.26: Case 4c results of participating countries, tangential stress on IPyC layer

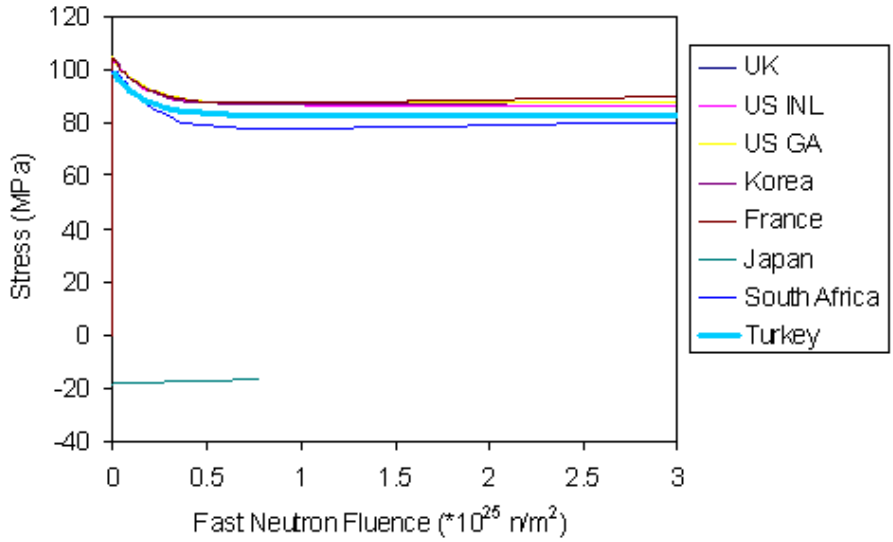

Figure A.27: Case 4c results of participating countries, tangential stress on SiC layer

Case 4d IPyC/SiC Composite with Constant Creep and Fluence-Dependent Swelling/Shrinkage

Case 4d has the same particle as in Case 3, except that it experiences a fast neutron fluence with the IPyC layer shrinking/swelling at a variable rate. A constant internal pressure of 25 MPa is assumed. PyC swelling/shrinkage strain rate is given as a function of fast neutron fluence, as represented by the correlation (a), which is given in equations A.1 and A.2. The change of the radial stress between the IPyC and SiC layers with fast neutron fluence is presented in Figure A.28. The variations of the maximum tangential stress for the IPyC and SiC layers with fast neutron fluence are presented in Figures A.29 and A.30, respectively. The results are consistent with those of the other countries [40]. Case 4d results of the participating countries are presented in Figures A.31, A.32 and A.33.

$$\text{PyC radial swelling/shrinkage rate}[(\Delta L/L)/10^{25}\ n/m^2] = \tag{A.1}$$
$$1.36334 \times 10^{-3}x^3 - 7.77024 \times 10^{-3}x^2 + 2.00861 \times 10^{-2}x - 2.22642 \times 10^{-2}$$

$$\text{PyC tangential swelling/shrinkage rate}[(\Delta L/L)/10^{25}\ n/m^2] = \tag{A.2}$$
$$-3.53804 \times 10^{-4}x^3 + 1.69251 \times 10^{-3}x^2 + 2.63307 \times 10^{-3}x - 1.91253 \times 10^{-2}$$

where x is the fast neutron fluence in units of $10^{25}\ n/m^2$.

As can be seen from the figures A.29 and A.30, the IPyC layer shrinks rapidly at the beginning, then relaxes due to creep. This reduces the tensile stress on the SiC layer and even converts to compression in a short time. The compressive stress on the SiC layer turns to tension again and the tensile stress increases with increasing burnup.

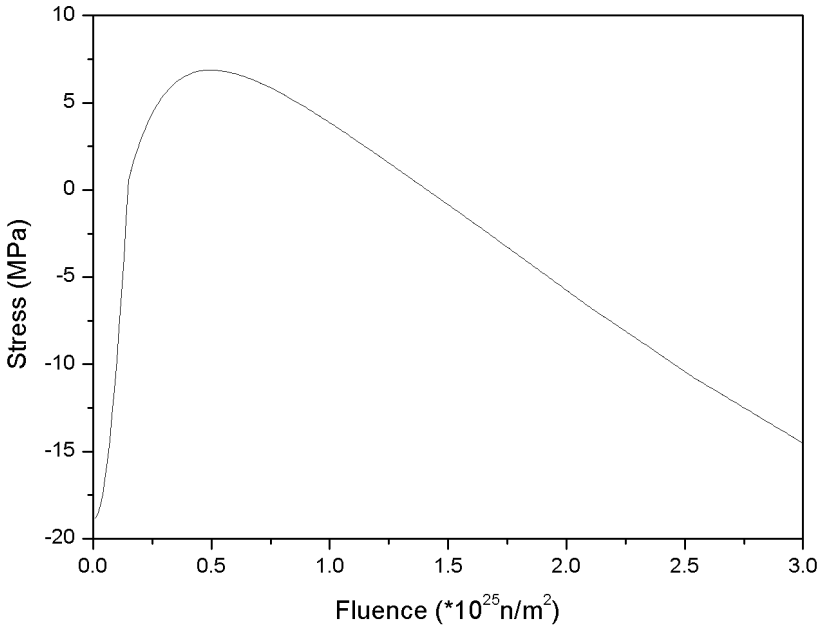

Figure A.28: Radial stress between IPyC and SiC layers for Case 4d

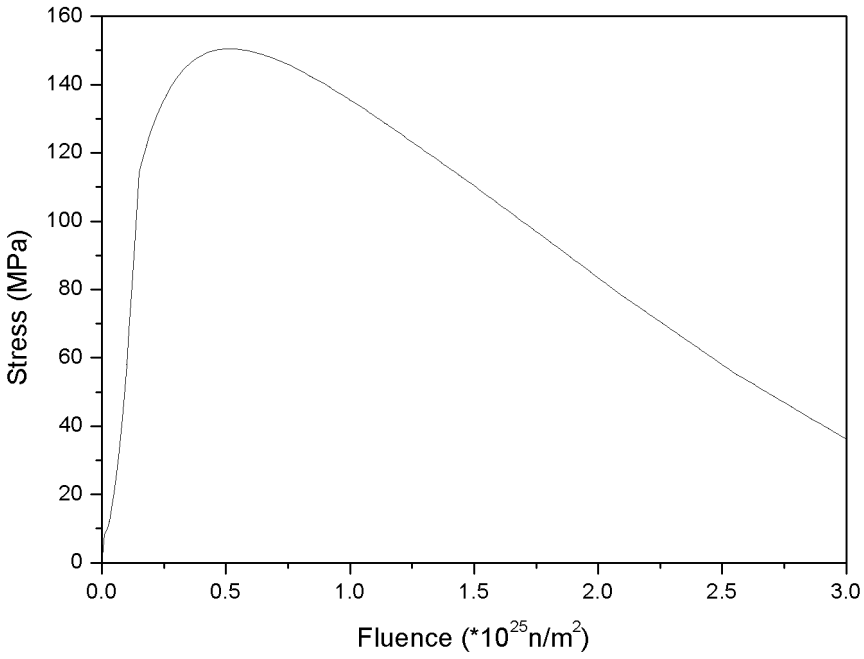

Figure A.29: Tangential stress on IPyC layer for Case 4d

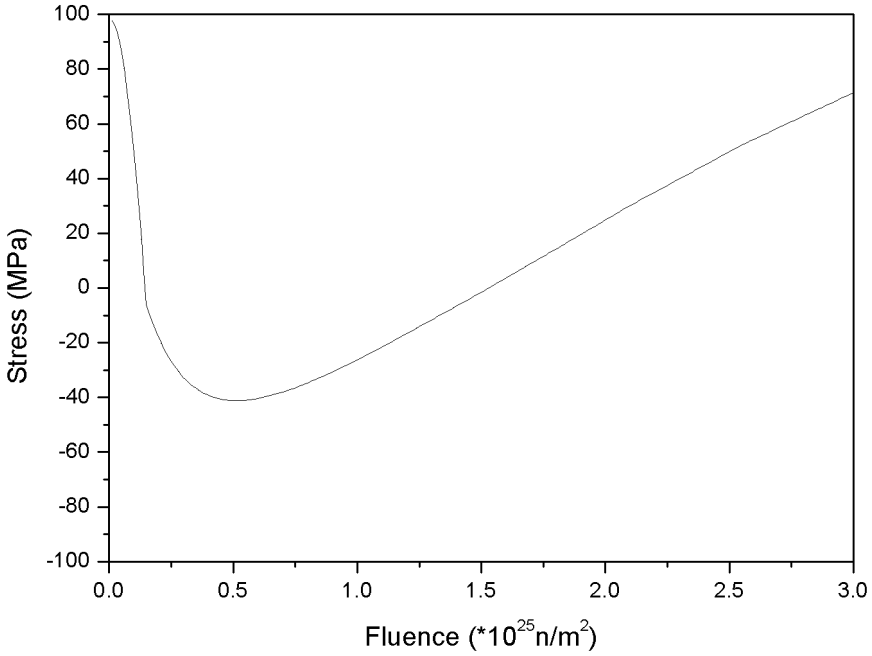

Figure A.30: Tangential stress on SiC layer for Case 4d

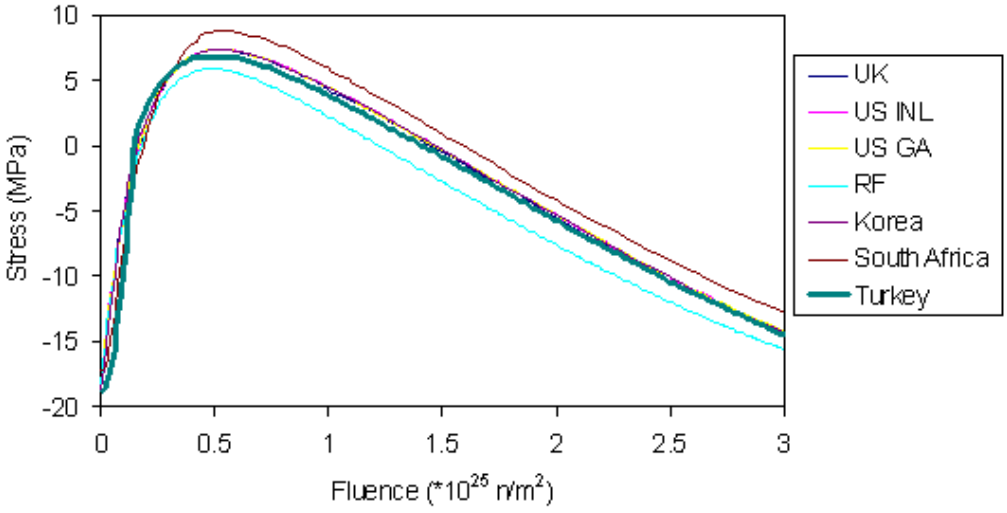

Figure A.31: Case 4d results of participating countries, radial stress between IPyC and SiC layers

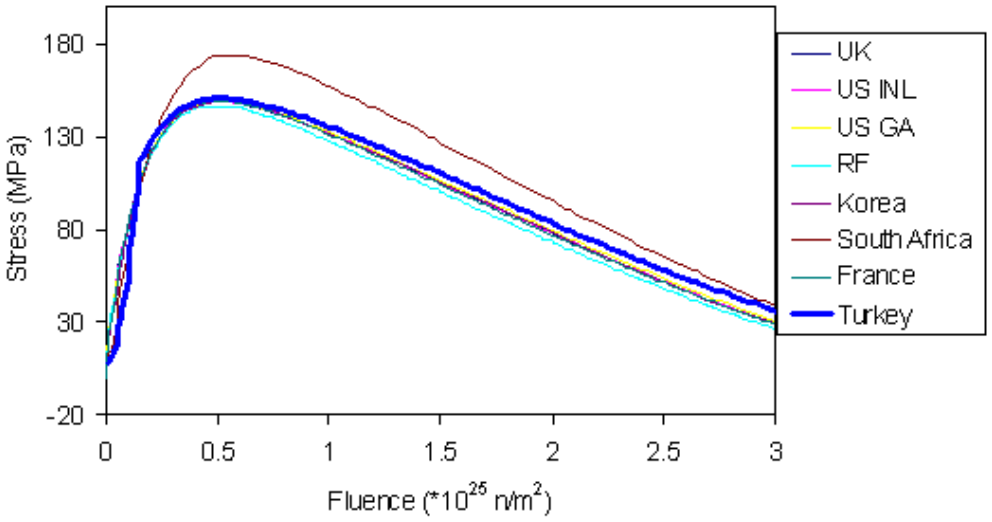

Figure A.32: Case 4d results of participating countries, tangential stress on IPyC layer

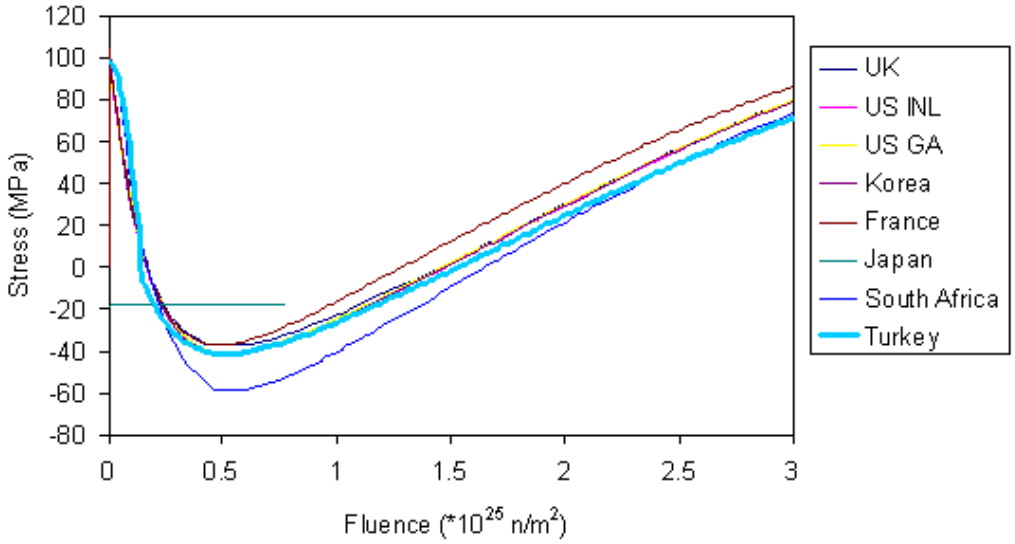

Figure A.33: Case 4d results of participating countries, tangential stress on SiC layer

Case 5 TRISO, 350 μm Kernel

This is a full three layer (TRISO) coated particle with a 350 μm diameter kernel under realistic service conditions. Finite element model is composed of three layers. These three layers are the so-called load bearing layers, which are the IPyC, SiC and OPyC. The particle is under pressure load from the fission gases. For Cases 5 through 8, the gas pressure increases linearly with time, up to the given value. Creep, irradiation-induced swelling/shrinkage and thermal stress are the other loads modelled for the rest of the CRP study. Fuel characteristics, irradiation conditions and material properties for Cases 5 through 8 are presented in Tables A.8, A.9 and A.10, respectively. The variations of tangential stress for the IPyC and SiC layers with fast neutron fluence are presented in Figures A.34 and A.35, respectively. The results are consistent with those of the other countries [40]. Case 5 results of the participating countries are presented in Figures A.36 and A.37.

Table A.8: Fuel characteristics for Cases 5-8

Parameter	Case 5	Case 6	Case 7	Case 8
Oxygen to uranium ratio	2	2	2	2
Carbon to uranium ratio	0	0	0	0
U-235 enrichment (weight $\%$)	10	10	10	10
Kernel diameter (μm)	350	500	500	500
Buffer thickness (μm)	100	100	100	100
IPyC thickness (μm)	40	40	40	40
SiC thickness (μm)	35	35	35	35
OPyC thickness (μm)	40	40	40	40
Kernel density (Mg/m^3)	10.8	10.8	10.8	10.8
Buffer density (Mg/m^3)	0.95	0.95	0.95	0.95
IPyC density (Mg/m^3)	1.90	1.90	1.90	1.90
SiC density (Mg/m^3)	3.2	3.2	3.2	3.2
IPyC BAF	1.03	1.03	1.06	1.03
OPyC BAF	1.03	1.03	1.06	1.03

$$\text{PyC radial swelling/shrinkage rate}[(\Delta L/L)/10^{25} n/m^2] = \quad \text{(A.3)}$$
$$7.27026 \times 10^{-4} x^3 - 5.05553 \times 10^{-3} x^2 + 1.83715 \times 10^{-2} x - 2.12522 \times 10^{-2}$$

Table A.9: Irradiation conditions for Cases 5-8

Parameter	Case 5	Case 6	Case 7	Case 8
Irradiation duration (efpd)	1000	1000	1000	1000
End of life burnup (% FIMA)	10	10	10	10
End of life fluence (10^{25} n/m^2, E $>$ 0.18 MeV)	3	3	3	3
Constant temperature (K)	1273	1273	1273	873 to 1273 (10 cycles)
Constant internal pressure (MPa)	15.54	2.20	26.20	From table [25]
Ambient pressure (MPa)	0.1	0.1	0.1	0.1

Table A.10: Material properties for Cases 5-8

Parameter	Case 5	Case 6	Case 7	Case 8
PyC modulus of elasticity (MPa)	3.96×10^4	3.96×10^4	3.96×10^4	3.96×10^4
PyC Poisson's ratio	0.33	0.33	0.33	0.33
PyC Poisson's ratio in creep	none	0.5	0.5	0.5
PyC coefficient of thermal expansion (K^{-1})	5.5×10^{-6}	5.5×10^{-6}	5.5×10^{-6}	5.5×10^{-6}
PyC creep coefficient ((MPa–10^{25} n/m^2)$^{-1}$, E $>$ 0.18 MeV)	None	2.71×10^{-4}	2.71×10^{-4}	Eq. A.7
PyC swelling strain rate ((ΔL/L)/10^{25} n/m^2, E $>$ 0.18 MeV)	Eq. A.1, A.2	Eq. A.1, A.2	Eq. A.3, A.4	Eq. A.5, A.6
SiC modulus of elasticity (MPa)	3.70×10^5	3.70×10^5	3.70×10^5	3.70×10^5
SiC Poisson's ratio	0.13	0.13	0.13	0.13
SiC coefficient of thermal expansion (K^{-1})	4.9×10^{-6}	4.9×10^{-6}	4.9×10^{-6}	4.9×10^{-6}

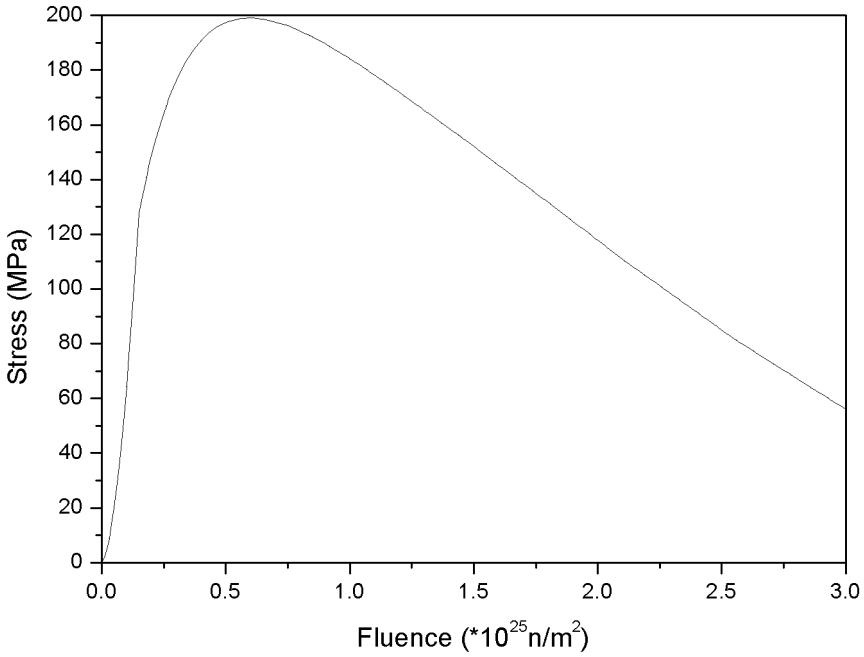

Figure A.34: Tangential stress on IPyC layer for Case 5

PyC tangential swelling/shrinkage rate$[(\Delta L/L)/10^{25}n/m^2] =$ (A.4)

$-8.88086 \times 10^{-4}x^3 + 5.03465 \times 10^{-3}x^2 - 3.42182 \times 10^{-3}x - 1.79113 \times 10^{-2}$

PyC radial swelling/shrinkage rate$[(\Delta L/L)/10^{25}n/m^2] =$ (A.5)

$4.03266 \times 10^{-4}x^3 - 2.25937 \times 10^{-3}x^2 + 9.82884 \times 10^{-3}x - 1.80613 \times 10^{-2}$

PyC tangential swelling/shrinkage rate$[(\Delta L/L)/10^{25}n/m^2] =$ (A.6)

$-4.91648 \times 10^{-4}x^3 + 2.32979 \times 10^{-3}x^2 + 1.71315 \times 10^{-3}x - 1.78392 \times 10^{-2}$

PyC creep coefficient$[(MPa - 10^{25}n/m^2)^{-1}, E > 0.18MeV] =$ (A.7)

$4.386 \times 10^{-4} - 9.7 \times 10^{-7}\ T + 8.0294 \times 10^{-10}\ T^2$

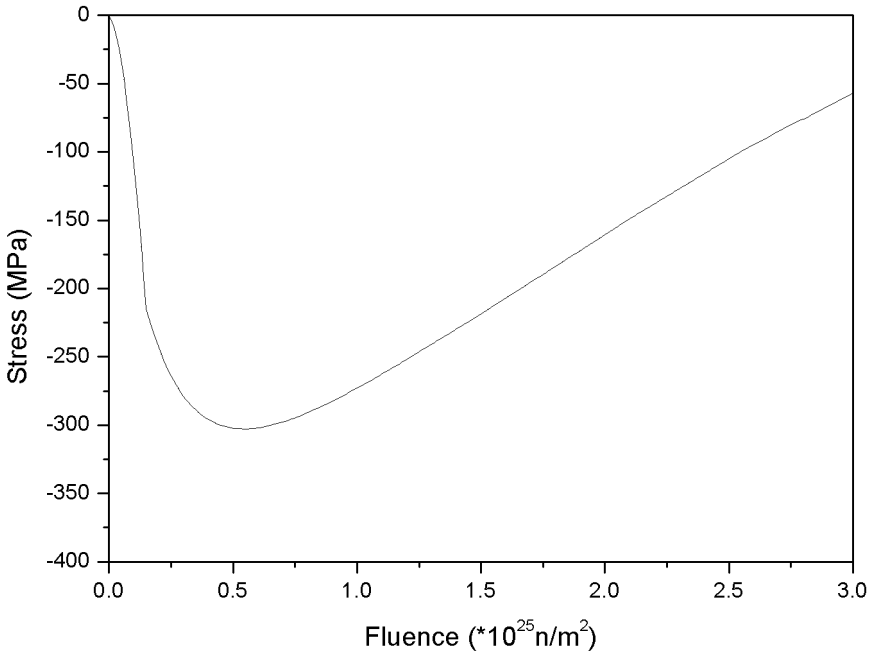

Figure A.35: Tangential stress on SiC layer for Case 5

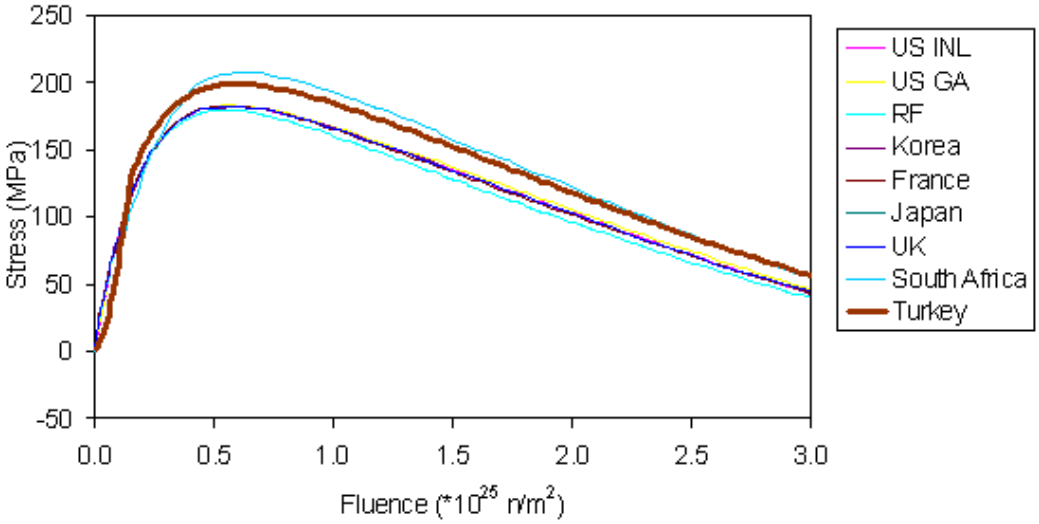

Figure A.36: Case 5 results of participating countries, tangential stress on IPyC layer

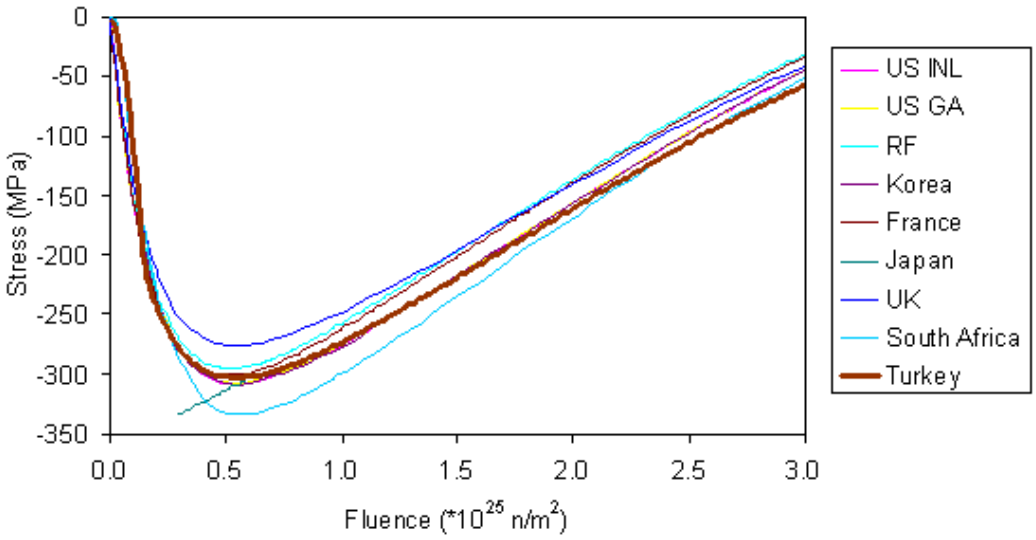

Figure A.37: Case 5 results of participating countries, tangential stress on SiC layer

Case 6 TRISO, 500 μm Kernel

Case 6 TRISO coated particle has a 500 μm diameter kernel with all other parameters the same as in Case 5. Fuel characteristics, irradiation conditions and material properties are presented in Tables A.8, A.9 and A.10, respectively. Comparison metric for Case 6 is the maximum IPyC and SiC tangential stress as a function of fast neutron fluence. The variations of tangential stress for the IPyC and SiC layers with fast neutron fluence are presented in Figures A.38 and A.39, respectively. The results are consistent with those of the other countries [40]. Case 6 results of the participating countries are presented in Figures A.40 and A.41.

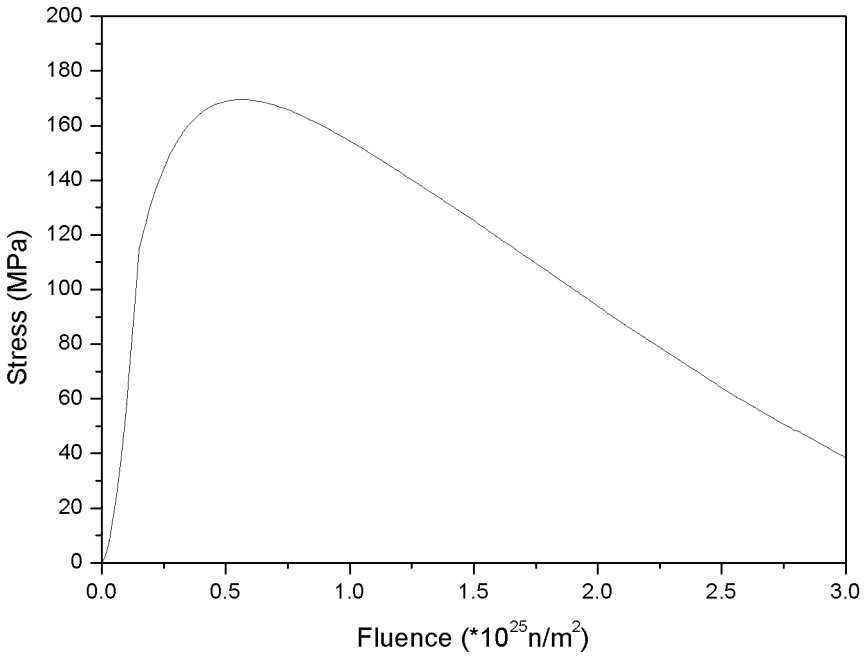

Figure A.38: Tangential stress on IPyC layer for Case 6

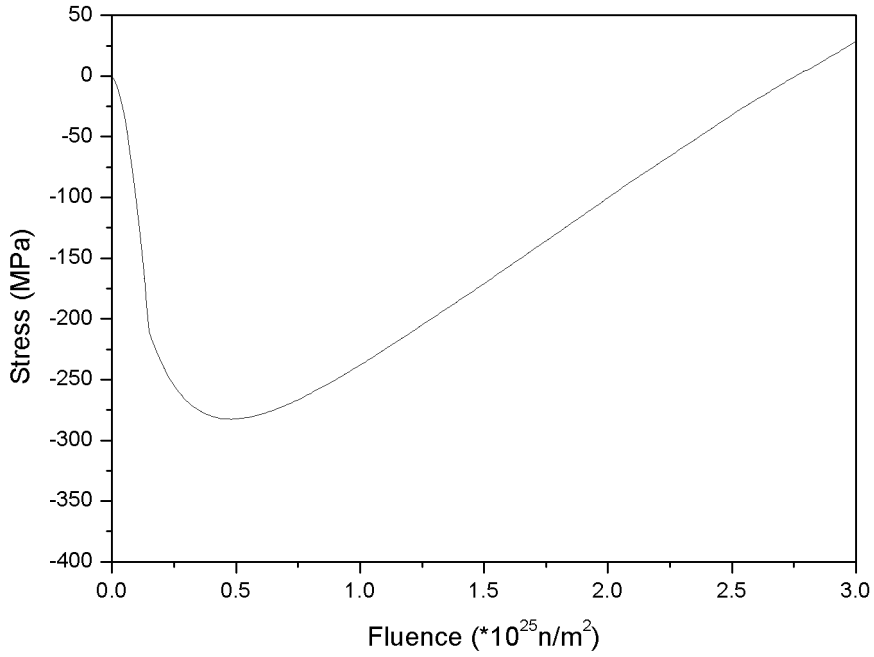

Figure A.39: Tangential stress on SiC layer for Case 6

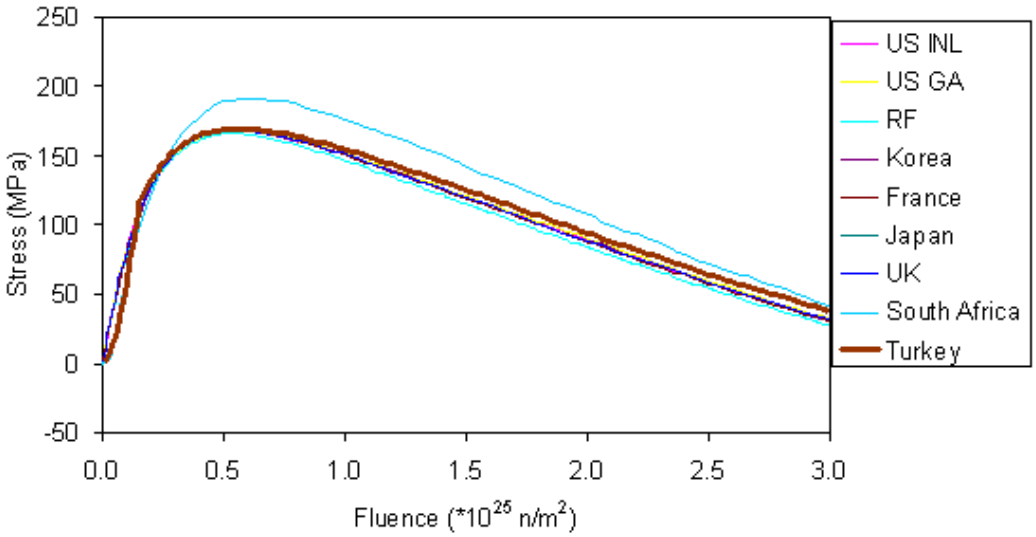

Figure A.40: Case 6 results of participating countries, tangential stress on IPyC layer

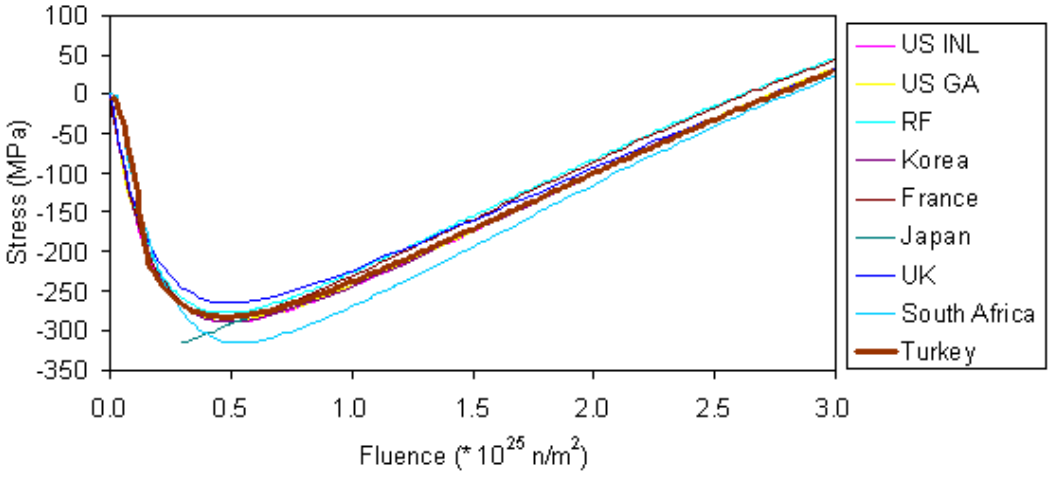

Figure A.41: Case 6 results of participating countries, tangential stress on SiC layer

Case 7 TRISO, High BAF

This particle is the same as in Case 6 except that the pyrocarbon BAF is increased to 1.06. Equations A.3 and A.4 are employed in calculation of PyC swelling strain rate as a function of fast neutron fluence. Fuel characteristics, irradiation conditions and material properties are presented in Tables A.8, A.9 and A.10, respectively. Comparison metric for Case 7 is the maximum IPyC and SiC tangential stresses as a function of fast neutron fluence. The variation of tangential stress for the IPyC and SiC layers with fast neutron fluence are presented in Figures A.42 and A.43, respectively. The results are consistent with those of the other countries [40]. Case 7 results of the participating countries are presented in Figures A.44 and A.45.

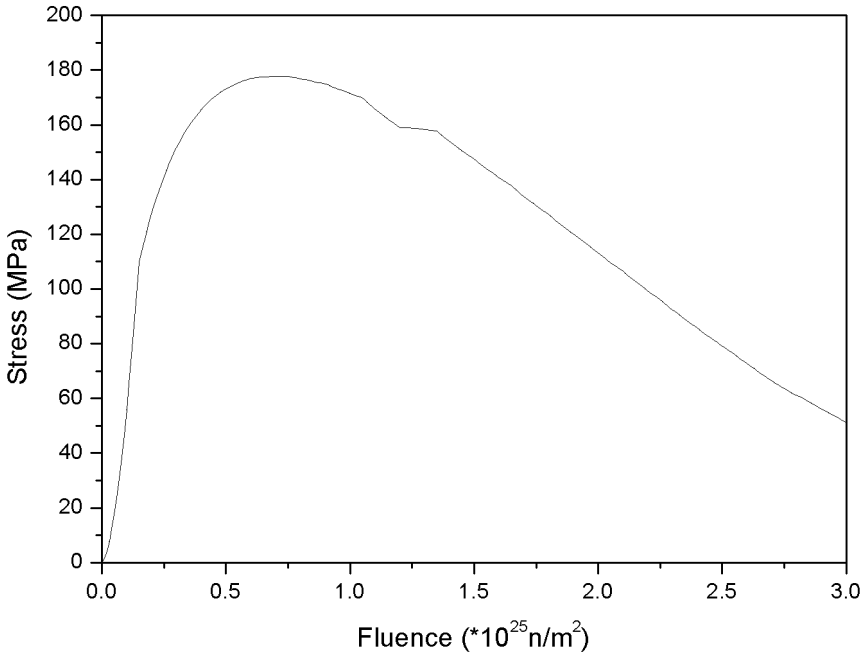

Figure A.42: Tangential stress on IPyC layer for Case 7

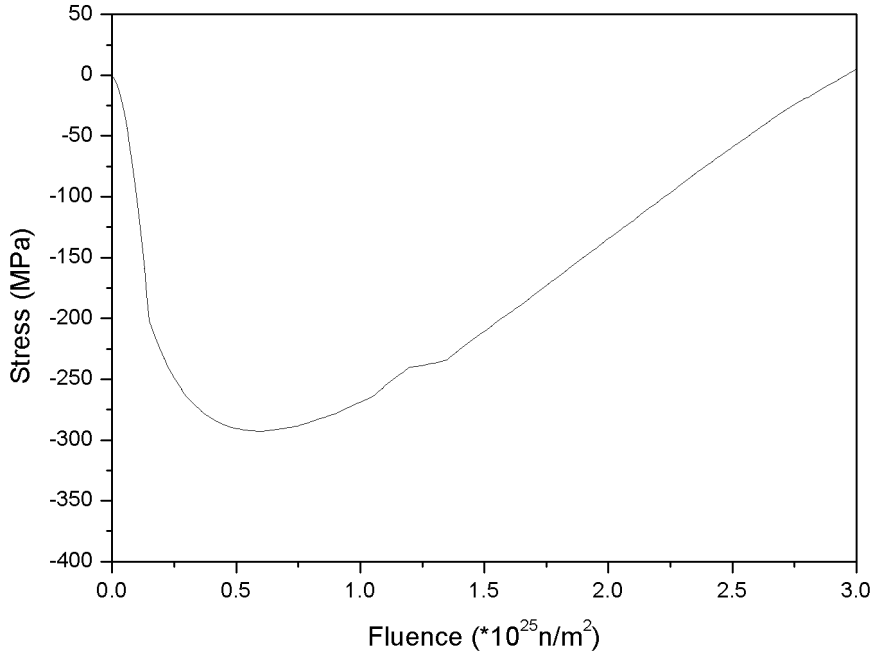

Figure A.43: Tangential stress on SiC layer for Case 7

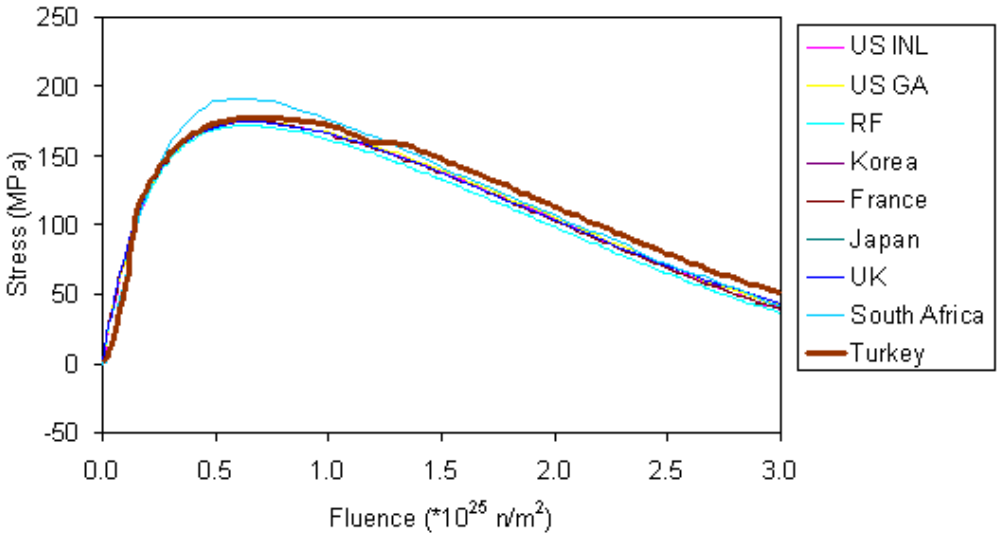

Figure A.44: Case 7 results of participating countries, tangential stress on IPyC layer

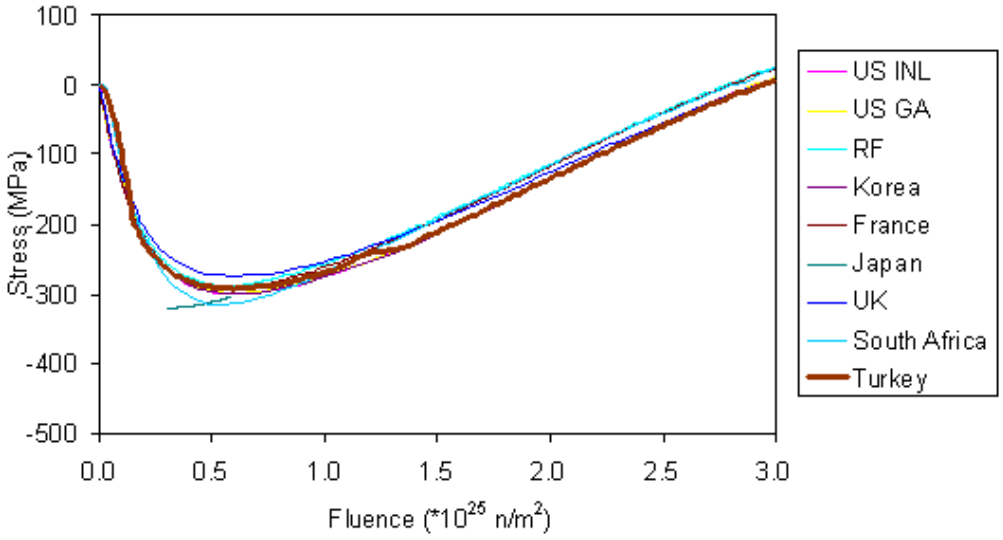

Figure A.45: Case 7 results of participating countries, tangential stress on SiC layer

Case 8 TRISO, Cyclic Temperature History

Case 8 has a TRISO coated particle subjected to a cyclic temperature history characteristic of the fuel in a pebble bed reactor. The particle is assumed to experience ten cycles, in which the temperature is initially 873 K and increases linearly to 1273 K, and then decreases immediately back to 873 K. The period for each cycle is one-tenth of the total irradiation time, or 100 days. Pressure inside the layers is presented in reference [25]. Fuel characteristics, irradiation conditions and material properties are presented in Tables A.8, A.9 and A.10, respectively. Comparison metric for Case 8 is the maximum IPyC and SiC tangential stress as a function of fast neutron fluence. The variation of tangential stress for the IPyC and SiC layers with fast neutron fluence are presented in Figures A.46 and A.47, respectively. The results are consistent with those of the other countries [40]. Case 8 results of the participating countries are presented in Figures A.48 and A.49.

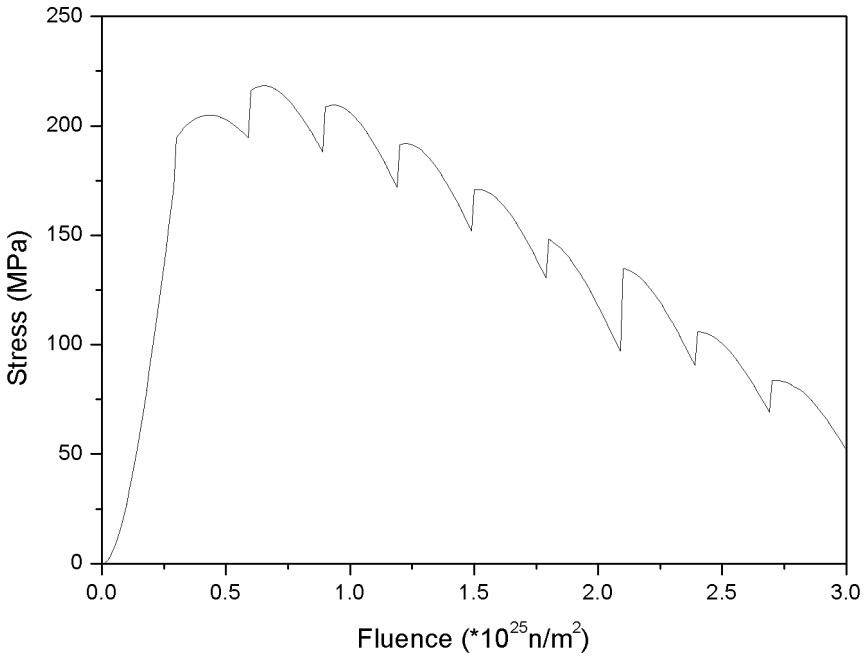

Figure A.46: Tangential stress on IPyC layer for Case 8

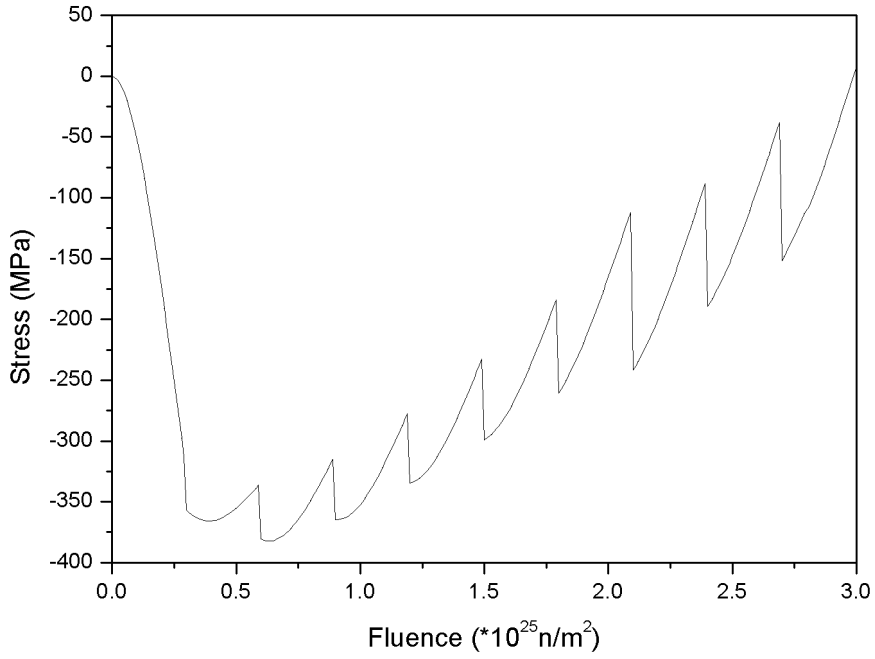

Figure A.47: Tangential stress on SiC layer for Case 8

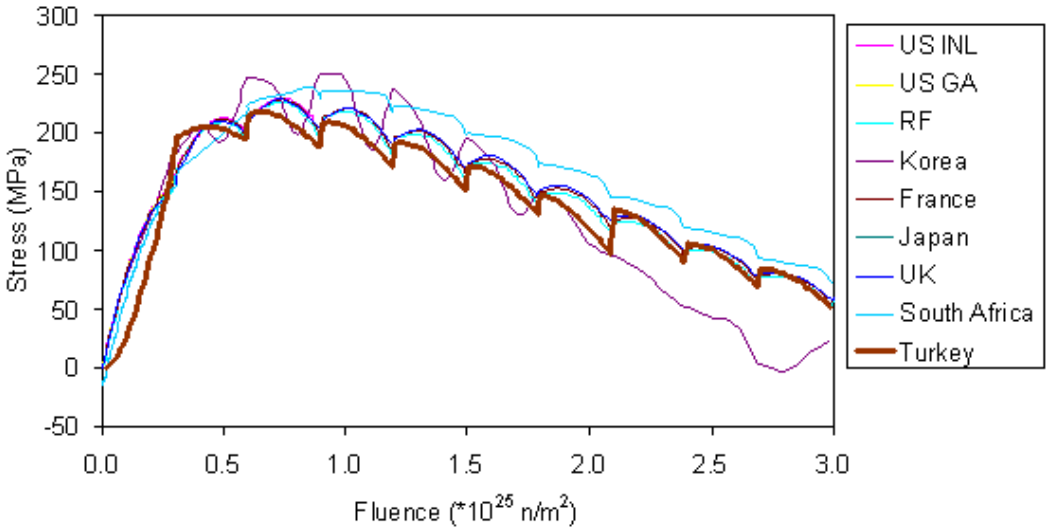

Figure A.48: Case 8 results of participating countries, tangential stress on IPyC layer

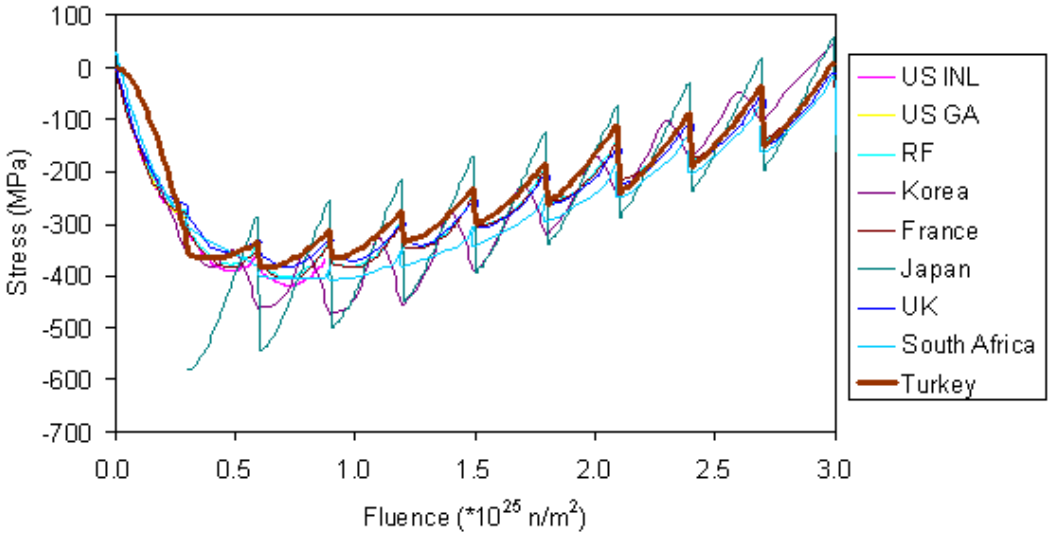

Figure A.49: Case 8 results of participating countries, tangential stress on SiC layer

Case 9 HRB-22 Experiment

Case 9 is the model of a coated fuel particle from the HRB-22 experiment. Fuel characteristics, irradiation conditions and material properties are presented in Tables A.11, A.12 and A.13, respectively. Comparison metric for this case is the failure probability of the coated fuel particle, gas pressure inside the IPyC layer and tangential stress on the SiC as a function of burnup. The change of pressure with burnup is presented in Figure A.50. SiC tangential stress as a function of burnup is presented in Figure A.51. The results are consistent with those of the other countries [40]. Case 9 results of the participating countries are presented in Figures A.52 and A.53.

Table A.11: Fuel characteristics for Cases 9-12

Parameter	Case 9	Case 10	Case 11	Case 12
Oxygen to uranium ratio	2	2	2	1.51
Carbon to uranium ratio	0	0	0	0.36
U-235 enrichment (weight $\%$)	4.07	9.82	9.82	93.15
Kernel diameter (μm)	544	497	497	200
Buffer thickness (μm)	97	94	94	102
IPyC thickness (μm)	40	40	40	40
SiC thickness (μm)	33	41	41	35
OPyC thickness (μm)	39	40	40	39
Kernel density (Mg/m^3)	10.84	10.81	10.81	10.52
Buffer density (Mg/m^3)	1.10	1.00	1.00	0.96
IPyC density (Mg/m^3)	1.85	1.88	1.88	1.92
SiC density (Mg/m^3)	3.20	3.20	3.20	3.23
OPyC density (Mg/m^3)	1.85	1.88	1.88	1.86
IPyC BAF	1.03	1.053	1.053	1.058
OPyC BAF	1.00	1.019	1.019	1.052

$$\begin{aligned}&\text{PyC radial swelling/shrinkage rate}[(\Delta L/L)/10^{25}n/m^2] = \\ &4.52013\times10^{-4}x^5 - 8.36313\times10^{-3}x^4 + 5.67549\times10^{-2}x^3 - \\ &- 1.74247\times10^{-1}x^2 + 2.62692\times10^{-1}x - 1.43234\times10^{-1}\end{aligned} \tag{A.8}$$

$$\begin{aligned}&\text{PyC tangential swelling/shrinkage rate}[(\Delta L/L)/10^{25}n/m^2] = \\ &1.30457\times10^{-4}x^3 - 2.10029\times10^{-3}x^2 + 9.07826\times10^{-3}x - 3.24737\times10^{-2}\end{aligned} \tag{A.9}$$

Table A.12: Irradiation conditions for Cases 9-12

Parameter	Case 9	Case 10	Case 11	Case 12
Irradiation duration (efpd)	89	359	351	170
End of life burnup (%FIMA)	4.79	10	14	79
End of life fluence (10^{25} n/m^2, E $>$ 0.18 MeV)	2.1	5.3	7.2	3.8
Constant temperature (K)	1303	1073	1335	1260
Ambient pressure (MPa)	0.1	0.1	0.1	0.1

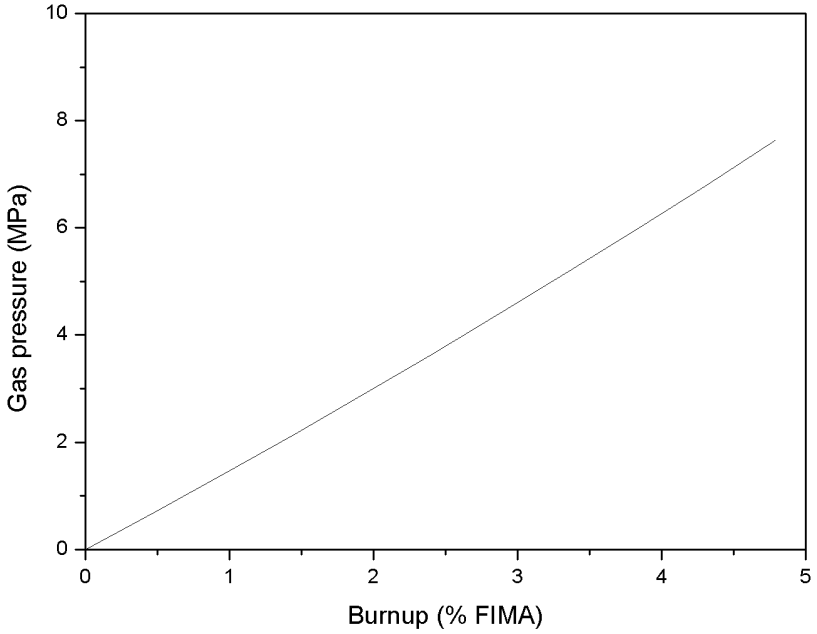

Figure A.50: Change of gas pressure with burnup for Case 9

Table A.13: Material properties for Cases 9-12

Parameter	Case 9	Case 10	Case 11	Case 12
PyC modulus of elasticity (MPa)	3.96×10^4	3.96×10^4	3.96×10^4	3.96×10^4
PyC Poisson's ratio	0.33	0.33	0.33	0.33
PyC Poisson's ratio in creep	0.4	0.4	0.4	0.5
PyC coefficient of thermal expansion (K^{-1})	5.5×10^{-6}	5.5×10^{-6}	5.5×10^{-6}	5.5×10^{-6}
PyC creep coefficient ((MPa–10^{25} n/m^2)$^{-1}$, E $>$ 0.18 MeV)	4.93×10^{-4}	4.93×10^{-4}	4.93×10^{-4}	4.93×10^{-4}
PyC swelling strain rate ((ΔL/L)/10^{25} n/m^2, E $>$ 0.18 MeV)	Eq. A.8, A.9	Eq. A.8, A.9	Eq. A.8, A.9	Eq. A.10, A.11
PyC mean strength (MPa)	200	200	200	218
PyC Weibull modulus	5.0	5.0	5.0	9.5
SiC modulus of elasticity (MPa)	3.70×10^5	3.70×10^5	3.70×10^5	3.70×10^5
SiC Poisson's ratio	0.13	0.13	0.13	0.13
SiC coefficient of thermal expansion (K^{-1})	4.9×10^{-6}	4.9×10^{-6}	4.9×10^{-6}	4.9×10^{-6}
SiC mean strength (MPa)	873	873	873	572
SiC Weibull modulus	8.02	8.02	8.02	6.00

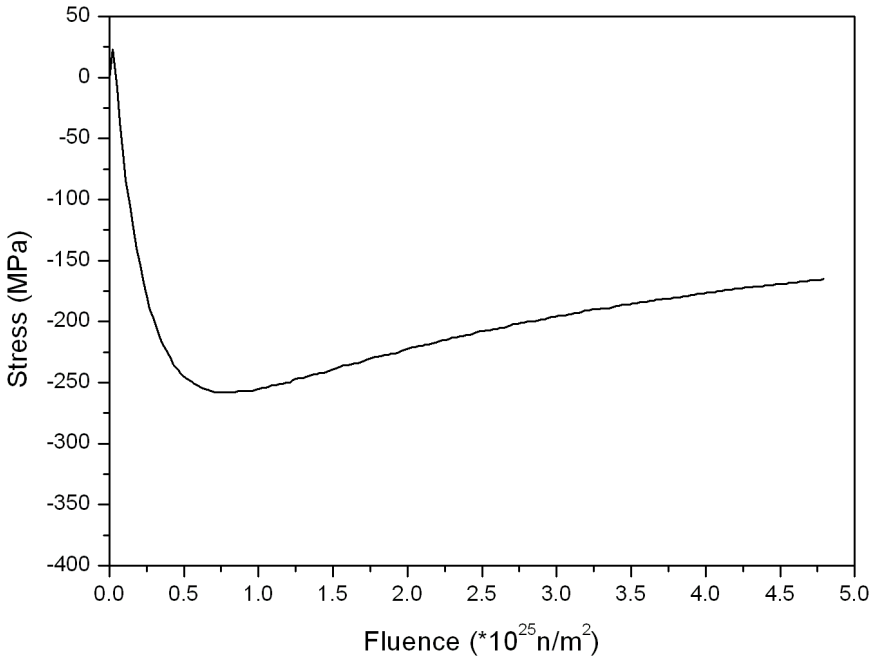

Figure A.51: Change of SiC tangential stress with burnup for Case 9

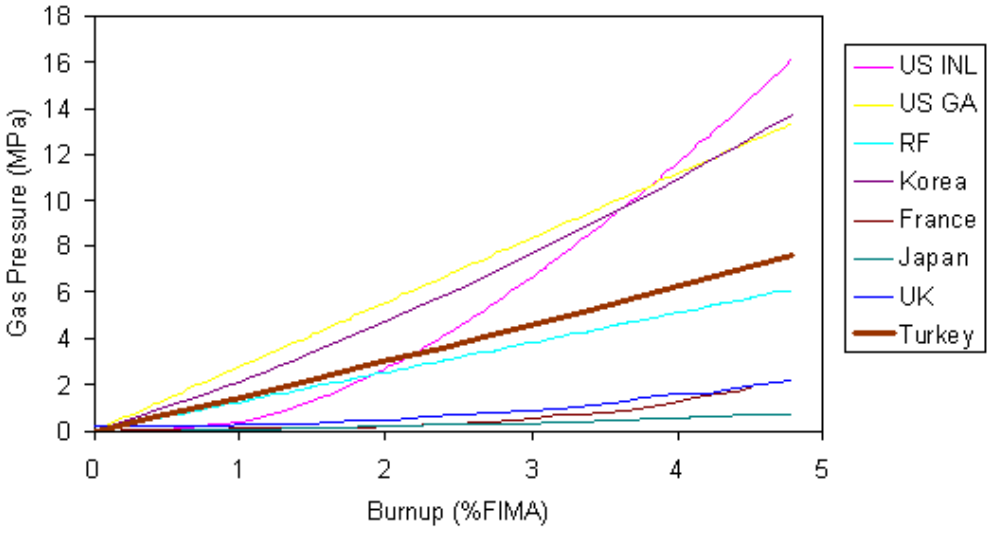

Figure A.52: Case 9 results of participating countries, change of gas pressure with burnup

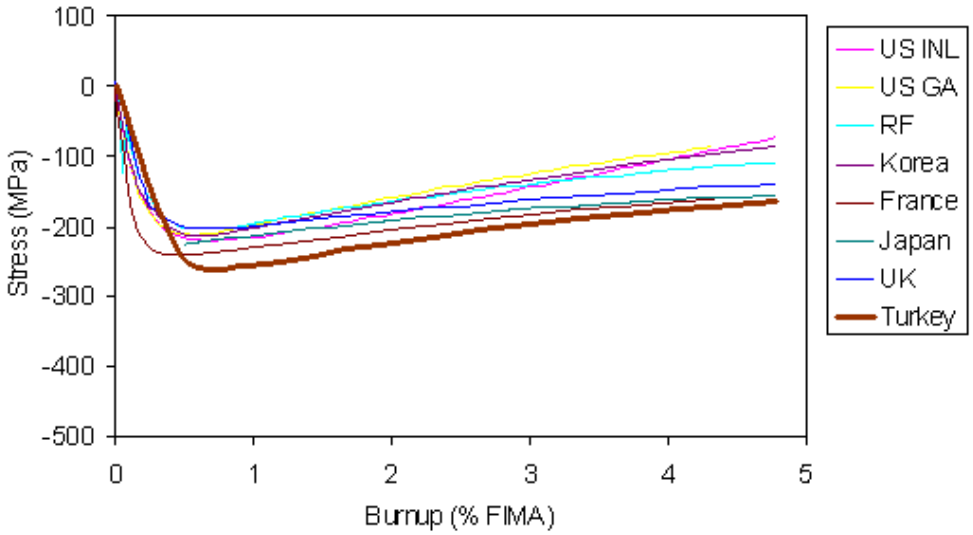

Figure A.53: Case 9 results of participating countries, tangential stress on SiC layer

$$\text{PyC radial swelling/shrinkage rate}[(\Delta L/L)/10^{25} n/m^2] = \tag{A.10}$$
$$4.73765 \times 10^{-4} x^3 - 3.80252 \times 10^{-3} x^2 + 1.64999 \times 10^{-2} x - 2.13483 \times 10^{-2}$$

$$\text{PyC tangential swelling/shrinkage rate}[(\Delta L/L)/10^{25} n/m^2] = \tag{A.11}$$
$$-1.03249 \times 10^{-3} x^3 + 5.47396 \times 10^{-3} x^2 - 3.29740 \times 10^{-3} x - 1.83549 \times 10^{-2}$$

Case 10 HFR-K3 B/2 Experiment

Case 10 is the model of a coated fuel particle from the HFR-K3 B/2 experiment. Fuel characteristics, irradiation conditions and material properties are presented in Tables A.11, A.12 and A.13, respectively. Comparison metric for this case is the failure probability of the coated fuel particle, gas pressure inside the IPyC layer and tangential stress on the SiC as a function of burnup. The change of pressure with burnup is presented in Figure A.54. The SiC tangential stress as a function of burnup is presented in Figure A.55. The results are consistent with those of the other countries [40]. Case 10 results of the participating countries are presented in Figures A.56 and A.57.

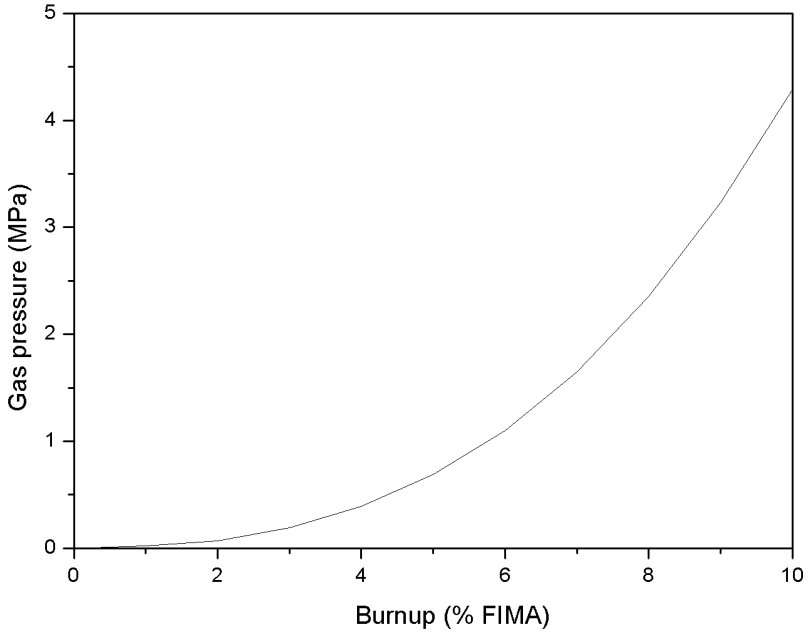

Figure A.54: Change of gas pressure with burnup for Case 10

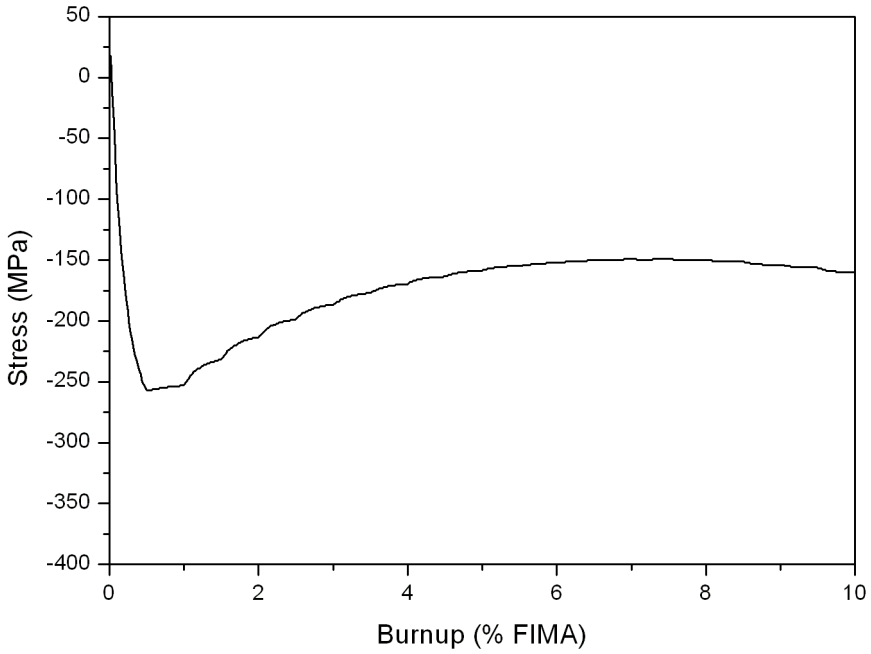

Figure A.55: Change of SiC tangential stress with burnup for Case 10

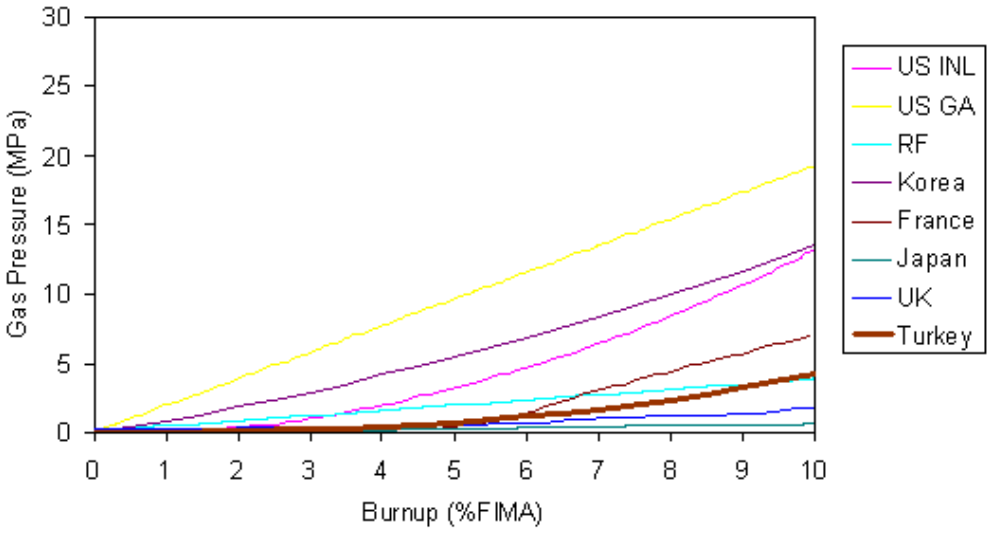

Figure A.56: Case 10 results of participating countries, change of gas pressure with burnup

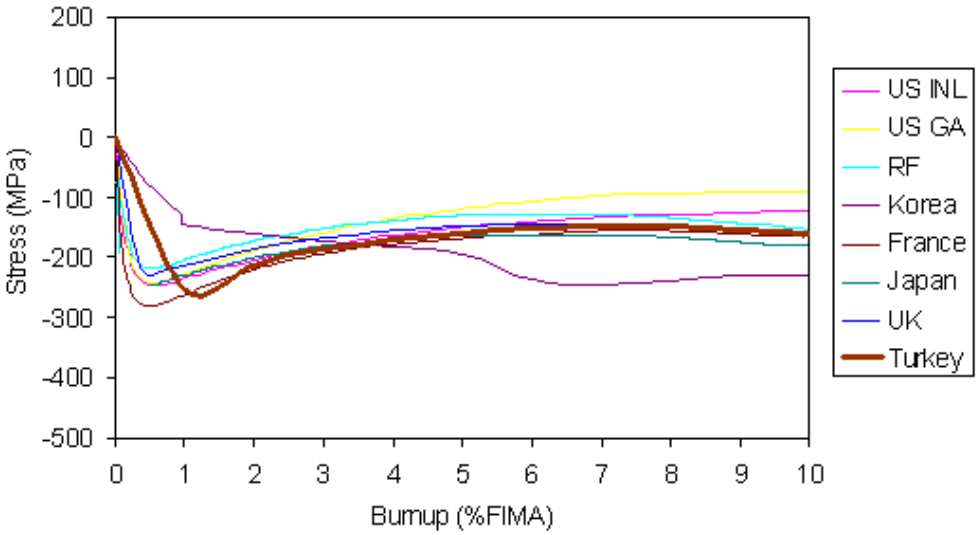

Figure A.57: Case 10 results of participating countries, tangential stress on SiC layer

Case 11 HFR-P4 3 Experiment

Case 11 is the model of a coated fuel particle from the HFR-P4 3 experiment. Fuel characteristics, irradiation conditions and material properties are presented in Tables A.11, A.12 and A.13, respectively. Comparison metric for this case is the failure probability of the coated fuel particle, gas pressure inside the IPyC layer and tangential stress on the SiC as a function of burnup. The change of pressure with burnup is presented in Figure A.58. The SiC tangential stress as a function of burnup is presented in Figure A.59. The results are consistent with those of the other countries [40]. Case 11 results of the participating countries are presented in Figures A.60 and A.61.

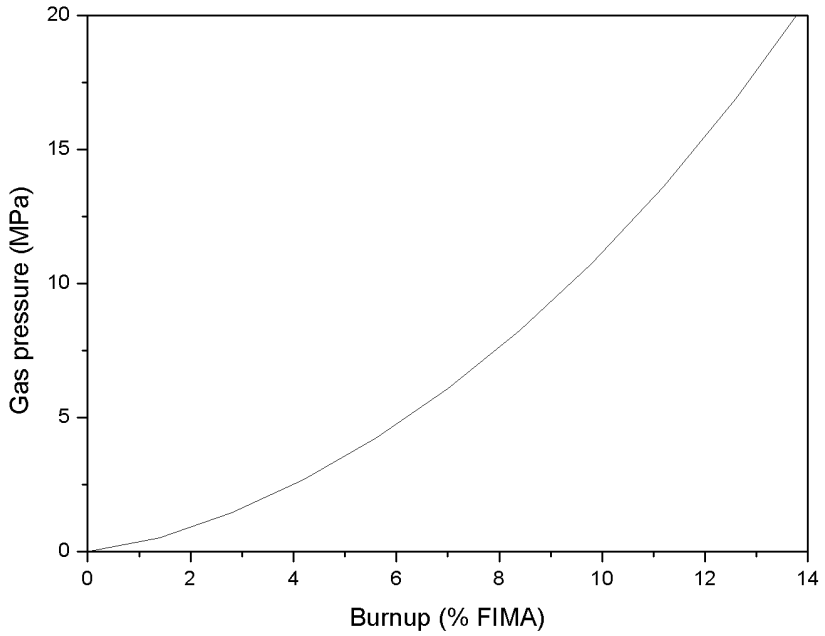

Figure A.58: Change of gas pressure with burnup for Case 11

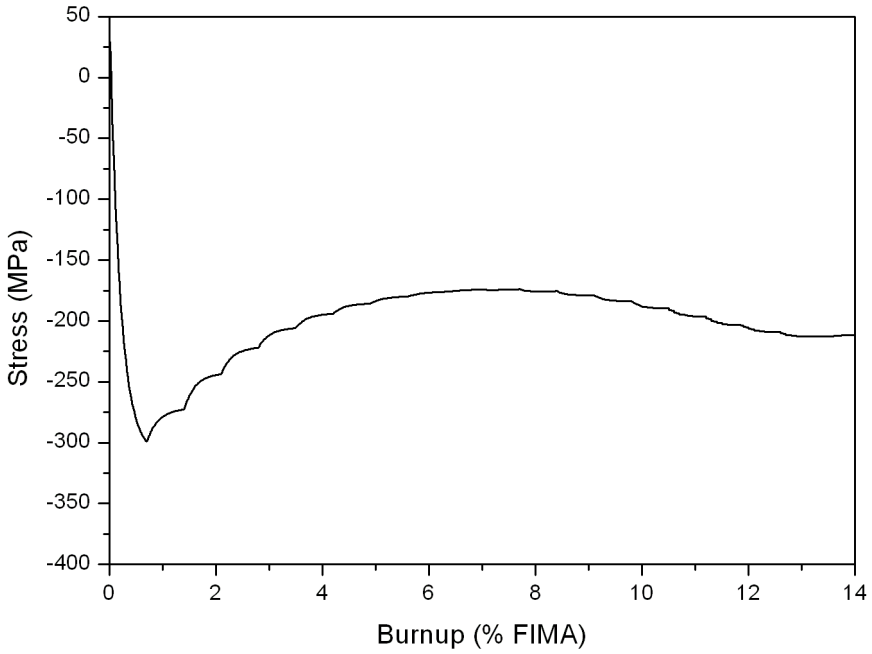

Figure A.59: Change of SiC tangential stress with burnup for Case 11

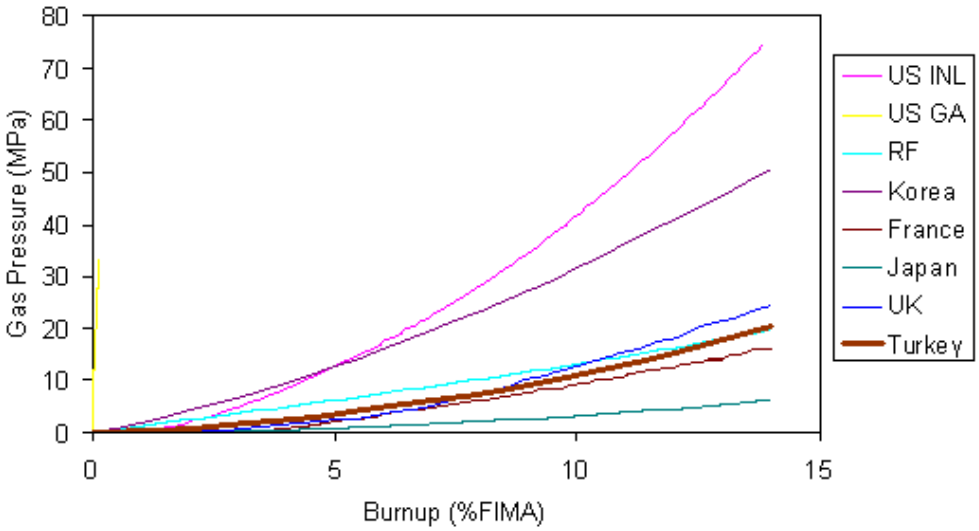

Figure A.60: Case 11 results of participating countries, change of gas pressure with burnup

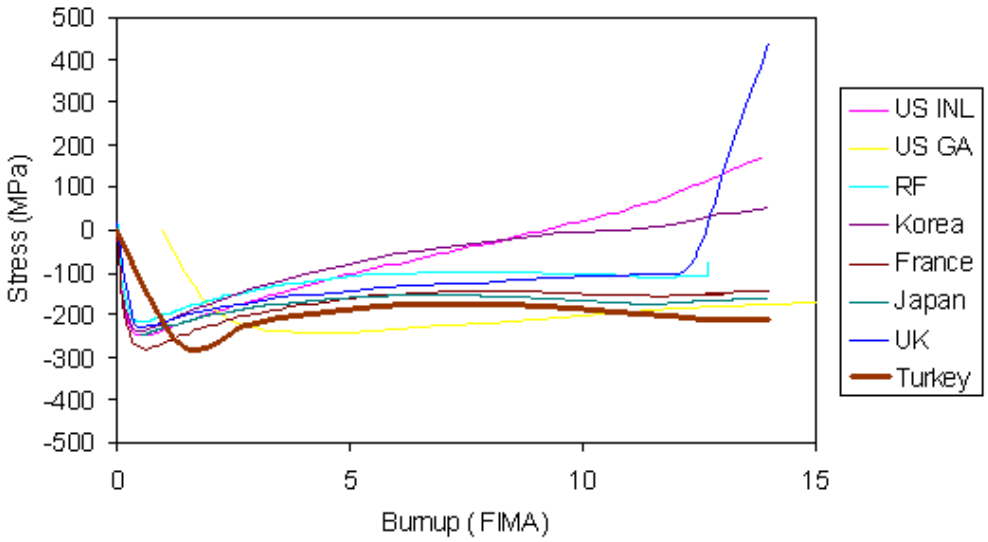

Figure A.61: Case 11 results of participating countries, tangential stress on SiC layer

Case 12 NPR-1A 5 Experiment

Case 12 is the model of a coated fuel particle from the NPR-1A 5 experiment. Fuel characteristics, irradiation conditions and material properties are presented in Tables A.11, A.12 and A.13, respectively. Comparison metric for this case is the failure probability of the coated fuel particle, gas pressure inside the IPyC layer and tangential stress on the SiC as a function of burnup. The change of pressure with burnup is presented in Figure A.62. The SiC tangential stress as a function of burnup is presented in Figure A.63. The results are consistent with those of the other countries [40]. Case 12 results of the participating countries are presented in Figures A.64 and A.65.

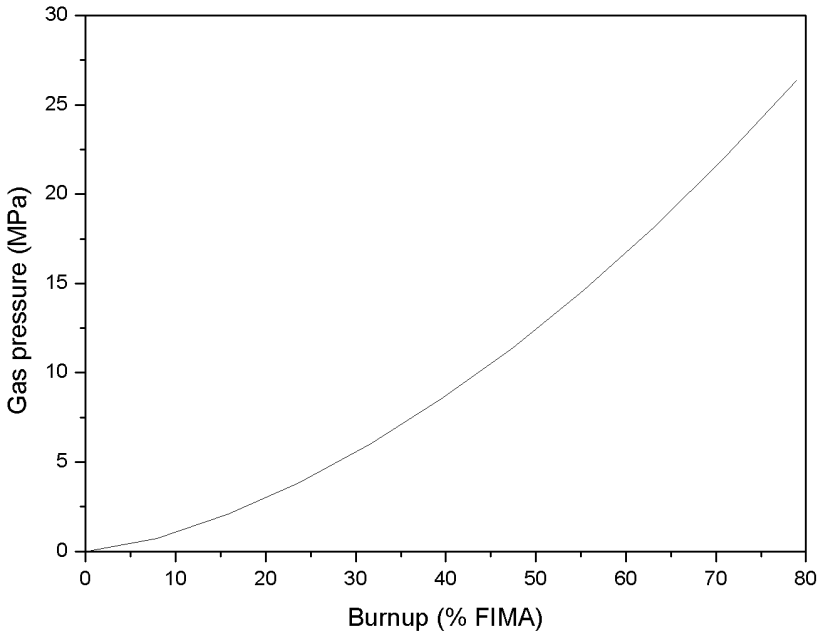

Figure A.62: Change of gas pressure with burnup for Case 12

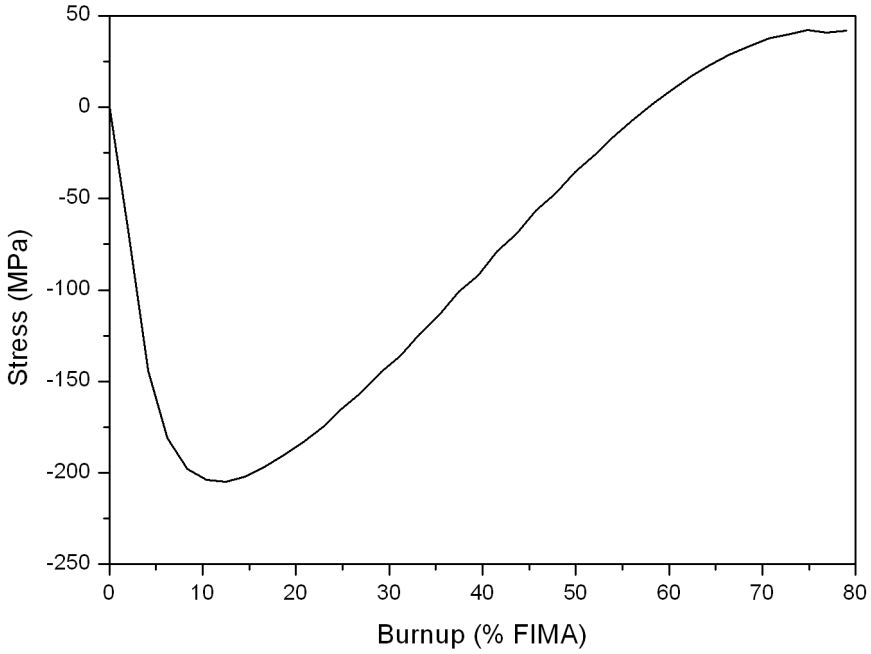

Figure A.63: Change of SiC tangential stress with burnup for Case 12

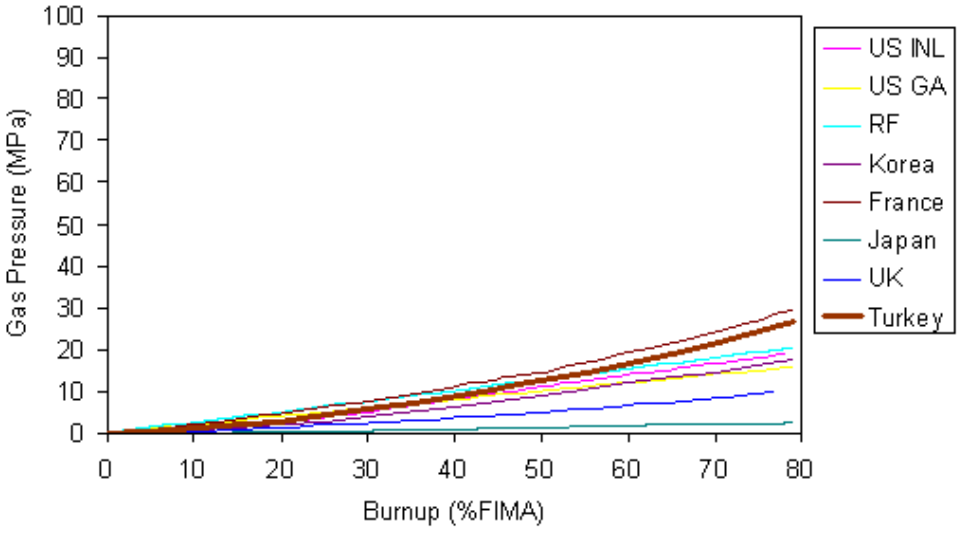

Figure A.64: Case 12 results of participating countries, change of gas pressure with burnup

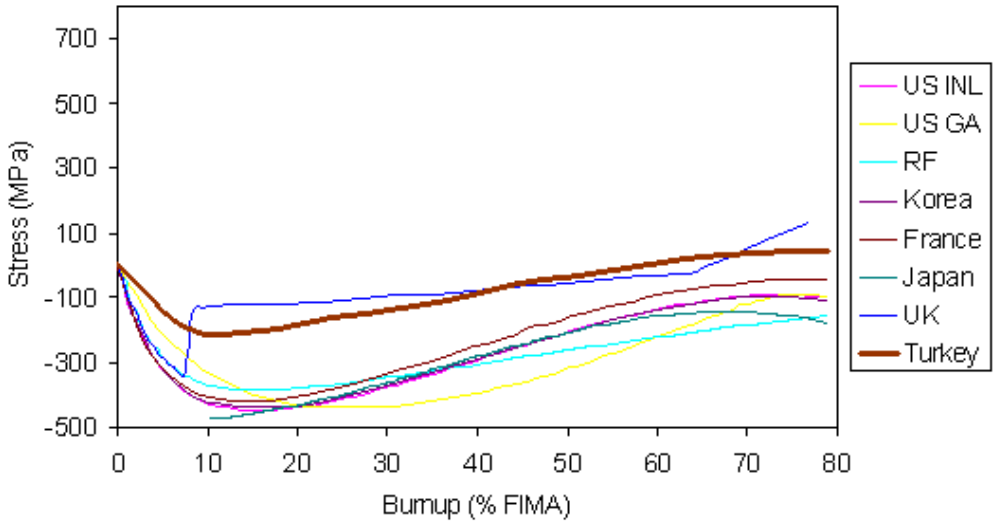

Figure A.65: Case 12 results of participating countries, tangential stress on SiC layer

Case 13 HFR EU-1 Experiment

Case 13 is the model of a coated fuel particle from the HFR EU-1 experiment. Fuel characteristics, irradiation conditions and material properties are presented in Tables A.14, A.15 and A.16, respectively. The change of pressure with burnup is presented in Figure A.66. The SiC tangential stress as a function of burnup is presented in Figure A.67. The results are consistent with those of the other countries [40]. Case 13 results of the participating countries are presented in Figures A.68 and A.69.

Table A.14: Fuel characteristics for Cases 13-14

Parameter	Case 13	Case 14
Oxygen to uranium ratio	2	2
Carbon to uranium ratio	0	0
U-235 enrichment (weight $\%$)	16.7	10.6
Kernel diameter (μm)	502	508
Buffer thickness (μm)	95	102
IPyC thickness (μm)	41	39
SiC thickness (μm)	35	36
OPyC thickness (μm)	40	38
Kernel density (Mg/m^3)	10.81	10.72
Buffer density (Mg/m^3)	1.01	1.02
IPyC density (Mg/m^3)	1.90	1.90
SiC density (Mg/m^3)	3.2	3.2
IPyC BAF	1.02	1.04
OPyC BAF	1.02	1.02

Table A.15: Irradiation conditions for Cases 13-14

Parameter	Case 13	Case 14
Irradiation duration (efpd)	600	350
End of life burnup (% FIMA)	20	10
End of life fluence (10^{25} n/m^2, E $>$ 0.18 MeV)	5.4	4.5
Constant temperature (K)	1298	1323
Ambient pressure (MPa)	0.1	0.1

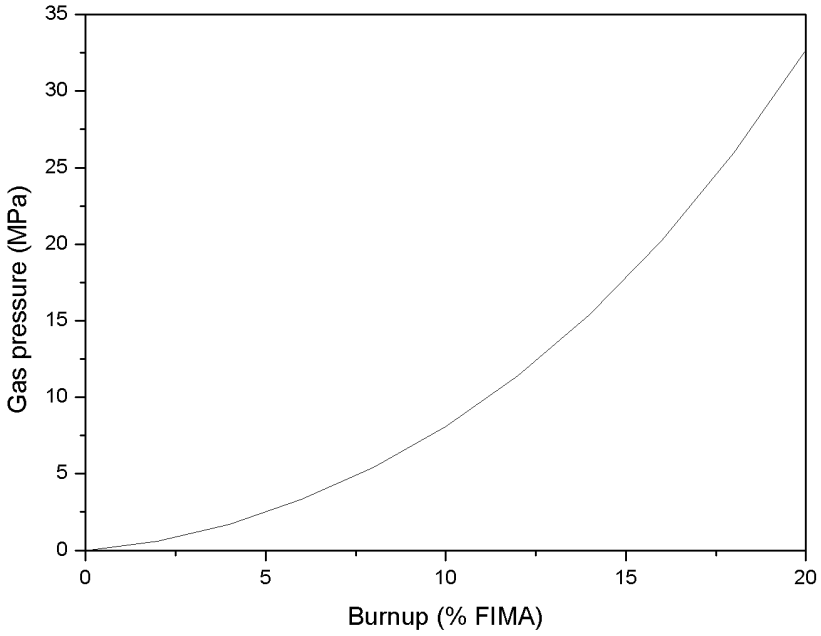

Figure A.66: Change of gas pressure with burnup for Case 13

Table A.16: Material properties for Cases 13-14

Parameter	Case 13	Case 14
PyC modulus of elasticity (MPa)	3.96×10^4	3.96×10^4
PyC Poisson's ratio	0.33	0.33
PyC Poisson's ratio in creep	0.4	0.4
PyC coefficient of thermal expansion (K^{-1})	5.5×10^{-6}	5.5×10^{-6}
PyC creep coefficient ((MPa–10^{25} n/m^2)$^{-1}$, E $>$ 0.18 MeV)	4.93×10^{-4}	4.93×10^{-4}
PyC swelling strain rate ((ΔL/L)/10^{25} n/m^2, E $>$ 0.18 MeV)	Eq. A.8, A.9	Eq. A.8, A.9
PyC mean strength (MPa)	200	200
PyC Weibull modulus	5.0	5.0
SiC modulus of elasticity (MPa)	3.70×10^5	3.70×10^5
SiC Poisson's ratio	0.13	0.13
SiC coefficient of thermal expansion (K^{-1})	4.9×10^{-6}	4.9×10^{-6}
SiC mean strength (MPa)	873	873
SiC Weibull modulus	8.02	8.02

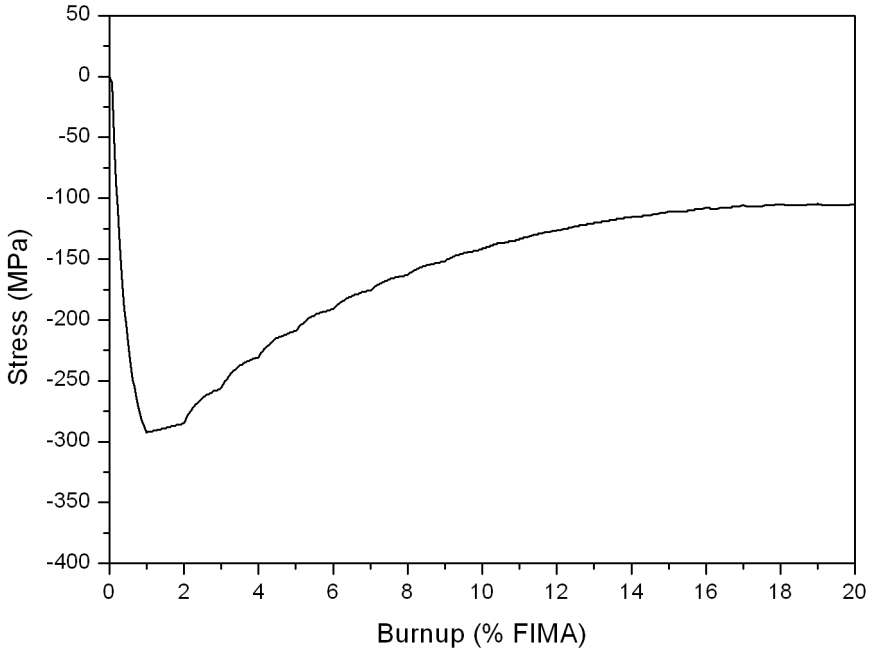

Figure A.67: Change of SiC tangential stress with burnup for Case 13

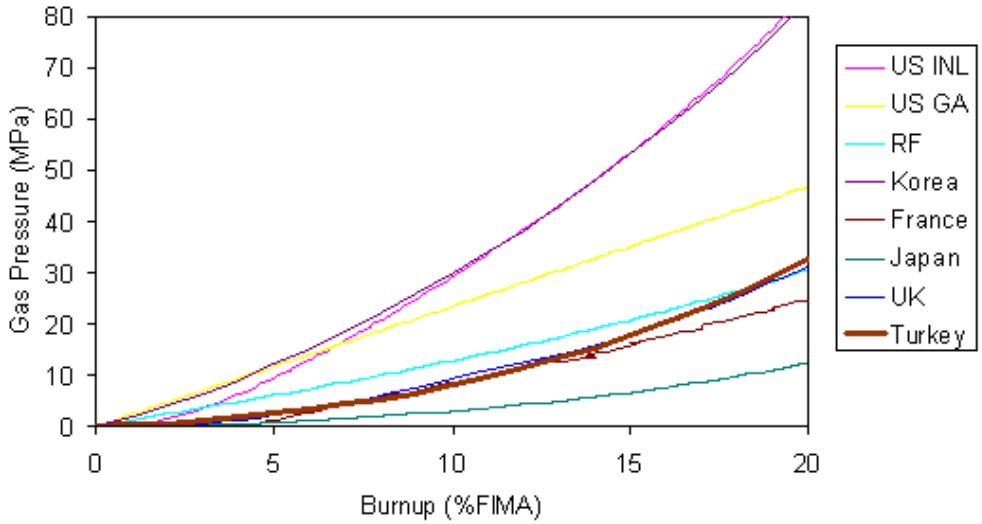

Figure A.68: Case 13 results of participating countries, change of gas pressure with burnup

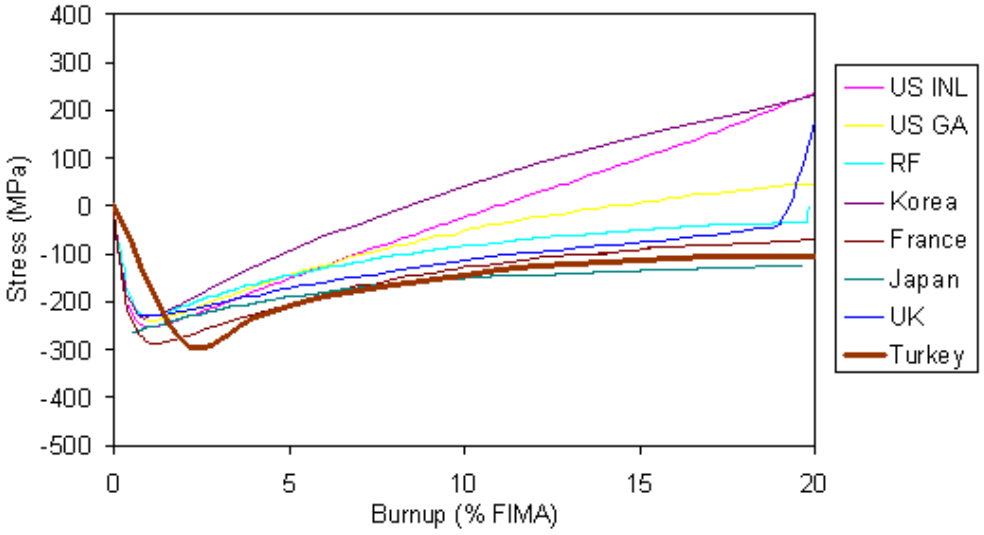

Figure A.69: Case 13 results of participating countries, tangential stress on SiC layer

Case 14 HFR EU-2 Experiment

Case 14 is the model of a coated fuel particle from the HFR EU-2 experiment. Fuel characteristics, irradiation conditions and material properties are presented in Tables A.14, A.15 and A.16, respectively. The results are consistent with those of the other countries [40]. Case 14 results of the participating countries are presented in Figures A.72 and A.73.

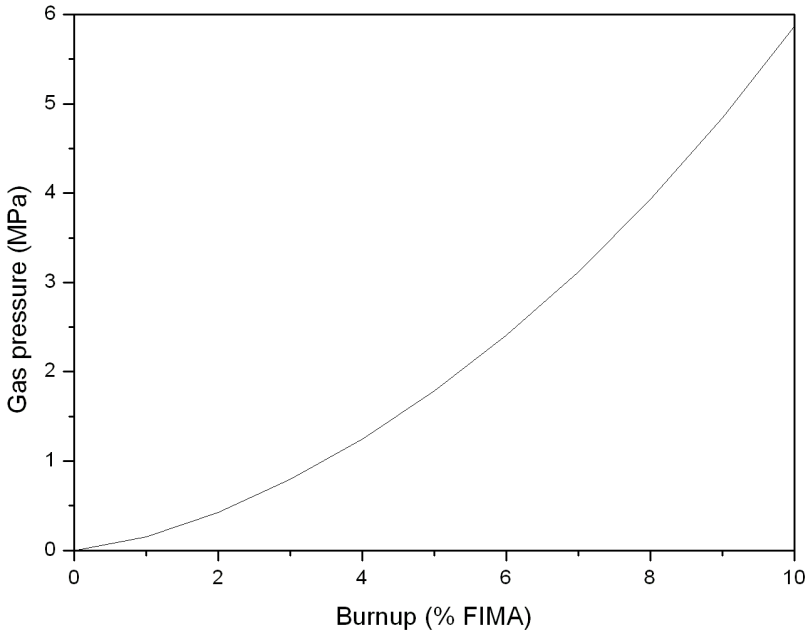

Figure A.70: Change of gas pressure with burnup for Case 14

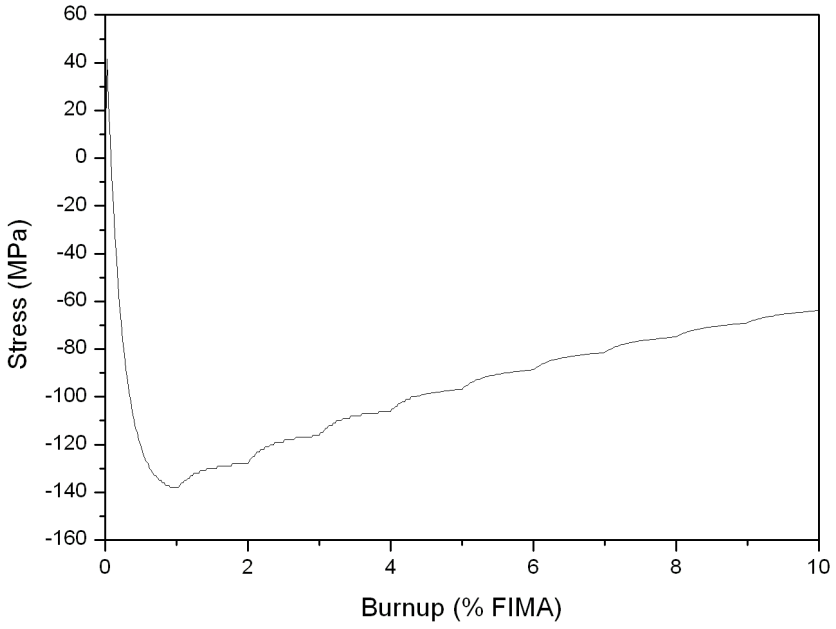

Figure A.71: Change of SiC tangential stress with burnup for Case 14

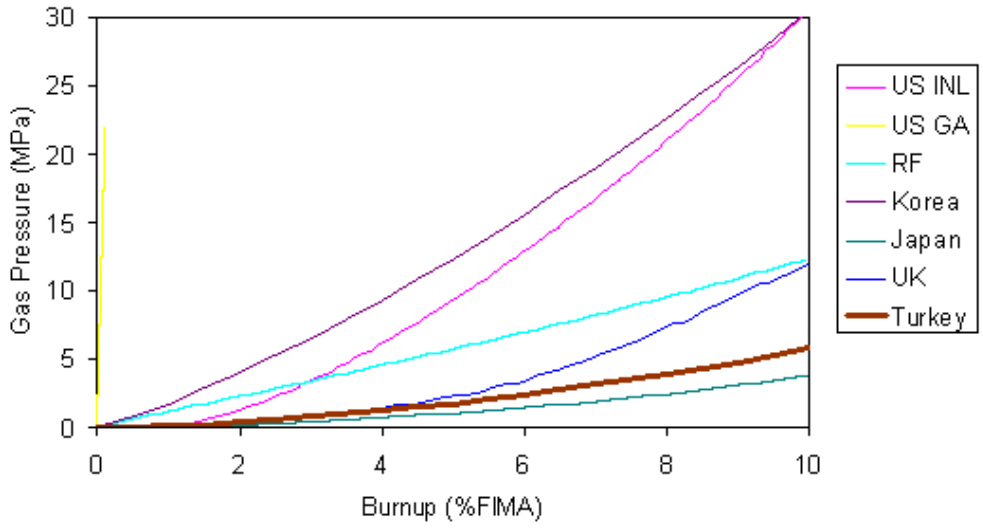

Figure A.72: Case 14 results of participating countries, change of gas pressure with burnup

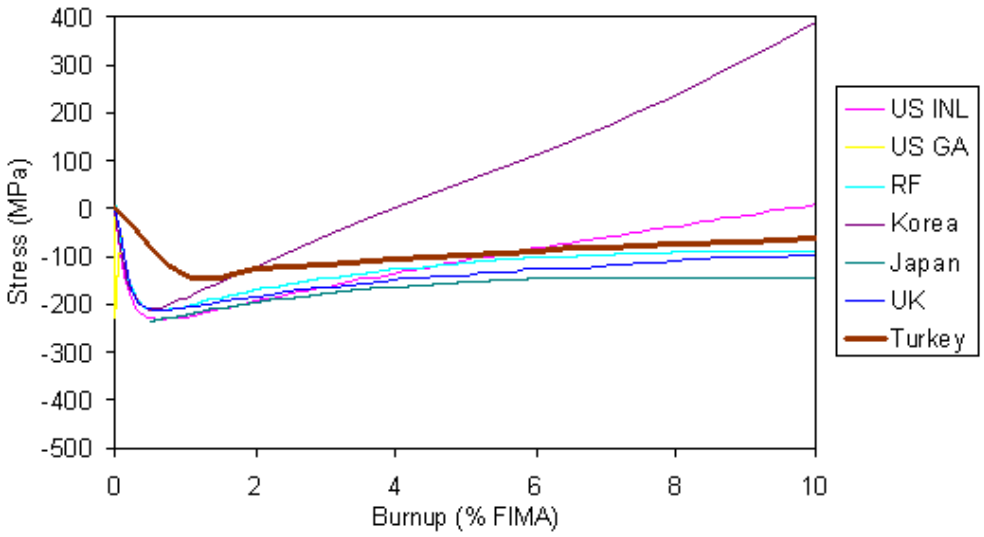

Figure A.73: Case 14 results of participating countries, tangential stress on SiC layer

Appendix B

Gas Pressure Calculation

Pressure due to fission gases and CO is the main contributor to tangential stress inside the SiC layer. This section describes the steps for calculation of this pressure.

Number of Fission Product Gas Atoms

Fission product gases Xe and Kr are assumed to be representative of the gaseous fission products. Stable gaseous fission products Xe and Kr compose 31% of the fission products. When the initial number of U atoms per kernel is known, number of fissions at each time step can be calculated. Number of fissions is the product of initial U atoms per kernel and burnup expressed in terms of FIMA (Fissions per Initial Metal Atoms). Since Xe and Kr compose 31% of the fission products, the number of Xe and Kr atoms produced inside the kernel is known at each time step. The release of the gases from the kernel are assumed to be well-represented by the Booth equivalent sphere release model. The equations representing the Booth model are presented below [17, 34].

Diffusion constant is expressed in the form:

$$D \;=\; D_0 \, e^{-E_0/(R\,T)} \tag{B.1}$$

where D_0 and E_0 are fitting parameters, R is the ideal gas constant, T is temperature and D is the diffusivity, which is assumed independent of position but may depend on time through temperature. Time-averaged diffusivity is given by:

$$\bar{D} \;=\; \frac{1}{t} \int_0^t D(t') \, dt' \tag{B.2}$$

Booth equation is expressed in terms of the dimensionless parameter t/τ given by:

$$\frac{t}{\tau} \;=\; \frac{\bar{D}\, t}{a^2} \tag{B.3}$$

where a is the radius of the sphere.

Concentration of gas atoms, c, inside a sphere of radius a with a constant generation rate per unit volume, S, can be calculated from the mass balance:

$$\frac{\partial c}{\partial t} = D\ \frac{1}{r^2}\frac{\partial}{\partial r}\left(r^2\frac{\partial c}{\partial r}\right)\ +\ S, \qquad 0\ <\ r\ <\ a \tag{B.4}$$

with the boundary conditions:

$$\left.\frac{\partial c}{\partial r}\right|_{r=0} = 0 \quad \text{and} \quad c(a,t) = 0 \quad \text{for} \quad t > 0 \tag{B.5}$$

Solving the equations B.4 and B.5 with initial condition $c(r,0)\ =\ 0$, the fractional release of the gas, defined as:

$$F(t) = \frac{-4\pi a^2 D\ \left.\frac{\partial c}{\partial r}\right|_{r=a}}{\frac{4}{3}\pi a^3 S} \tag{B.6}$$

can be calculated as follows [17]:

$$F(t) = 1\ -\ \frac{6\tau}{t}\sum_{n=1}^{\infty}\frac{1}{n^4\pi^4}\left[1 - exp\left(-n^2\pi^2\ \frac{t}{\tau}\right)\right] \tag{B.7}$$

which can be approximated as:

$$\begin{aligned} F(t) &\approx 4\sqrt{\frac{t}{\pi\tau}}\ -\ \frac{3t}{2\tau} && \text{for} \quad \frac{t}{\tau} < 0.35 \\ F(t) &\approx 1\ -\ \frac{\tau}{15t} && \text{for} \quad \frac{t}{\tau} > 0.35 \end{aligned} \tag{B.8}$$

Equations B.8 are employed in the calculations where changes are slow. For fast transients the amount of gases is assumed constant (no generation) and only their diffusion from the sphere is considered. The mass balance becomes:

$$\frac{\partial c}{\partial t} = D\ \frac{1}{r^2}\frac{\partial}{\partial r}\left(r^2\frac{\partial c}{\partial r}\right), \qquad 0 < r < a \tag{B.9}$$

with the boundary conditions B.5 and initial condition $c(r,0) = c_0$. Now, the fractional release during the transient is [34]:

$$\begin{aligned} f_B(t) &= \frac{-4\pi a^2 D\ \left.\frac{\partial c}{\partial r}\right|_{r=a}}{\frac{4}{3}\pi a^3 c_0} \\ &= 1\ -\ \frac{6}{\pi^2}\sum_{n=1}^{\infty}\frac{1}{n^2}\left[1 - exp\left(-n^2\pi^2\ \frac{t}{\tau}\right)\right] \end{aligned} \tag{B.10}$$

which can be approximated as:

$$\begin{aligned} f_B(t) &\approx 1.0006964\sqrt{\frac{36t}{\pi\tau}}\ -\ \frac{3t}{\tau} && \text{for} \quad \frac{t}{\tau} < 0.155 \\ f_B(t) &\approx 1\ -\ \frac{6}{\pi^2}exp\left(-\pi^2\frac{t}{\tau}\right) && \text{for} \quad \frac{t}{\tau} > 0.155 \end{aligned} \tag{B.11}$$

Equations B.11 are employed during fast transients.

Number of CO Molecules

In oxide-based fuel kernels, free oxygen is formed as a result of the consumption of fissionable nuclides. This free oxygen first oxidizes the rare earth elements, which have the greatest affinity for oxygen. The remaining oxygen oxidizes the other elements such as Sr, Eu, Zr and Ba in UO_2 fuels [52]. If there is still free oxygen left remaining in the system, it may diffuse out of the kernel and react with the carbon in the coating layers under appropriate conditions, resulting in CO and CO_2 production. Under HTR operating conditions, CO is formed; the CO_2 contribution is usually below a few percent [53]. Free oxygen from the kernel immediately reacts with the carbon in the buffer and forms CO. The following experimental correlation of oxygen release [53] is employed in this study to calculate the amount of CO formed inside the IPyC layer:

$$\log\left(\frac{(O/f)}{t^2}\right) = -0.21 - \frac{8500}{T} \tag{B.12}$$

where O/f is the oxygen release at the end of irradiation (atoms per fission), t is the irradiation time in days and T is the time-averaged particle surface temperature during irradiation in K. The upper limit of the O/f value is given by the stochiometric formula [17]:

$$O/f = 0.4f_U + 0.85f_{Pu} \tag{B.13}$$

where f_U is the ratio of the number of uranium fissions to the total number of fissions, and f_{Pu} is $(1-f_U)$. f_{Pu} is estimated as 2 times the burnup in FIMA units [66]. Number of fissions at the specified burnup is calculated from reaction rates and the number of CO molecules is calculated from B.12 and B.13.

Pressure Calculation

Xe, Kr and CO are assumed to fill the free volume inside the IPyC layer. The free volume on the inner side of the IPyC consists of the empty volume of the buffer, which is 50% of the fully dense material, and the free volume created by CO formation within the buffer. In addition, this volume is decreased by the swelling of the kernel, which is assumed to be 0.47% per %FIMA [52].

Fission product gases and CO molecules are assumed to fill the empty volumes inside the coated fuel particle according to Redlich-Kwong gas state law when the pressure and temperature values are within its range of validity. When Redlich-Kwong law is not applicable, the ideal gas law is employed to calculate the pressure on the inner side of the IPyC layer as a function of burnup.

Recent studies and experimental data [45] have shown that Redlich-Kwong equation of state is applicable for calculation of gas pressure. Redlich-Kwong equation of state is [51]:

$$P = \frac{RT}{V_m - b} - \frac{a}{\sqrt{T} V_m (V_m + b)} \tag{B.14}$$

where

$$a = \frac{0.42748 R^2 T_c^{2.5}}{P_c} \tag{B.15}$$

$$b = \frac{0.08662 R T_c}{P_c} \tag{B.16}$$

and P is the pressure, T is the absolute temperature, V_m is the molar volume, R is the ideal gas constant, T_c is the absolute temperature at critical point and P_c is the pressure at the critical point.

Redlich-Kwong equation is adequate for calculation of the gas phase properties when the ratio of the pressure to the critical pressure is less than about one-half of the ratio of the temperature to the critical temperature:

$$\frac{P}{P_c} < \frac{T}{2T_c} \tag{B.17}$$

The critical temperature, T_c, of a material is the temperature above which distinct liquid and gas phases do not exist. The critical pressure is the vapor pressure at the critical temperature. The critical pressure and temperature for Xe, Kr and CO are presented in Table B.1.

In gas pressure calculations, applicability of Redlich-Kwong equation has been checked with the equation B.17. Redlich-Kwong equation has produced more conservative results in the applicable range when compared to the ideal gas equation.

Table B.1: Critical pressure and critical temperature values for gases

	Xe	Kr	CO
T_c (K)	289.8	209.4	133
P_c (MPa)	5.88	5.50	3.50

In CRP-6 calculations (Appendix A), use of Redlich-Kwong equation for Cases 9 to 13 has produced consistent results with the results of the participant countries [40]. For the kernel migration analysis case, however, gas pressure and temperature values are relatively high compared to their critical values. Therefore, ideal gas equation of state is more appropriate for this case.

Appendix C

Weibull Distribution

The pyrocarbon and SiC layers are ceramic brittle materials. Brittle materials break easily and their strength is observed to vary from component to component even when a set of identical components are tested [13]. Therefore, the strength of a brittle material is not a well-defined quantity and has to be described by fracture statistics. Also, the assessment of reliability of a brittle material needs a probabilistic approach.

The normal (Gaussian) or Weibull distributions are widely used functions. In coated fuel particle probability analysis, strength of the pyrocarbon and SiC layers are expressed by the Weibull distribution [14, 24, 25, 44]. Weibull cumulative distribution function is described by Equation C.1.

$$f(t) = 1 - \exp\left[-\ln\ 2\ \times \left(\frac{\sigma(t)}{\sigma_0}\right)^m\right] \tag{C.1}$$

where $f(t)$ is the failure probability of the layer at irradiation time t, $\sigma(t)$ is the stress in the layer at irradiation time t, σ_0 is the median strength of the layer and m is the Weibull modulus of the layer. Mostly used σ_0 values for the pyrocarbon and SiC layers are 200 MPa and 873 MPa, respectively. Values used for the Weibull moduli for the pyrocarbon and SiC layers are 5.0 and 8.02, respectively [16].

RESUME

Name Surname : Oya Özdere Gülol

Birth Place : Ankara, TURKEY

Birth Date : August 10, 1976

Martial Status : Married

Children : 1

Education :

- High School, Gazi Anadolu Lisesi, 1987 - 1994
- B.S. Hacettepe University, Department of Nuclear Engineering, 1994 - 1998
- M.Sc. Hacettepe University, Department of Nuclear Engineering, 1998 - 2000

Experience :

- 1998 - 2000 Research Assistant at Hacettepe University, Department of Nuclear Engineering
- 2000 - today Engineer at Turkish Atomic Energy Authority, Department of Nuclear Safety